Multiphoton Microwave Ionization of Rydberg Atoms

Joshua Houston Gurian
Evanston, IL

B.A., Wesleyan University, 2004

A Dissertation presented to the Graduate Faculty
of the University of Virginia in Candidacy for the Degree of
Doctor of Philosophy

Department of Physics

University of Virginia
May, 2010

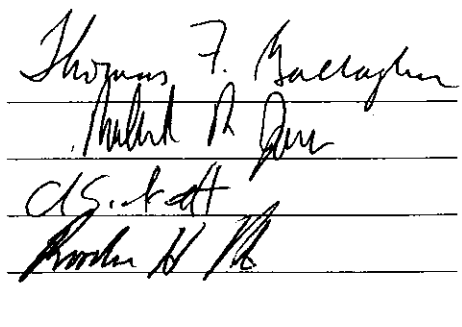

Multiphoton Microwave Ionization of Rydberg Atoms

Joshua Houston Gurian
Evanston, IL

B.A., Wesleyan University, 2004

A Dissertation presented to the Graduate Faculty
of the University of Virginia in Candidacy for the Degree of
Doctor of Philosophy

Department of Physics

University of Virginia
May, 2010

_____

_____

_____

_____

_____

Abstract

This thesis describes a series of multiphoton microwave experiments on Rydberg atoms when the microwave frequency is much greater than the classical Kepler frequency of the excited atoms. A new kHz pulse repetition frequency dye laser system was constructed for Rydberg lithium excitation with a linewidth as narrow as 3 GHz. This new laser system is used for first experiments of multiphoton microwave ionization of Rydberg lithium approaching the photoionization limit using 17 and 36 GHz microwave pulses. A multi-channel quantum defect model is presented that well describes the experimental results, indicating that these results are due to the coherent coupling of many atomic levels both above and below the classical ionization limit. Finally, preliminary results of measuring the final-state distributions of high lying Rydberg states after 17 GHz microwave pulses are presented.

Acknowledgements

Completing this work would not have been possible without the help of many others. My labmates, Ed Shuman, Paul Tanner, Wei Yang, Jianing Han, and Xiaodong Zhang, have all provided guidance and helped to push me in the right directions. Newer lab members Hyunwook Park, Jirakan Nunkaew, and Richard Overstreet have brought a strong sense of camaraderie, and taught me immeasurable amounts with their questions.

My graduate cohort kept time spent outside the lab entertaining and stimulating. Karen Mooney was also kind enough to ensure this work was actually handed in after my departure.

Two people have helped me quite a bit with this work who I have yet to actually meet face-to-face. Alexej Schelle has facilitated some fascinating discussions on microwave ionization of Rydberg atoms, and impressively patient about bridging the disconnect between theory-speak and experiment-speak. Keith Clever at Coherent has always been happy to answer any and all questions pertaining to the Coherent Evolution series lasers, even when there's water covering every optic in your laser cavity.

Chris Floyd, Bryan Wright, David Wimer, and B. H. Kent have helped me with the countless important details of conducting research, covering everything from shipping and receiving to making sure I didn't lose a hand in the machine shop. Tammie Shifflett, Dawn Shifflett, Pam Joseph, and Suzie Garrett are the glue

that keeps this department together and functioning. Rick Marshall and Thomas Clausen have provided me with great graduate career guidance, helping me get the most out of the graduate experience.

Haruka Maeda has been a great mentor in the lab. Haruka and a rock could produce results, and I thank him for letting me be that rock.

Tom Gallagher has truly been the best advisor a student could hope for. It's been both a pleasure and an honor to work with him for the past five years.

Contents

List of Figures

Chapter 1

Introduction

1.1 Rydberg Atoms

Highly excited atoms, or Rydberg atoms, in external fields have long been a rich subject of investigation in atomic physics. Rydberg atoms, with one or more electrons with large principal quantum number n, are highly sensitive to even small perturbations, exhibited by changes in the atoms' often exaggerated properties. In this work I look to illustrate the experimental pieces connecting field and photoionization of Rydberg atoms using microwaves.

I begin this chapter with an overview of some of the basic properties and mathematical tools used to treat Rydberg atoms, and look to give an overview of the current state of microwave ionization of Rydberg atoms. The rest of this dissertation is as follows. In Chapter 2 I give an overview of the experimental setup and methods used in this dissertation. In Chapter 3 I describe first results of multiphoton microwave ionization of lithium atoms at 17 GHz. In Chapter 4 I describe similar experiments using 36 GHz microwave pulses. In Chapter 5 I introduce a Floquet - Quantum Defect Theory model to describe the experimental results. Finally, in Chapter 6 I investigate the final state distributions of surviving bound

atoms after 17 GHz microwave pulses.

The field of Rydberg atoms can be traced back to Johannes Rydberg, who in 1889, after studying a wealth of spectral tables of known atoms, determined that the atomic spectral transition wavelength, λ, between two states n_1 and n_2 with quantum defects δ_1 and δ_2, respectively, could be expressed as a simple expression,

$$\frac{1}{\lambda} = R_\infty \left(\frac{1}{(n_1 - \delta_1)^2} - \frac{1}{(n_2 - \delta_2)^2} \right), \tag{1.1}$$

where R_∞ is what is now referred to as the Rydberg constant,

$$R_\infty = 109737\,\mathrm{cm}^{-1}, \tag{1.2}$$

which Rydberg properly computed for hydrogen to within a tenth of a percent of the currently known value[1].

In 1913 Bohr showed that for hydrogen the Rydberg constant could be expressed in terms of physical constants,

$$R = \frac{k^2 Z^2 e^4 m_e}{2\hbar^2}, \tag{1.3}$$

where k is the Coulomb force constant, Z is the atomic number, e and m_e are the charge and mass of the electron, and $\hbar$ is the reduced Planck constant, or the Dirac constant. Bohr was therefore able to express the energy levels of the hydrogenic atoms terms of physical constants,

$$W = \frac{-k^2 Z^2 e^4 m_e}{2\hbar^2 n^2}, \tag{1.4}$$

most importantly scaling as n^{-2}. Many of the properties of Rydberg atoms scale proportionally to a power of the principal quantum number, n. Throughout this

dissertation we will be exploiting many of these physical properties, and some of the relevant properties are summarized in the table below[2].

Property	Scaling
Binding energy	n^{-2}
Adjacent n level spacing	n^{-3}
Classical Kepler frequency	n^{-3}
Orbital radius	n^{2}

1.1.1 Atomic Units

As Eq. (1.4) well illustrates, it would be best to introduce atomic units sooner rather than later. Unless otherwise noted, atomic units will be used throughout this dissertation to simplify equations. To quickly summarize,

Constant	Symbol	SI	AU
Mass	m_e	$9.1 \times 10^{-31}\,\mathrm{kg}$	1
Action	$\hbar$	$1.05 \times 10^{-34}\,\mathrm{J{\cdot}sec}$	1
Charge	e	$1.6 \times 10^{-19}\,\mathrm{C}$	1
Length	a_0	$5.29 \times 10^{-11}\,\mathrm{m}$	1
Energy	W	$2 \times 13.6\,\mathrm{eV}$	1
Frequency	$\omega/2\pi$	$6.5761 \times 10^{6}\,\mathrm{GHz}$	1
Electric Field	E	$5.137 \times 10^{9}\,\mathrm{V/cm}$	1

Equation (1.4) can therefore be more cleanly written as,

$$W = \frac{-1}{2n^2}. \tag{1.5}$$

1.1.2 Quantum Defect Theory

Non-hydrogenic atoms exhibit shifted energy levels, due to the non-Coulombic potential of the ionic core. The binding energy of the Rydberg atom can be written as,

$$W = \frac{-1}{2(n-\delta_\ell(n))^2}, \tag{1.6}$$

where $\delta_\ell(n)$ is the quantum defect, the phase shift divided by π of the nonhydrogenic Rydberg wavefunction from the hydrogenic wavefunction. The quantum defects for an atomic species are heavily ℓ dependent and weakly n dependent. These quantum defects are empirically determined and approach zero for high-ℓ states, since the electron never approaches the ionic core. For ^{7}Li, these quantum defects are[3, 4],

$$\delta_s(n) = 0.3995101(10) + 0.0290(5)(n-0.3995)^{-2} \tag{1.7a}$$

$$\delta_{p_{1/2}}(n) = 0.0471780(20) - 0.024(1)(n-0.0471)^{-2} \tag{1.7b}$$

$$\delta_{p_{3/2}}(n) = 0.0471665(20) - 0.024(1)(n-0.0471)^{-2} \tag{1.7c}$$

$$\delta_d(n) = 0.002129 - 0.01491(n-0.002129)^{-2} \tag{1.7d}$$

$$\delta_f(n) = -0.000077 + 0.021856(n+0.000077)^{-2}, \tag{1.7e}$$

and are illustrated in Fig. 1.1.

1.2 Ionization Processes in atoms

1.2.1 Field Ionization

At one extreme of this subject is the basic concept of field ionization of atoms. A rich subject itself , the salient points of field ionization will be discussed below.

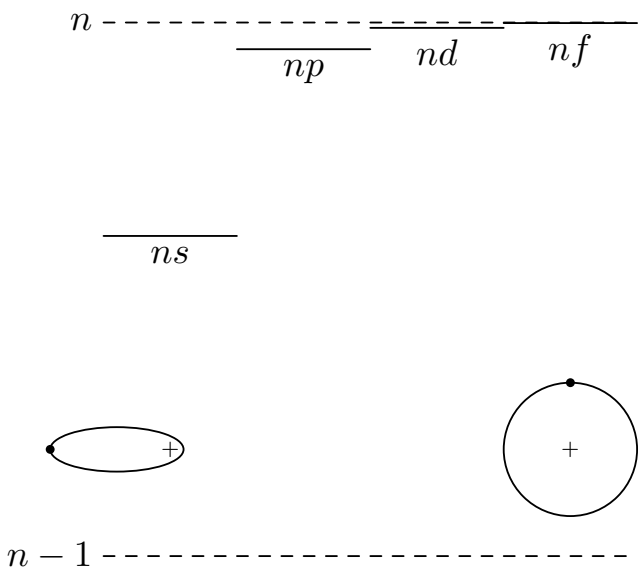

Figure 1.1: Lithium energy levels as a function of ℓ plotted between the hydrogenic n and $n-1$ levels (dashed lines). Example low and high angular momentum classical orbits are shown at the bottom left and right of the figure, respectively.

Hydrogenic ionization

We can first look at hydrogenic field ionization. Applying an electric field, E, tips

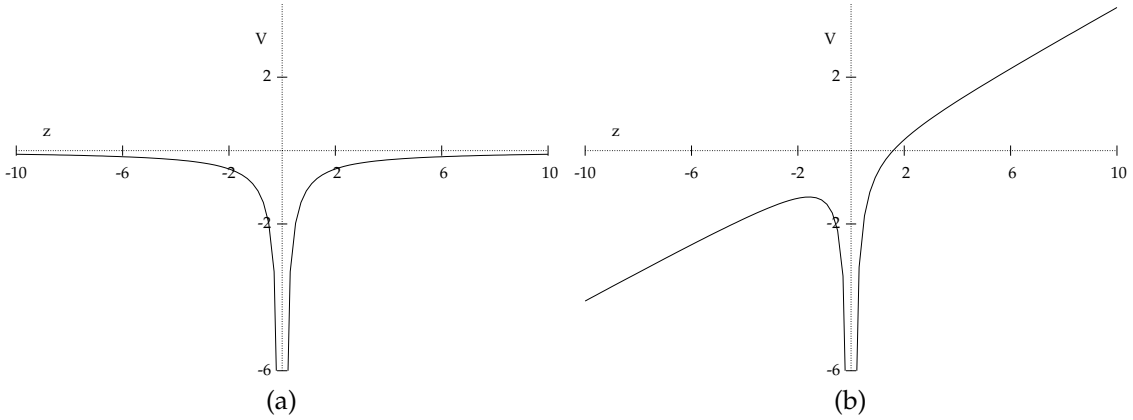

Figure 1.2: (a) Coulomb and (b) combined Stark-Coulomb potentials.

the atomic Coulomb potential,

$$V(z) = \frac{-1}{|z|} + Ez, \tag{1.8}$$

where z is the direction of the electric field, as shown by Fig. 1.2. We can find the field necessary for the electron to go over the Coulomb-Stark barrier by first setting the derivative of the potential equal to zero,

$$\frac{dV}{dz} = 0 = z^{-2} + E, \tag{1.9}$$

giving the coordinate of the top of the potential saddle point. Substitution into Eq. (1.8) leads to the potential energy $-2\sqrt{E}$ due to the applied field . Ionization occurs when the binding energy of the atom, W, is less than the field potential. Equating them leads to the requisite field required for ionization,

$$E = \frac{W^2}{4} \tag{1.10}$$

which with Eq. (1.5) reduces to $1/16n^4$, denoted as the classically allowed ionization field. The derivation of Eq. (1.10) ignores some important subtleties, namely the shift in energies from the Stark effect and the centripetal barrier seen by high m states. In the presence of the electric field, ℓ is no longer a good quantum number and is replaced by the non-negative parabolic quantum numbers, n_1 and n_2, where,

$$n = n_1 + n_2 + |m| + 1. \tag{1.11}$$

The electric field also shifts the atomic energy levels, which to first order can be written as

$$W = \frac{-1}{2n^2} - \frac{3}{2}E(n_1 - n_2)n. \tag{1.12}$$

For the reddest state, or state shifted lowest in energy, $n_1 - n_2$ can be substituted for n[2]. Solving Eq. (1.10) for the new requisite field when $m \neq 0$ yields $E = 1/9n^4$. The $1/16n^4$ and $1/9n^4$ fields are shown on the hydrogen Stark maps for

$n = 12 \ldots 17$ in Figs. 1.3a and 1.3b. Bluer states, or states shifted higher in energy, ionize in higher fields, usually higher by a factor of two to n, but there is no equally simple way of estimating a threshold field[5]. Parabolic coordinates may be used to describe field ionization, where motion is bound in the ξ coordinate, and electrons ionize at infinity in the η coordinate.

Nonhydrogenic ionization

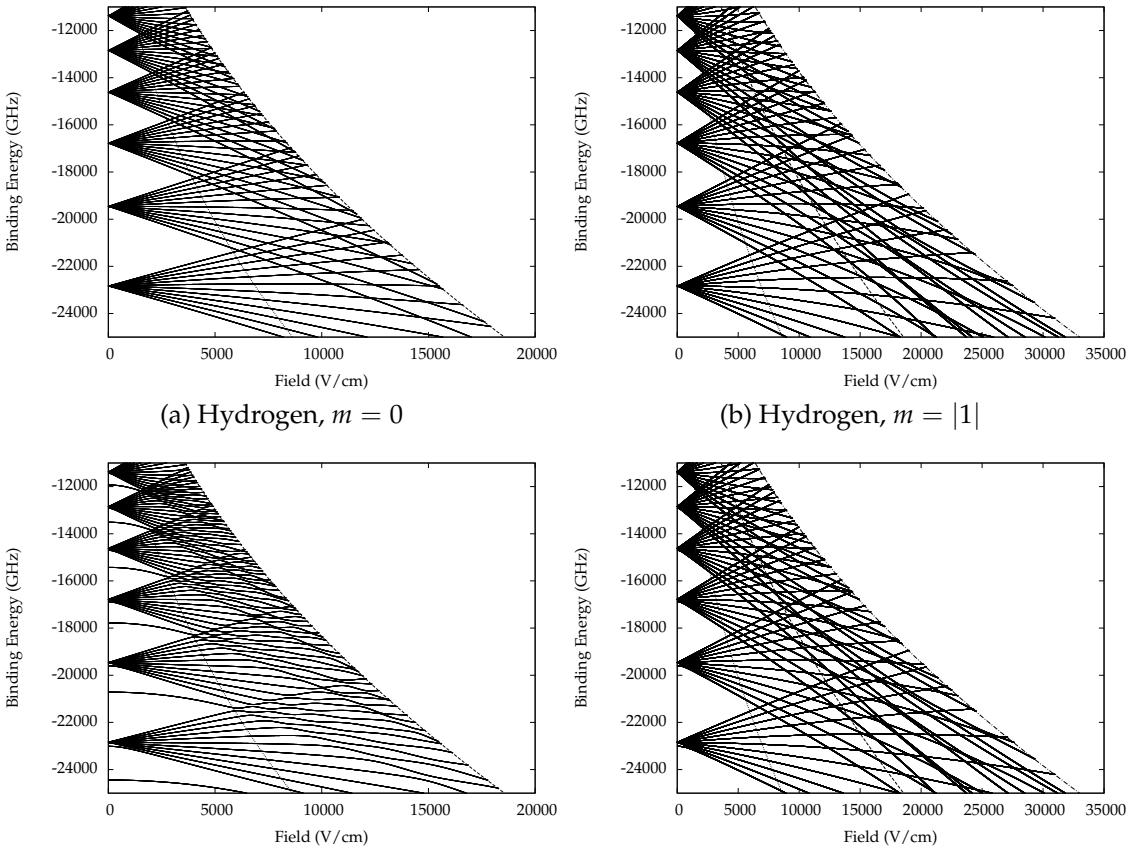

(a) Hydrogen, $m = 0$

(b) Hydrogen, $m = |1|$

(c) Lithium, $m = 0$

(d) Lithium, $m = |1|$

Figure 1.3: Stark maps for H and Li, $m = \{0, |1|\}$, for $n = 12 \ldots 17$ as a function of binding energy. Also plotted are $1/9n^4$ (dot-dashed line), $1/16n^4$ (dashed line), and $1/3n^5$ Inglis-Teller limit (dotted line).

Nonhydrogenic atoms can ionize in the same fashion as hydrogenic atoms, maintaining the same approximate value of n_1 as the electron overcomes the po-

tential barrier found by Eq. (1.9) for the red state. Blue states again ionize in a higher field. Nonhydrogenic ionization adds a second, often more rapid, method of ionization not occurring in hydrogenic atoms that is similar to autoionization[5]. Nonhydrogenic atom wavefunctions in an electric field are no longer separable in parabolic coordinates and n_1 is no longer a good quantum number. Just as the core perturbation causes avoided level crossings, as visible in the lithium Stark map for $m = 0$ shown in Fig. 1.3c, the core perturbation couples levels of different n_1. Red and blue states overlap slightly at the atomic core and couple together. High n_1 states couple to Stark continua states of low n_1 and ionize. Littman *et al.* first illustrated this in $|m| = 1$ states of lithium, ionizing at a field of $1/9n^4$[6]. For $m = 0$ ionization in nonhydrogenic atoms occurs at a field according to $1/16n^4$.

1.2.2 Photoionization

On the other extreme is photoionization, where one or more photons of sum total energy greater than the electron binding energy W incident on an atom provides the energy to cause ionization.

First experiments of photoionization were undertaken by Hertz in 1886, concluding that UV light was a requisite component of the photoelectric effect, but Hertz did not attempt an explanation of his results. In 1905, Einstein successfully explained the photoelectric effect with the quantization of incident light hf, where f is the frequency of light, and received the Nobel prize in 1921 for his efforts[7].

The advent of strong laser light sources has opened atomic photoionization into a broad sub-field of physics. Photoionization processes are primarily divided into two regimes by the Keldysh tunneling parameter,

$$\gamma = \sqrt{\frac{W_{ion}}{2\Phi_{pond}}}, \tag{1.13}$$

where W_{ion} is the binding energy of the atom, and Φ_{pond} is the ponderomotive potential of the applied laser field, given as,

$$\Phi_{pond} = \frac{E^2}{4\omega^2}, \tag{1.14}$$

where E is the field amplitude of the incident light of frequency ω. The Keldysh parameter is essentially the ratio of the laser frequency to the tunneling frequency through the combined Stark-Coulomb potential barrier[8]. If $\gamma < 1$ ionization is a tunneling process and if $\gamma > 1$ then ionization is a multiphoton process, and this work will primarily concern only the latter. In a perturbation theory regime, N-photon ionization of ground state atoms is at least an N-th order process[9–12].

Photoionization is often best described not by a requisite field amplitude, but instead by a rate. In a regime where perturbation theory is valid and depletion of the initial state is small, the rate of transfer between two atomic states $|i\rangle$ and $|f\rangle$ in a field E, where $|f\rangle$ is normalized per unit energy, is given by Fermi's Golden Rule[13],

$$\Gamma = 2\pi|\langle f|r \cdot E|i\rangle|^2. \tag{1.15}$$

Single photon photoionization rates can be calculated using Fermi's Golden Rule by inserting a bound atomic state as the initial state and a normalized per unit energy continuum state for the final state.

Fermi's Golden Rule has been applied in many more complicated situations, and with regards to experiments presented in Chapters 3 and 4, most importantly with above threshold ionization. Above threshold ionization is when an electron energetically above ionization threshold absorbs one or more additional photons. Deng and Eberly[14, 15] successfully described multiphoton absorption above threshold ionization using a quantum mechanical model of strong coherent continuum

- continuum electric dipole coupling above the limit where the coupling over the ionization limit is a perturbative bound - continuum coupling from the ground state given by Fermi's Golden Rule.

Whereas Deng and Eberly's approach well describes the ground state case, a proper description of multiphoton ionization by laser fields of Rydberg atoms was developed by Giusti-Suzor and Zoller[16]. Giusti-Suzor and Zoller formulated it as a multichannel quantum defect theory - Floquet problem where the couplings between channels are described by radiative dipole couplings of finite range. Their approach shows that the strong coherent coupling of states continues smoothly over the limit to the bound states. A full treatment of a Rydberg atom in a microwave field using a similar approach will be discussed in Chapter 5.

1.3 Previous Work

Sitting in between field ionization and photoionization is microwave ionization of excited atoms. What follows is an overview of the body of research to date on microwave ionization of Rydberg atoms.

1.3.1 Scaled Units

Previous work on microwave ionization, outlined below, has used scaled microwave units for the classification of systems with great success. The scaled microwave frequency, Ω, is the ratio of the microwave frequency ω to the $1/n^3$ classical Kepler frequency of the atom,

$$\Omega = \omega n^3. \tag{1.16}$$

The scaled microwave field amplitude, E_0, is the ratio of the microwave field amplitude E to the $1/n^4$ electric field of the Coulomb potential,

$$E_0 = En^4. \tag{1.17}$$

Scaled microwave units have proven to be a useful tool in the classification of systems, as illustrated by Fig. 1.4. The gray shaded area represents experimentally explored regions. Scaled microwave units draw a clear separation in the dynamics of systems where $\Omega < 1$ and $\Omega > 1$, where microwave ionization processes are fundamentally different for both hydrogenic and non-hydrogenic atoms, as will be illustrated below. However, scaled units are not a useful method of analyzing atomic spectra near the photoionization limit, defined as $\Omega = n/2$. For this dissertation lab units are preferred over scaled microwave units and will be used unless otherwise specified.

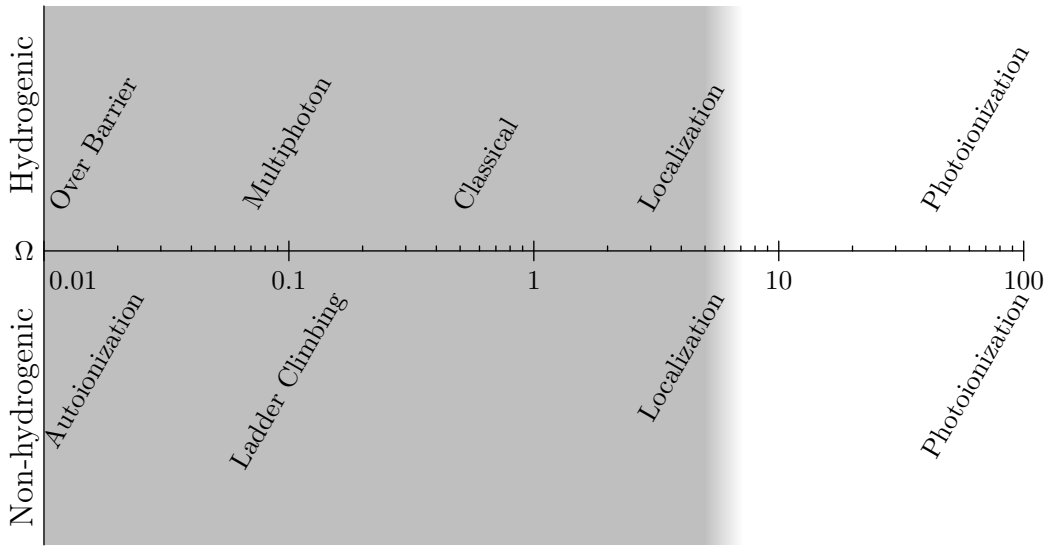

Figure 1.4: Classification schematic of the dynamics of microwave ionization as a function of scaled frequency. The gray shaded areas represents the experimentally explored regions. Figure updated from Clausen[17].

1.3.2 Low Scaled Frequency

Hydrogenic atoms

The first experimental work on microwave ionization, published in 1974, was undertaken by Bayfield and Koch[18], who used 30 MHz, 1.5 GHz, and 9.9 GHz fields to ionize a fast beam of excited hydrogen atoms in states around $n = 65$. Interestingly, H atoms ionized in the same field amplitude for 30 MHz and 1.5 GHz fields, the same $1/9n^4$ field for ionization of the red state in a static field, and a lower field was required at 9.9 GHz. By 1983, work on microwave ionization illustrated the differences between hydrogenic and non-hydrogenic atoms in fields where the microwave frequency is below the $1/n^3$ transition frequency[19]. Further work on hydrogen showed that the $1/9n^4$ field dependence for low frequencies decreased as the scaled frequency approached unity, as shown in Fig. 1.5[20]. Quantum mechanically, this $1/9n^4$ field dependence can be considered a byproduct of the second-order Stark effect. The oscillating microwave field creates a Stark state for a given n and m. Due to the second-order Stark effect the slope of the state, dW/dE, is not constant. When the microwave field reverses the Stark state created by the field $-E$ does not have the same slope, and the original Stark state is projected on to a set of Stark states of the same n and m. Ionization occurs when the field is large enough to ionize the reddest Stark state. Classically, hydrogenic microwave ionization has been well described as the onset of classical chaos[21]. More recently, Clausen and Blümel have shown a fourth-order perturbation theory model properly describes the multiphoton resonances experimentally observed in hydrogen below $\Omega = 1$[23].

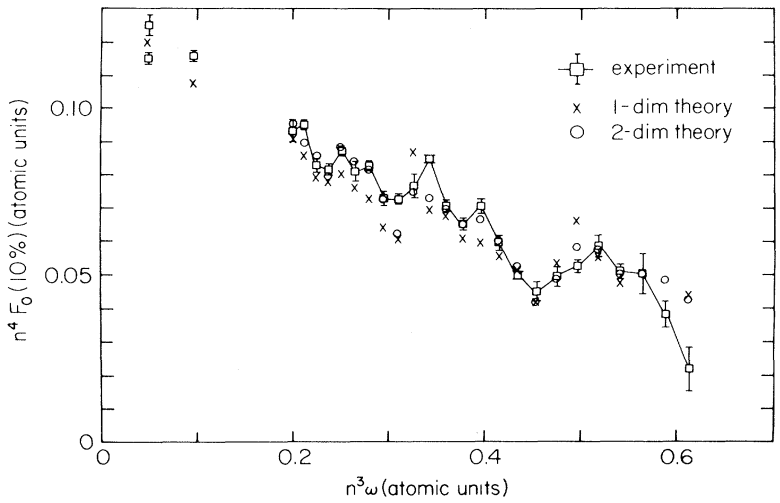

Figure 1.5: Threshold 10% scaled field vs scaled microwave frequency, from van Leeuwen *et al.*[20]. A 1D classical surface state electron model and 2D classical hydrogenic monte carlo model[22] fit experimental results for $0.2 < \Omega < 0.6$.

Non-hydrogenic atoms

A different picture exists for non-hydrogenic atoms. Pillet *et al.*[24] showed a $1/3n^5$ field requirement for low m alkali atoms. Although both forms of microwave ionization are essentially field processes, they occur for fundamentally different reasons. Microwave ionization of nonhydrogenic atoms can be thought of as a ladder climbing mechanism, as shown in Fig. 1.6. As the field increases to $1/3n^5$, point A in Fig. 1.6, atoms make a Landau-Zener transition to the $n+1$ state, traversing the avoided crossing of the n and $n+1$ states. Successive microwave cycles drive further transitions to higher states until the direct field ionization occurs at point B in Fig. 1.6. This Landau-Zener transition picture fails to account for the coherent effects of many microwave cycles, which lowers the field required.

A more subtle picture of microwave ionization of nonhydrogenic atoms is needed to properly explain some experiment results. Pillet *et al.* have illustrated microwave ionization results not well explained using a single-cycle Landau-Zener

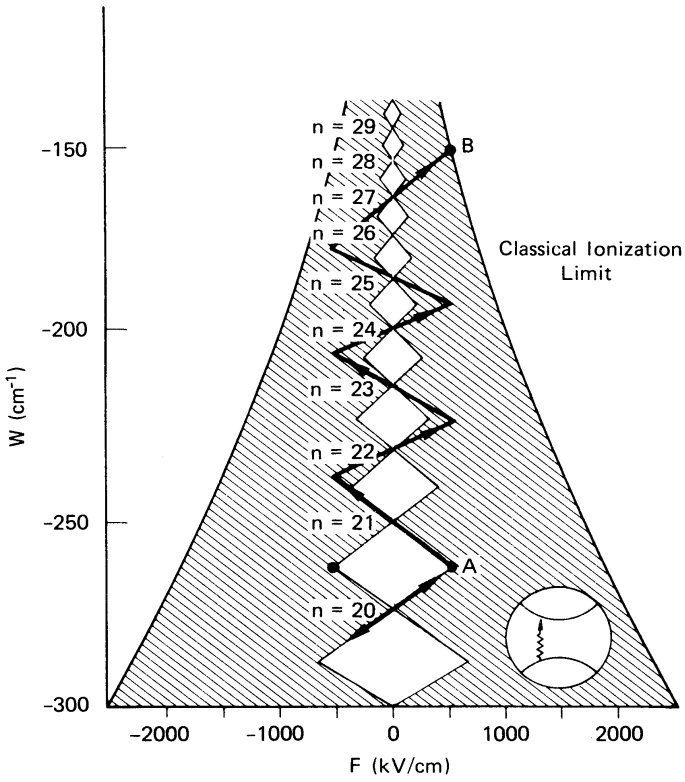

Figure 1.6: Energy level diagram illustrating the ladder climbing mechanism of nonhydrogenic microwave ionization in a microwave field where $\Omega < 1$, from Pillet *et al.*[25]. If the microwave field is greater than $1/3n^5$ an initial $n = 20$ atom traverses the avoided crossing at point A to the $n = 21$ state. Successive microwave cycles cause a series of Landau-Zener transitions bring the atom to a large enough n such that direct field ionization can occur, labeled as point B.

picture[26]. Lithium atoms excited to the $36d$ state ionize in a 15 GHz 340 V/cm microwave field, corresponding to $E_{mw} = 1/9n^4$. Applying a small 1 V/cm static field lowers the threshold ionization field to $1/3n^5$. In zero field, the microwave field creates a set of sidebands spaced by the microwave frequency ω spanning $\pm kE_{mw}$. For a $n \rightarrow n+1$ transition the n and $n+1$ sidebands must overlap, with the detuning between the sidebands small compared to the coupling matrix element. Microwave ionization is suppressed when the coupling matrix elements are small compared to the microwave frequency and ionization requires a $1/9n^4$ field

amplitude. When a small static field,

$$E_s \geq \frac{\omega}{6n^2}, \tag{1.18}$$

is applied, the sidebands are split by a $3/2nkE_s$ Stark shift, and a quasi-continuum of states is created where the central sideband of states has spacing of ω/n rather than ω in zero static field. Microwave ionization occurs at a threshold only slightly higher than $1/3n^5$, a result not explained by a single-cycle model. Stoneman *et al.* also required a multi-cycle description for microwave transitions from the $19s$ state to the $n = 17$ Stark manifold in potassium[27]. Each cycle of the microwave samples the avoided crossing, and the transition amplitude of each microwave cycle coherently add together to form multiphoton resonances. The full multiphoton picture can be described using a Floquet approach, the mechanics of which will be discussed in section 5.1.

1.3.3 High Scaled Frequency

In the region $1 < \Omega < 2$ the classical description slowly breaks down, predicting ionization fields much lower than experimentally measured[17, 28]. Explaining microwave ionization when the microwave frequency is greater than the $1/n^3$ level spacing has been an area of much theoretical research and is still incompletely understood. Most theoretical work has been based around a "localization" concept for ionization, roughly analogous to Anderson localization which describes electron transport in 1D solid state systems. These localization models have been applied to both hydrogenic and nonhydrogenic atoms with some success[29]. These models will be discussed below.

Jensen *et al.*

The previous best theoretical description of experimental data came from Jensen *et al.*, simplifying the localization work of Casati *et al.*[21, 30]. Given two high-lying one dimensional states, n and n', the on resonance Rabi frequency between the two states can be written as[31],

$$\omega_R = \mu \cdot E \tag{1.19}$$

where μ is given by by Delone *et al.*[31],

$$\mu = \langle n|r|n'\rangle = \frac{0.4108}{(nn')^{3/2}\omega^{5/3}}, \tag{1.20}$$

where ω is the applied microwave frequency. We can assume $n \approx n'$ and that $n \gg (n' - n)$. Jensen *et al.* introduce the parameter a, the ratio of the Rabi width, ω_R to the detuning from resonance, Δ. The maximum detuning from resonance is half the atomic level spacing, giving a as,

$$a = \frac{\omega_R}{\Delta} = \frac{\dfrac{0.4108E}{n^3\omega^{5/3}}}{\dfrac{1}{2n^3}} = \frac{0.4108E}{2\omega^{5/3}}, \tag{1.21}$$

which is independent of n. The extremes of $a \ll 1$ and $a \gg 1$ are known as the "strong-disorder" and "weak-disorder" regimes of Anderson localization in solid-state physics[30]. When $a < 2$, the Rabi width spans at most a single n state and the microwave field couples a sequence of single states one photon apart, creating a few strongly coupled levels. When $a \geq 2$ the Rabi width is greater than the $1/n^3$ state spacing and the Rabi width contains more than a single state. The process can no longer be considered as a coherent sequence of single state transitions. Instead the coupling of levels extends all the way to the ionization limit, and diffusive

microwave ionization occurs. This $a = 2$ condition for microwave ionization can be succinctly written as,

$$E = 2.4\omega^{5/3}, \tag{1.22}$$

and is n independent. Equation (1.22) has been previously shown to hold for Sr in the region where $1 < \Omega < 5$[28].

Maeda and Gallagher measured the 50% ionization threshold field for strontium in the range of $0.9 < \Omega < 5.5$[28]. Their results are shown in Fig. 1.7. Stray fields on the order of $\sim$60 mV/cm in the experimental interaction region set the cutoff n at $n_c = 270$, and artificially depressing the cutoff n lowered the requisite field required for ionization. Also shown in the figure are the theoretical predictions of Jensen *et al.*[21] (solid curve), and two predictions of Casati *et al.*[32]; a classical prediction (thick dashed curve) and a quantum prediction (thin dashed curve). Although the Casati *et al.* result best matches the data in the region of $1 < \Omega < 3$ it exhibits the wrong functional form, and the Jensen *et al.* result best indicates a lower bound for ionization.

Schelle *et al.*

Schelle *et al.*[29] have expanded the approach of Casati *et al.* to a more developed localization model, strongly drawing corollaries to Anderson localization in condensed matter systems. Anderson localization is the inhibition of quantum transport due to destructive interference in disordered quantum systems[34]. Applied to microwave ionization of atoms, the microwave photons define multiphoton transitions between the initial and final states, the amplitudes of which must be coherently summed together and destructive interference causes localization. Casati *et al.* posited that ionization occurs when the localization length reaches all the way to the ionization limit[32, 33]. Schelle *et al.* again apply the localization

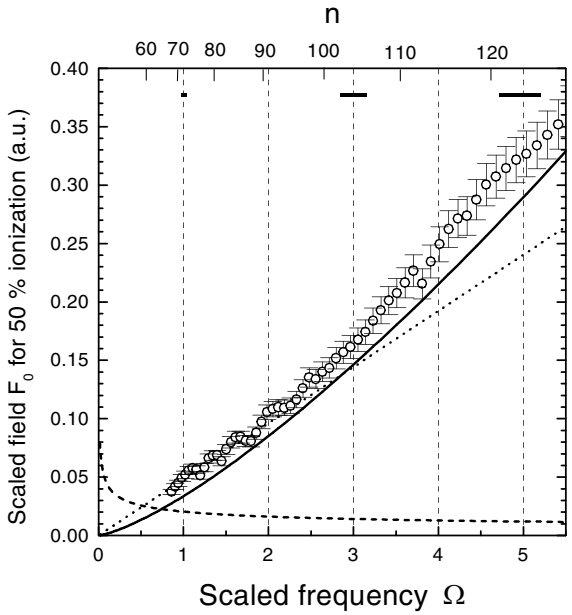

Figure 1.7: Scaled 50% ionization threshold fields for $0.9 < \Omega < 5.5$ from Maeda and Gallagher[28], shown along with theoretical predictions. The classical prediction of Casati *et al.*[32] is plotted as the dashed line and clearly fails as the scaled frequency increases. The quantum mechanical prediction of Casati *et al.*[33] is the plotted as the dotted line. The prediction of Jensen *et al.*[21] is plotted as the solid line and best matches the experimental measurements.

ionization condition to an extensive augmented Floquet matrix diagonalization of banded symmetric complex matrices on the order of 10^6[35–39]. The results of their calculations are shown in Fig. 1.8 for a 500 ns microwave pulse at $\omega = 17.5$ GHz using np states up to $n = 245$. The ionization limit is assumed to be one microwave photon above $n = 230$, at $n_c = 270$. For these calculations, photoionization occurs at scaled frequency $\Omega = 32$.

The results shown in region (I) of Fig. 1.8 agree with the previous theoretical prediction of Jensen *et al.*[21, 30] and the experimental results of Maeda and Gallagher[28]. As we will discuss further in Chapters 3 and 4, our recent experiments match well with the theoretical predictions shown in region (II), but widely diverge for region (III) of Fig. 1.8, one microwave photon from the ionization limit..

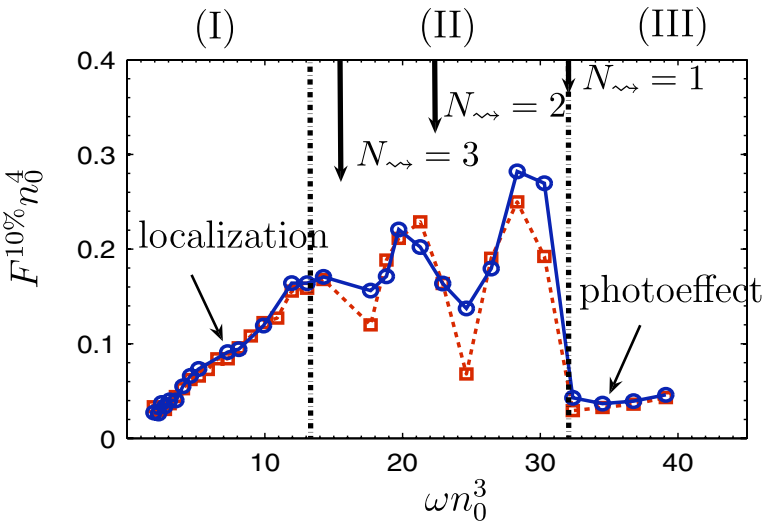

Figure 1.8: Scaled 10% ionization threshold field for atomic hydrogen (□) and lithium (○) at $\omega = 17.5\,\mathrm{GHz}$ and t=500 ns, from Schelle *et al.*[29]. The cutoff state is taken to be $n_c = 270$ and photoionization occurs in region (III).

Chapter 2

Experimental Setup

2.1 Overview

This chapter covers the experimental details required for the experiments in this dissertation. In particular, the design of the kilohertz repetition rate dye laser system, microwave components, vacuum hardware, and electronics for exciting ground state lithium to Rydberg states and observing the results from the application of microwave fields.

The general method for the following experiments is composed of four things. Initial state preparation of ground state lithium to Rydberg np states, microwave interaction, remaining population state detection, and finally, data collation. An example timing diagram is shown in Fig. 2.1. This chapter attempts to clarify the techniques necessary for these four steps.

2.2 Thermal Li Beam

The experiment is based around a thermal beam of ground state lithium atoms. The beam is created by resistively heating a small oven filled with lithium to a va-

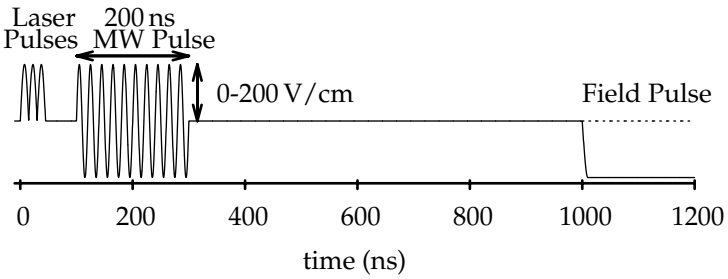

Figure 2.1: Experimental Timing diagram

por pressure on the order of a torr[40]. The oven is created by drilling a roughly 1 mm diameter hole in the center of a 0.3125" diameter, 0.008" walled, 321 seamless stainless steel tube. The ends of the tube are hammered shut. By running between 40 and 60 A through the tube an effusive Li beam is created which is then collimated using a series of apertures.

2.3 kHz Laser Setup

2.3.1 Introduction

The workhorse laser system of Rydberg atom physics has long been a system of Littman-Metcalf pulsed dye lasers pumped by Q-switched, frequency doubled or tripled Nd:YAG lasers. However, Nd:YAG lasers usually have pulse repetition frequencies of 10 to 100 Hz with pulse lengths of 5-10 ns, producing dye pulses of similar length. Recently, kHz repetition rate pump lasers have become commercially available as turn-key solutions for pump lasers systems. These lasers, mostly Q-switched, frequency doubled or tripled Nd:YLF lasers, have gained popularity as pumps for Ti:sapphire regenerative amplifiers[41]. The existence of these kHz Ti:sapphire lasers has fueled interest in the development of kHz repetition rate dye lasers for preparation of excited atomic and molecular states. Unfortunately, most doubled Nd:YLF lasers used to pump the regenerative amplifiers produce 527 nm

pulses 200 ns long, far too long to pump a conventional ns dye laser[42–44]. Most problematic is the long tail of the pump pulse which contributes to dye heating. One approach to using such a long pump laser is to use a dye laser cavity more like that of a continuous wave (cw) laser[45, 46]. Typically the resulting linewidths are 30 GHz unless an intracavity etalon is used.

Here a different approach is used, slicing the pump pulse into shorter pulses, an approach which enables us to pump three dye lasers of conventional design[42–44] for creating lithium np Rydberg states.

2.3.2 Design and Performance

Nd:YLF Pump Laser

The pump laser is a Coherent Evolution-30 diode pumped solid state, frequency doubled, Q-switched Nd:YLF laser. The Evolution-30 laser produces horizontally polarized 200 ns FWHM pulses of 527 nm light at a 1 kHz repetition rate and can deliver up to 20 W of average power. Twelve AlGaAs laser diodes pump the Nd:YLF rod to produce 1053 nm light. The laser cavity is internally Q-switched via quartz blocks. Piezo-electric transducers convert rf pulses to ultrasonic waves. The changing optical index of the quartz, via the photoelastic effect, spoils the Q of the cavity.

The 1053 nm light is frequency doubled in the laser cavity by a lithium triborate (LBO) crystal, heated to 318° C. The LBO crystal is non-critically phase-matched to provide efficient doubling without cavity stabilization. A dichroic folding mirror serves as an output coupler with high transmission at 527 nm and high reflection at 1057 nm. Waste heat is managed by a 2 kW recirculating chiller with a 23° C setpoint. All together this produces up to 20 W of 527 nm light in 200 ns pulses at pulse repetition frequency of 1 kHz. The photodiode signal of a single pulse is

shown in Fig. 2.5.

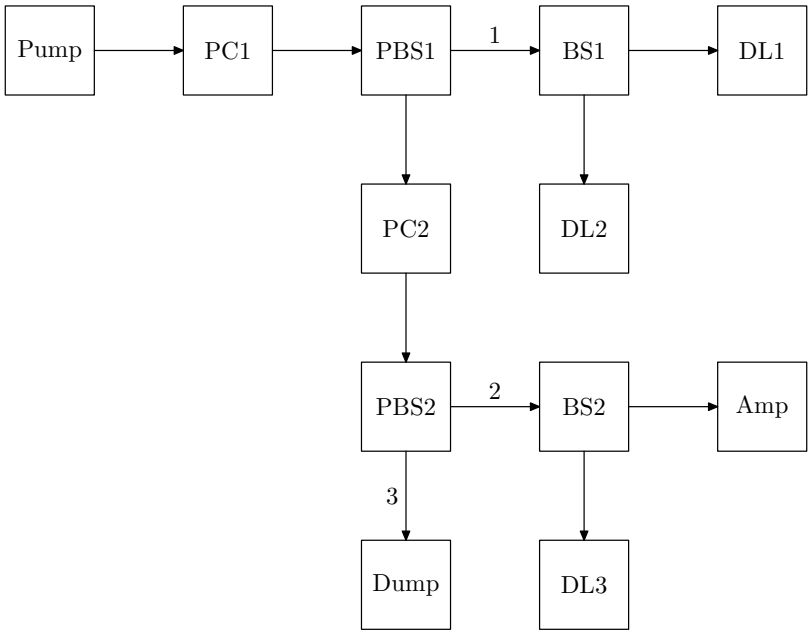

Figure 2.2: Laser system schematic. Shown are the pump laser, Pockels cells (PC), polarizing beam splitting cubes (PBS), beam splitting cubes (BS), dye lasers (DL1-3), single-pass dye amplifier (A1) and beam dump.

Pulse splitting

As mentioned earlier, the essential idea is to split each pulse into shorter pulses. Accordingly, each pulse from the Evolution-30 pump laser is split into three temporally distinct pulses using a system of two DKDP Pockels cells, schematically shown in Fig. 2.2.

The phase retardation of a noncentrosymmetric crystal is linear with respect to an applied electric field, known as the Pockels effect. By placing a noncentrosymmetric crystal between two electrodes, this can be exploited to make a voltage controlled waveplate, known as a Pockels cell[47]. The phase retardation of the

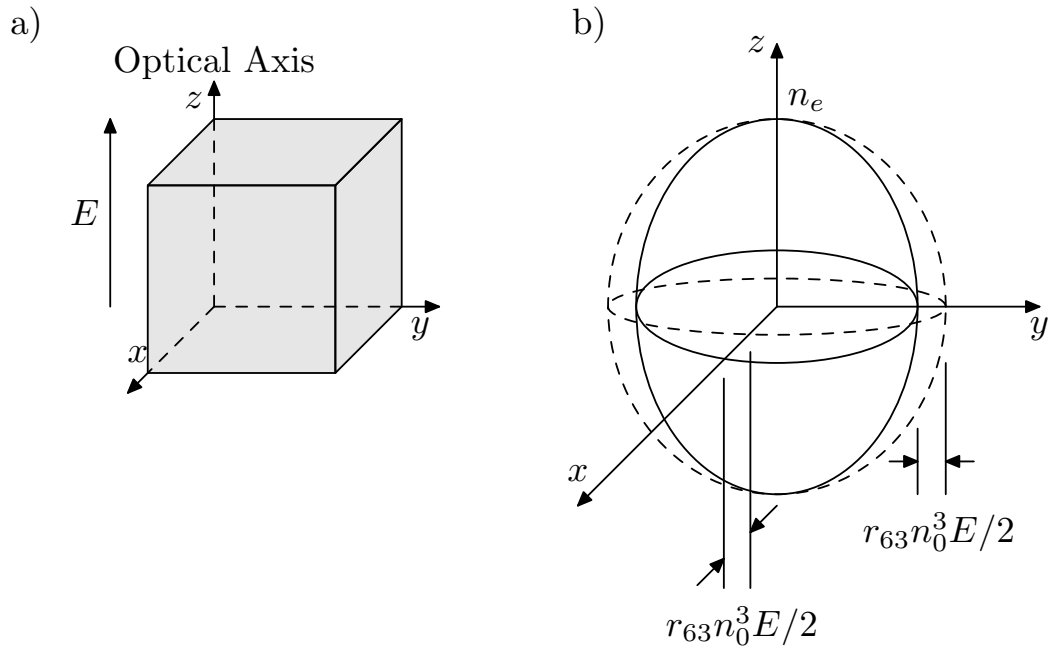

Figure 2.3: The a) orientation of DKDP crystal in relation to the electric field, and b) modified index ellipsoid, from [47].

Pockels cell can be written as,

$$\Delta\varphi = \frac{2\pi n_o^3 r_{63} V}{\lambda_0}, \tag{2.1}$$

where r_{63} is the electro-optic constant (23.3×10^{-12} m/V for DKDP), n_o the ordinary index of refraction ($n_o = 1.52$ for DKDP), V the applied voltage, and λ_0 is the wavelength of light[48]. For 527 nm light the half-wave voltage, $V_{\lambda/2}$, when $\Delta\varphi = \pi$, is roughly 4 kV. The optical axis is along the direction of the applied voltage, and the new principle axes of the Pockels cell are rotated 45° about the optical axis. The indices of refraction modified by the field are graphically shown in Fig. 2.3.

Proper alignment of the Pockels cells are critical for rotating the laser polarization. The alignment procedure is summarized below. The initial pump laser pulse is horizontally polarized. The first Pockels cell is grossly set in the beam path

in a mount capable of adjusting pitch, yaw, and roll. The Pockels cell electrodes should be approximately 45° from horizontal. The pump laser should be set to a power just above visible lasing, such that the laser intensity is still comfortable to look at when reflected by an index card. The laser beam should be centered about the Pockels cell entrance and exit apertures. Pieces of frosted tape or glass slides are helpful in determining this, although take care to place tape only covering the aperture and not to touch the optical faces of the cell. Fix an index card in the beam path at a distance of at least 30 cm past the Pockels cell. Using a pen or small marker, mark the beam spot on the index card. Next, place a piece of frosted tape over the entrance aperture of the cell and diffuse light should now be incident on the index card. Place a sheet of polarizer behind the exit aperture. The polarizer should be aligned to transmit vertically polarized light. An isogyre cross pattern, illustrated in Fig. 2.4, should be visible on the index card. The original beam spot position on the index card will most likely not be centered in the cross pattern. Adjust the pitch and yaw of the cell to center the beam spot in the cross pattern, and adjust the roll of the cell to maximize the contrast of the isogyre pattern. Recheck the beam alignment through the center of the cell and repeat the above process. Finally, remove the tape, polarizer, and index card and send the beam through the polarizing beam splitting cube. Block both outputs from the polarizing beam splitting cube using a beam dump and increase the pump power to normal operating voltage. Place a photodiode near each beam dump to monitor the light reflected from beam dump. Adjust the Pockels cell driving voltage to maximize switching contrast by monitoring the photodiode signals. Alignment of the second Pockels cell is a similar process, although the input light is vertically polarized. Therefore, the Pockels cell is mounted 90° from the first cell.

The Pockels cells are switched from zero retardation to $\lambda/2$ retardation in 2 ns,

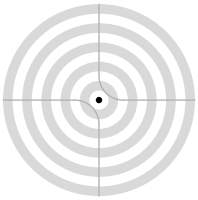

Figure 2.4: Isogyre pattern from properly centered Pockels cell. The shaded rings and lines are dark regions where light is not projected on the index card, and the central black dot is the marked initial laser spot.

a time that is short compared to the laser pulse length. The half-wave voltage $V_{\lambda/2} = 3.9\,\text{kV}$ is generated by a avalanche transistor based Marx-bank circuit using Motorola 2N5551 transistors[49]. A discussion of the Pockel's cell electronics can be found in 2.6.1. The two Pockels cells are switched at 48 and 81 ns after the beginning of the laser pulse at t = 0. Light exiting the first Pockels cell (PC1) is sent to a polarizing beam splitting cube (PBS1). Horizontally polarized light passes straight through PBS1 becoming what we term the first pulse, whereas the rotated, vertically polarized light is sent through the second Pockels cell (PC2). Light exiting the second Pockels cell is sent to the second polarizing beam splitting cube (PBS2). Vertically polarized light is reflected to produce the second pulse and horizontally polarized light retarded by PC2, the long tail, passes straight through as the third pulse. The timing of the light pulses is shown in Fig. 2.6. Figure 2.5 shows the pulse as it comes from the pump laser, and Fig. 2.6 shows how it is split into three pieces. The first, second, and third pulses have widths of 16 ns, 35 ns, and 45 ns, respectively. Note, however, that the Pockels cell timing may be tailored to fit the needs of the experiment. The pulse energies of the three pulses are 4.25, 3.75, and 3.5 mJ, respectively.

The first pulse, further split by a 50-50 beam splitter (BS1), pumps two single grating Littman-type dye lasers[43], DL1 and DL2 of Fig. 2.2. Both dye lasers were constructed using 1200 lines/mm diffraction gratings at grazing incidence with the

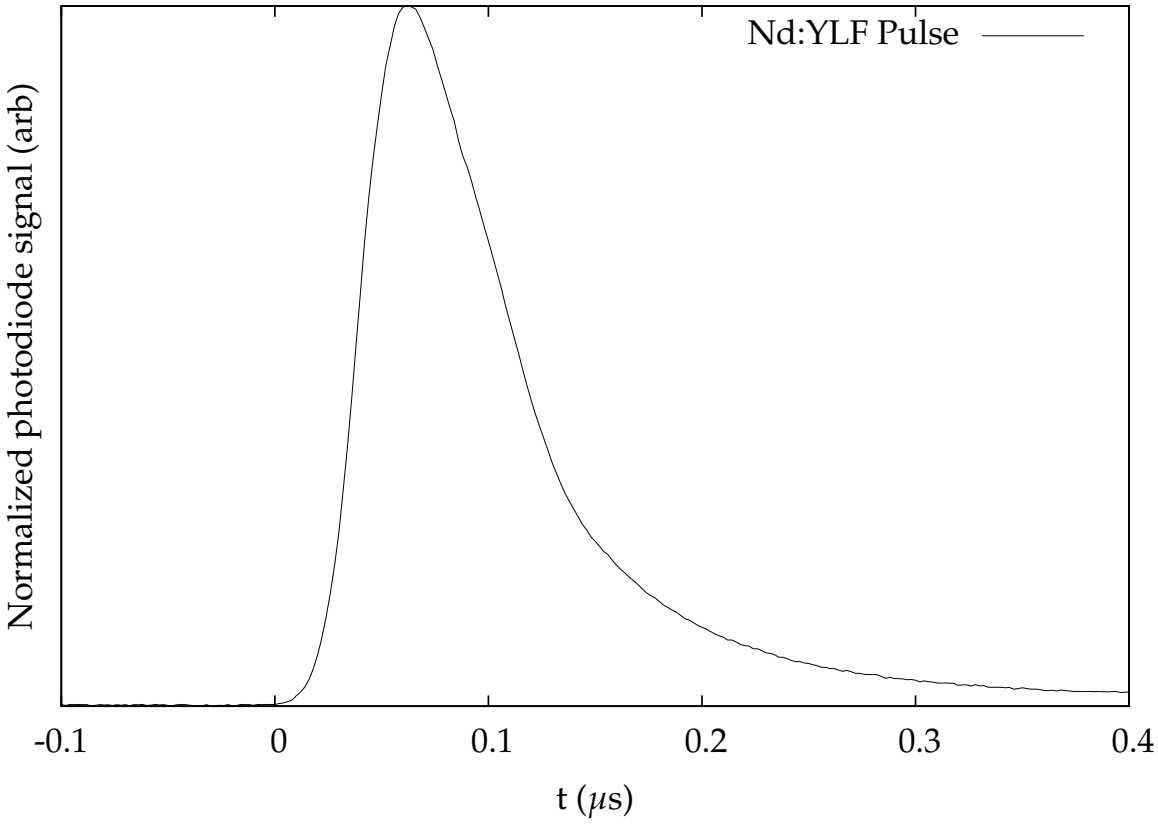

Figure 2.5: Coherent Evolution-30 Nd:YLF laser pulse shape before Pockels cell system

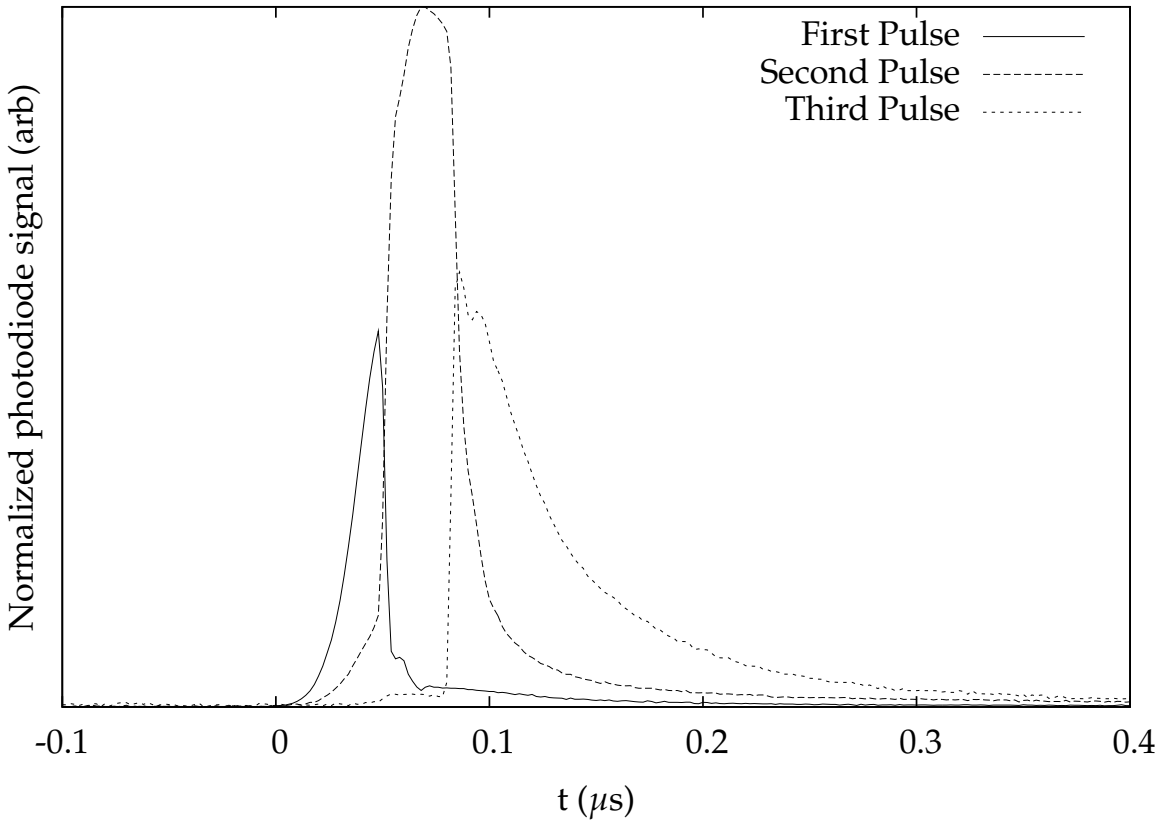

Figure 2.6: Coherent Evolution-30 Nd:YLF laser pulse shape after Pockels cell system.

output taken from the zeroth order reflection. DL1 uses DCM in dimethyl sulfoxide (DMSO) at a molar concentration of 1×10^{-3}. DL2 uses LDS-821 dissolved in methanol at a molar concentration of 1.5×10^{-4}. The second pulse, also split by a 50-50 beam splitter (BS2), pumps a double grating Littman-type dye laser[50], DL3 of Fig. 2.2, and a single-pass amplifier (A1). DL3 was constructed using two 1800 lines/mm diffraction gratings. Rhodamine-640 in molar concentrations 5×10^{-4} (oscillator) and 1×10^{-4} (amplifier) was used to characterize the dye laser. The third pulse, with an average power of 3.5 W, is sent to a beam dump but could easily be used to pump additional dye lasers or amplifiers. When pumped with 16 ns 2.2 mJ pump pulses, DL1 produces 12 ns laser pulses over a tuning range from 625 nm to 695 nm, centered around 660 nm. The measured temporal pulse shape is

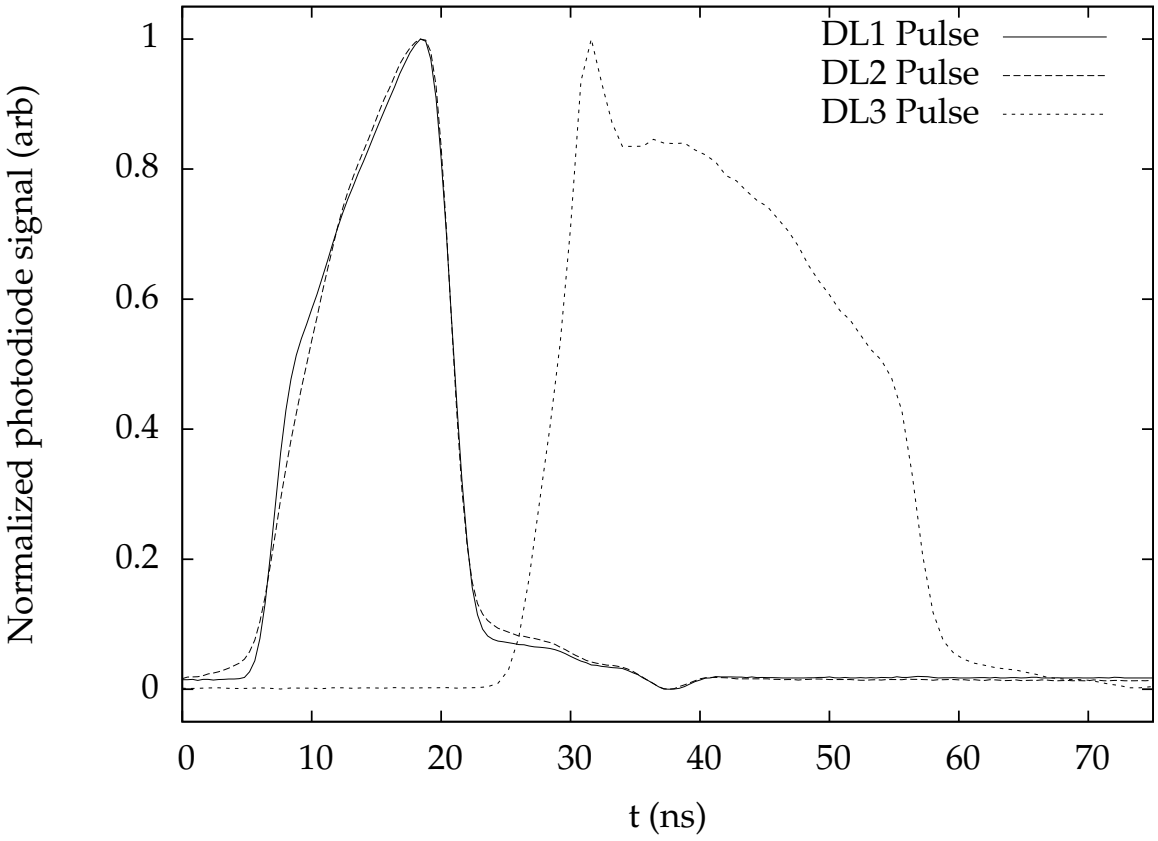

Figure 2.7: Dye Laser characteristics. Dye laser pulse shapes for DL1-3. DL1 and DL2 were both pumped by a 16 ns 2.2 mJ pump pulse, DL3 was pumped by a 35 ns 2.1 mJ pump pulse. These pump pulses are shown in Fig. 2.6.

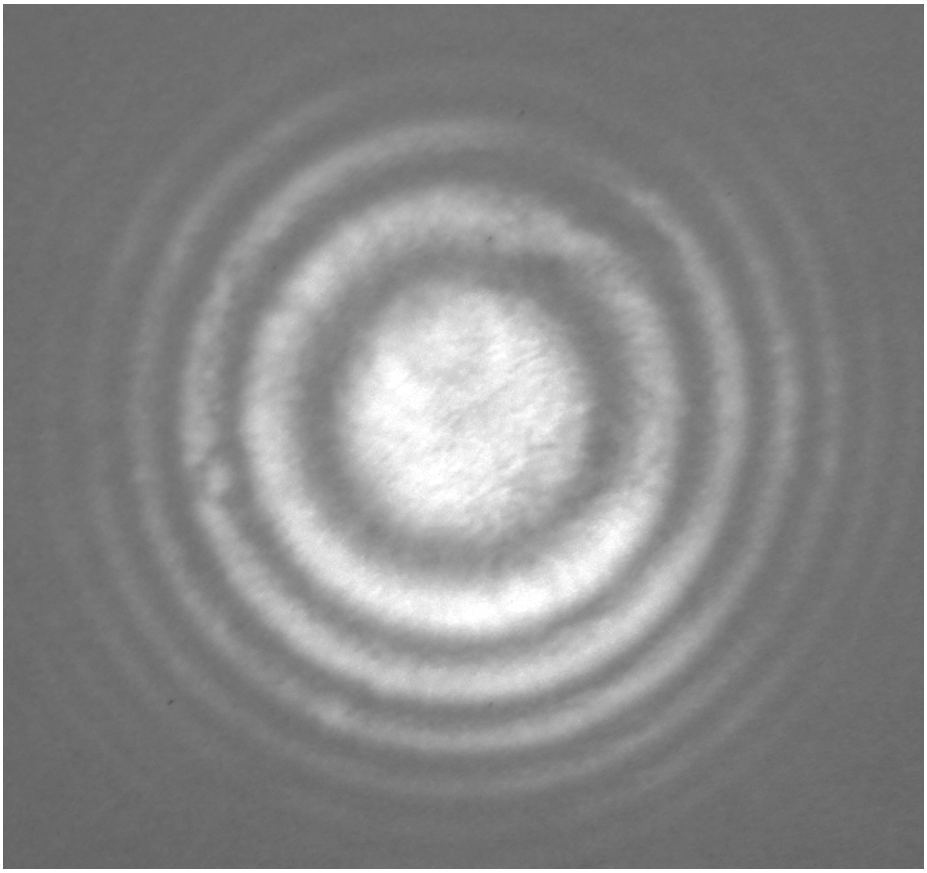

Figure 2.8: Etalon (20 GHz FSR) fringe pattern for DL1 tuned to 671 nm, averaged over 33 laser shots.

shown in Fig. 2.7, and the measured tuning curve is shown in Fig. 2.9. Typically, this laser produces 21.4 μJ per pulse at 671 nm with a linewidth less than 10 GHz (0.33 cm^{-1}.) An example 20 GHz FSR etalon fringe pattern at a laser output of 671 nm, averaged over 33 laser shots, is shown in Fig. 2.8.

When tuned to 813 nm, DL2 produces 14.4 μJ per pulse delivered in 12 ns. The pulseshape is shown in Fig. 2.7. The tuning range of this laser is 800 nm to 840 nm with a linewidth less than 10 GHz (0.33 cm^{-1}.)

The third dye laser oscillator produces 3.72 μJ per pulse at 615 nm before the amplifier stage when pumped with 35 ns 2.1 mJ pulses, and 36 μJ per pulse after the amplifier stage. The post-amplifier pulse shape is shown in Fig. 2.7. The linewidth

of this laser was measured to be as good as 3 GHz, and is typically 4.5 GHz. The laser frequency is computer controlled using a small stepper motor system to adjust the end diffraction grating angle. We measure the relative frequency of the third laser by monitoring its transmission through a 20 GHz free spectral range etalon, and the absolute calibration is provided by the 16274.0212 cm^{-1} $2p^5(2p_{3/2})3s - 2p^5(2p_{3/2})3p$ Ne line observed as an optogalvanic signal. The uncertainty in the laser frequency calibration is 3.6 GHz.

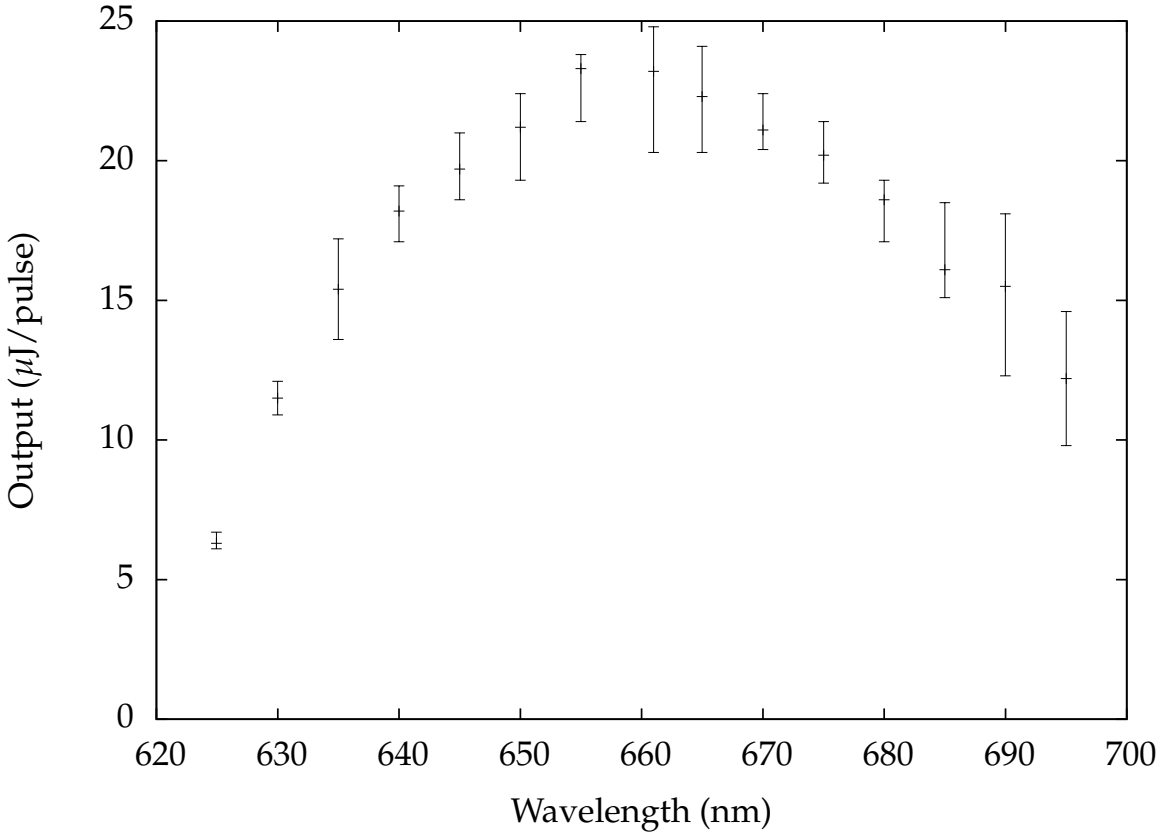

Figure 2.9: Dye Laser characteristics. Tuning curve for DL1 characterized with DCM in DMSO at a molar concentration of 1×10^{-3}.

The thermal beam of ground state lithium atoms can therefore be laser excited to np Rydberg states by the scheme: $2s \rightarrow 2p \rightarrow 3s \rightarrow np$.

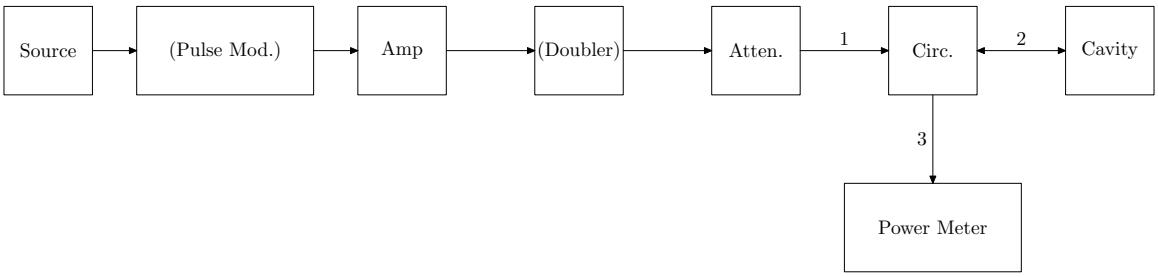

Figure 2.10: Microwave system schematic diagram. Items in parentheses are optional.

2.4 Microwave components

2.4.1 Overview

Conducting experiments on the microwave ionization of excited atoms requires complete control of the production of microwave pulses with well-defined frequency, amplitude, duration, and polarization. The general scheme for the production of microwave pulses is shown in Fig. 2.10.

The microwave source is either an HP 83620A 0.01-20ĠHz 8360 Series Synthesized Sweeper or an HP 8350B Sweep Oscillator with 83550A 8-20 GHz plug-in. In the case of the sweep oscillator, microwave pulses are made from the continuous wave (CW) output using a Hewlett Packard 11720A pulse modulator, connected using SMA cables. The pulse modulator has a contrast ratio of 60 dB with a rise time of 10 ns. All microwave components below 26 GHz are connected using SMA cables. The sweep oscillator exhibits small thermal frequency drifts, and use of the synthesized sweeper is preferable when using a Fabry-Perot cavity. The synthesized sweeper also has a modulated output option to create microwave pulses with a contrast ratio of 80 dB and a rise time below 50 ns.

For experiments above 26 GHz, an active microwave frequency doubler is then used to generate microwaves between 26 and 40 GHz. Whether frequency doubled

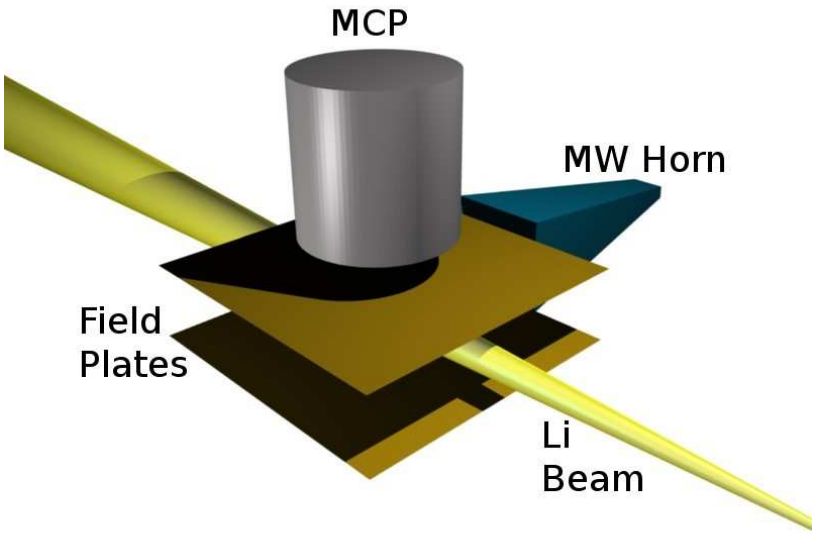

Figure 2.11: Experimental apparatus. The Li beam (yellow), field plates, horn and MCP detector are shown.

or not, a microwave amplifier is next used. Below 18 GHz, either a Miteq MPN4-02001800-23P 250 mW solid-state amplifier or a Hughes 8020H traveling wave tube amplifier is used. The former amplifier is preferable when using a microwave horn and high powers are not required, the latter when using a Fabry-Perot cavity removes concerns about microwave amplifier noise. There were a variety of reasons for choosing a microwave horn for the experiment over a waveguide or cavity setup. The horn allows for short microwave turn on and off times while avoiding egregious stray field problems, unlike the cavity or waveguide setups, respectively. However, the horn microwave field amplitude that the lithium atom beam is exposed to is not as easily known as when using a waveguide or cavity. The horn can be calibrated by comparing experimental data to similar results using a cavity or waveguide setup. However, conducting these experiments in a piece of WR-62 or smaller waveguide is not feasible due to the small distance between the interaction region and the waveguide walls.

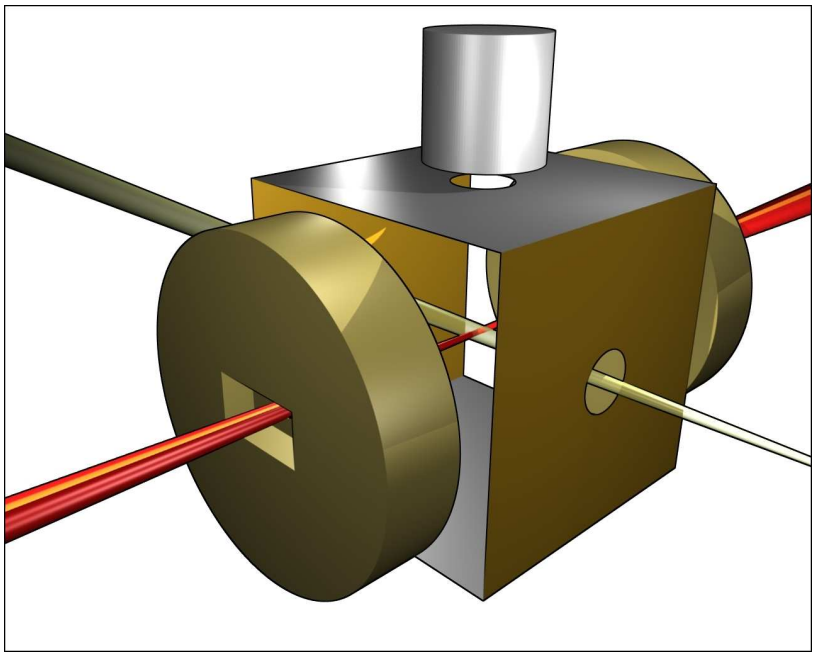

Figure 2.12: Experimental apparatus. The Li beam (yellow), dye laser pulses (red, orange, red), field plates, Fabry-Perot cavity, and MCP detector are shown. The four field plates and two brass cavity plates are all electrically isolated from one another.

The microwave amplifier output is connected to either a set of HP 8495B (70 dB) and 8495B (11 dB) step attenuators or a HP R382A (50 dB) variable attenuator to select a microwave power while keeping the microwave signal to noise power ratio constant. Finally, a 10 dB directional coupler is used to measure the reflected power when the Fabry-Perot cavity is used for power calibration. For microwave frequencies below 26 GHz, a SMA vacuum feed-through brings microwave power into the vacuum chamber to either a three-inch microwave horn or Fabry-Perot cavity. Above 26 GHz WR-28 waveguide is used to connect microwave components, with a small mica disk separating vacuum and atmosphere in the waveguide.The experimental apparatus with a horn is shown in Fig. 2.11. The experimental apparatus with a Fabry-Perot cavity is shown in Fig. 2.12.

2.4.2 Microwave Calibration

One of the key reasons for employing a Fabry-Perot cavity is that it makes calculating the field amplitude at the center of the cavity relatively straightforward. Our goal for this subsection is to calculate the electric field amplitude at the central antinode, E, based on measurable quantities. A more extensive discussion can be found in Ramo and Whinnery[51].

Experimentally, the power loss per cycle in the cavity is small and gaussian optics are applicable to describe the electric field in the cavity. The electric field in the cavity can be written as,

$$E(r,z) = E\psi(r,z)cos(kz - \phi(z))cos(\omega t), \tag{2.2}$$

where $\psi(r,z)$ is the profile amplitude, k is the wavenumber, $\phi(z)$ is the phase, and ω is the cavity angular frequency. The profile amplitude, $\psi(r,z)$ is written as,

$$\psi(r,z) = \frac{W_0}{W(z)} e^{-\frac{r^2}{W(z)^2} - \frac{ikr^2}{2R(z)}}, \tag{2.3}$$

where $W(z)$ is the beam waist, W_0 is the center beam waist, and R(z) is the radius of curvature of the wavefronts. These are defined as,

$$W_0^2 = \frac{\lambda}{2\pi}\sqrt{2Bd - d^2}, \tag{2.4}$$

$$W(z) = W_0\sqrt{1 + (\frac{\lambda z}{\pi W_0^2})^2}, \tag{2.5}$$

$$R(z) = z(1 + (\frac{\pi W_0^2}{\lambda z})^2), \tag{2.6}$$

respectively, where B is the mirror radius of curvature, d the distance between mirror centers, and λ the microwave wavelength[47]. The phase, $\phi(z)$, is defined

as,

$$\phi(z) = arctan(\frac{\lambda z}{\pi W_0^2}) \tag{2.7}$$

Since the energy in the cavity oscillates between the electric and magnetic fields, we can simply find the total energy stored, U, when the electric field is a maximum and the magnetic field is zero.

$$U = \frac{\epsilon_0}{2} \int E(r,z)^2 dV \tag{2.8}$$

We can rewrite the stored energy in terms of the microwave angular frequency, ω, the power lost in the cavity, P_L, and the cavity Q, where Q is the fractional power loss per cycle.

$$U = \frac{P_L Q}{\omega} \tag{2.9}$$

The cavity Q is measured by the frequency width where the amplitude response is $1/\sqrt{2}$ of the resonance value at a given frequency, f, known as half-power points.

$$\frac{\Delta f}{f} \approx \frac{1}{Q} \tag{2.10}$$

For our 17 GHz cavity, the cavity Q is ≈ 2900.

We can redefine the energy stored in the cavity, Eq. (2.8), in terms of the field amplitude at an antinode, E, and the effective volume of the cavity, V_{eff}. V_{eff} is defined as

$$V_{eff} = \frac{4}{E^2} \int_V d^3 r E(r)^2, \tag{2.11}$$

making the energy stored in the cavity,

$$U = \frac{\epsilon_0}{2} E^2 \frac{V_{eff}}{4}. \tag{2.12}$$

Equating Eqs. (2.9) and (2.12) and solving for the field amplitude yields,

$$E = \sqrt{\frac{8P_L Q}{\epsilon_0 \omega V_{eff}}}. \tag{2.13}$$

To calculate the microwave field amplitude, E, it is now only necessary to measure the power loss and Q of a cavity at a given frequency, and the geometric dimensions of the cavity to calculate the effective volume.

Substitution of Eq. (2.2) into Eq. (2.11) is explicitly written as,

$$V_{eff} = 16\pi \int_0^\infty r dr \int_0^{d/2} dz |\psi|^2 cos^2(kz - \phi). \tag{2.14}$$

Further substitution of Eqs. (2.3), (2.4), (2.5), (2.6) and (2.7) into Eq. (2.14) allows for calculating the effective volume in terms of the cavity geometry and a microwave wavelength. For our cavity the effective volume is 91 cm^3 at $f = 17$ GHz.

Returning to Eq. (2.13), in order to calculate the microwave field strength the power loss, P_L, must be measured. This is simply done with a microwave circulator or directional coupler and a power meter. A circulator has three ports, numbered one through three, and a signal input on port one is sent to port two. Microwave signals sent to port two are sent to port three, and signals to port three are sent to port one. Terminating port three with a 50 Ω terminator would create a microwave isolator. For frequencies below 18 GHz, port one of a Trak 10B2201 microwave circulator is connected to the microwave amplifier output, and port two is connected to the SMA coupler on the cavity mirror. A microwave power meter is connected to port three. All microwave power measurements have been taken with an HP 432A Power Meter with 8478B thermistor mount, a thermal power meter capable of measuring CW microwaves between 0.001 and 10 mW (40 dB) over a frequency range from 10 MHz to 18 GHz. The power meter has a measurement accuracy of

1%. The power lost is the difference in reflected CW power measured on port three of the circulator between resonance and non-resonance in the cavity.

The microwave cavity is stable over the course of a day, and the cavity Q, center frequency, and power coupling are checked daily.

2.5 Vacuum System

Sadly, these experiments cannot be conducted at atmospheric pressure. The impetus for conducting experiments in a vacuum is clear after a simple back of the envelope calculation of the mean free path of molecules. From the Maxwell-Boltzmann velocity distribution,

$$\bar{v} = \sqrt{\frac{8kT}{\pi m}} \tag{2.15}$$

For an atmospheric N_2 molecule, $\bar{v} = 476\,\mathrm{m/s}$. The average number of collision per second, Z, can be computed as,

$$Z = \sqrt{2} n \pi \xi^2 \bar{v}, \tag{2.16}$$

where n is the number density and ξ is the molecular diameter[52]. For N_2, ξ is roughly $3 \times 10^{-8}\,\mathrm{cm}$ and n is $2.7 \times 10^{19}\,\mathrm{cm}^{-3}$ at atmospheric pressure. Therefore the mean free path is simply,

$$\lambda = \frac{\bar{v}}{Z} = \frac{1}{\sqrt{2} n \pi \xi^2}. \tag{2.17}$$

This works out to be 92 nm for atmospheric N_2. For Rydberg atoms the collision cross-section can be quite large for even a dilute sample of highly excited atoms, scaling as n^4, and interaction with a background gas can cause initial state depopulation[5]. Since the mean free path is inversely proportional to number

density, we can call on the ideal gas law to conclude that mean free path is also inversely proportional to pressure. We can increase the mean free path beyond the 1 m distance scale of our vacuum chamber by simply decreasing the background pressure of our chamber below 10^{-6} torr.

The vacuum technology used in these experiments is a standard two-stage setup comprised of a mechanical belt-driven roughing pump and high-vacuum diffusion pump. Mechanical pumps are capable of bringing a vacuum chamber from atmospheric pressure down to close to 10^{-3} torr.

Diffusion pumps provide the second stage of pumping, covering the range of 10^{-3} to 10^{-8} torr, with background pressures in the 10^{-7} more typically seen on large chambers with many flanges. Diffusion pumps are experimentally ideal in that they have no moving mechanical parts to break and are generally not a source of electric noise. An electrically heated boiler sits at the bottom of the pump and vaporizes oil, which is conducted up through a central tower to a jet nozzle. The nozzle sends the oil vapor downwards and outwards towards the water cooled walls of the pump. The vapor condenses on the pump walls and runs down to the boiler for recirculation. System gases are trapped by momentum transfer in the vapor stream, pushed to the bottom of the pump, and eventually removed by the backing pump[53].

The diffusion pump is a three stage, water cooled, Edwards Diffstak 160/700M, with a nitrogen pumping speed of 700 liter/s[54]. The diffusion pump takes a standard fluid charge of 250 ml of Santovac 5. The diffusion pump is backed by a Welch 1376 Duo-Seal mechanical pump, connected by an Edwards BRV25 Backing Roughing Valve.

A background pressure of 1×10^{-6} torr can be easily reached within a few hours of pumping, and 7×10^{-7} after a day of pumping. Our typical operating

background pressure of 2×10^{-7} can be reached by employing a small liquid nitrogen cold trap inside the chamber. A copper cylinder sits inside the vacuum chamber with a tube allowing liquid nitrogen at atmospheric pressure to be poured inside the cylinder.

Pressure measurement is done via both a thermocouple gauge and a Bayard-Alpert type ionization gauge. The thermocouple gauge, which measures the thermal conductivity of a gas, covers a pressure range from 10^{-3} torr to almost atmospheric pressure. For pressures below 10^{-3} torr, a Bayard-Alpert type ionization gauge is used for pressure measurement. Gas molecules inside the gauge are ionized by electron impact from a hot filament grid and the resultant positive ions are collected by a negative biased electrode. The electrode current is inversely proportional to the pressure in the gauge, and can measure pressure in the range of 10^{-9} to 10^{-3} torr. The ionization gauge also creates a small pressure gradient; ions accelerated to the collector are often embedded and effectively removed from the system. The ion gauge itself pumps on the system, with a typical pumping speed of 200 mL/s[53]. Typically Schott glass iridium or tungsten filament gauges are used. Iridium B-A ion gauges can be briefly operated at air without failure, whereas tungsten filament gauges are more robust to diffusion pump oil backstreaming and usually have an accessible second filament by reversing the cable connector connecting the ion gauge to the ion gauge controller[55].

2.6 Electronics and Data Acquisition

The master clock for the experiment is the Evolution laser Q-switch sync output, which occurs exactly 2.515 μs before the last dye laser pulse reaches the interaction region at a repetition rate of 1 kHz.

All of the experimental timing is controlled by two SRS DG535 Four Channel

Digital Delay/Pulse Generators. The first delay generator is triggered by laser Q-switch sync out, the other delay generator is triggered by the first. The first DG535 controls the timing of the two laser Pockels cells and the field ionization pulse trigger. The second DG535 controls the timing of the pulse via the CD output, where the D channel delay can be altered by the computer over GPIB. Optionally, the second DG535 can be triggered not by the first delay generator, but instead by the output of a simple divide-by-two IC. This allows for the microwave pulse to occur every other laser shot, at 500 Hz, allowing for normalization data.

2.6.1 Pockels Cells Electronics

The essential idea behind a Marx-bank is to charge a number of capacitors in parallel, then discharge them in series. The circuit used is shown in Fig. 2.13. The switches require a +1 kV DC input and a TTL trigger pulse from a SRS-DG535 Delay/Pulse Generator. Stable output of the -4 kV output pulse is sensitive to the amplitude of the input DC voltage and of the trigger pulse. Increased switching stability is clearly seen when the trigger voltage is increased. Best results come from using the DG535 back-panel output at 30 V. The switches usually require between 700 V and 1.5 kV for stable operation, with an increase in input voltage increasing the output amplitude and giving a faster risetime. Interestingly, these transistor based Marx bank switches themselves are an active area of research[56]. Proper construction and operation of these switches requires transistors with a gaussian doping profile, such as the Motorola 2N5551 transistors[57]. Most non-Motorola 2N5551 transistors are uniformly doped rather than gaussian doped, like the Motorola 2N5551. Uniformly doped 2N5551 transistors consistently fail after only a few thousand cycles. When properly constructed with gaussian doped transistors, these switches last for greater than 10^9 operating cycles without fail. Unlike com-

mercial solutions, costing in excess of $5000, these switches cost only a few dollars each and can be made in a few hours.

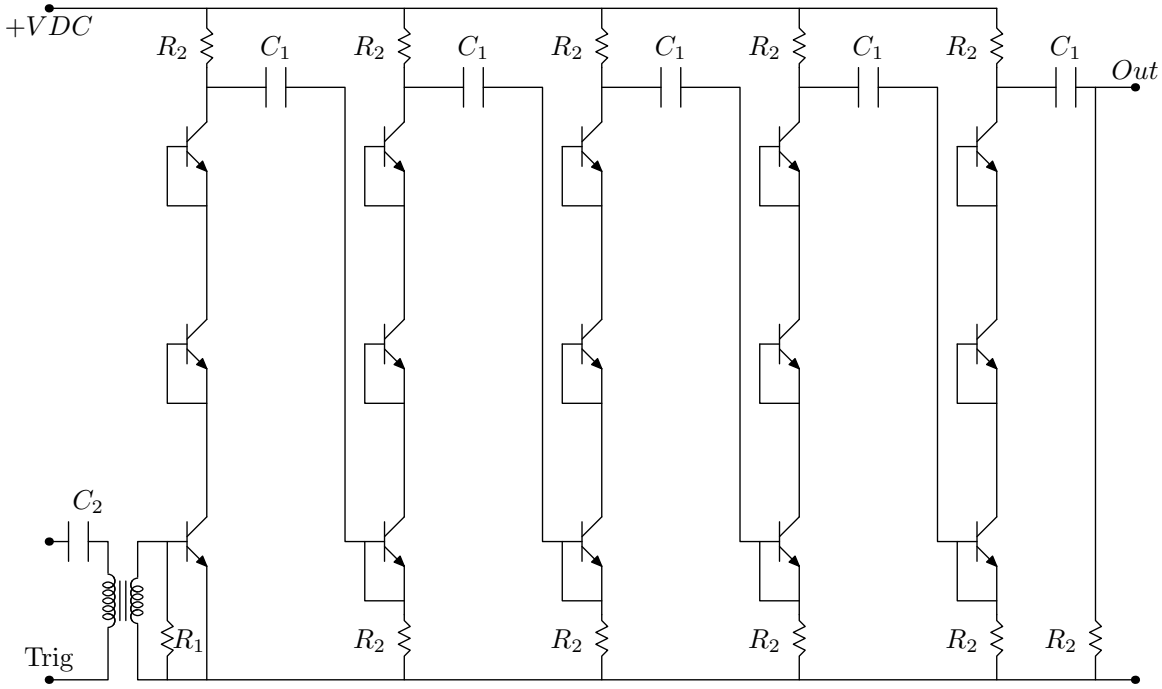

Figure 2.13: Marx bank circuit for generating Pockel's cell voltage. The circuit uses fifteen Motorola 2N5551 NPN transistors. $C_1 = 1\,\text{nF}$, $C_2 = 20\,\text{pF}$, $R_1 = 50\,\Omega$, and $R_2 = 680\,\text{k}\Omega$. The input voltage, $+VDC$, can be adjusted between 700 V and 1.5 kV.

2.6.2 Field Ionization Pulsers

For the experiments in this dissertation, excited atoms that survive microwave interaction are detected by means of field ionization. The combined Coulomb-Stark potential can simply be written as

$$V = -\frac{1}{|z|} + Ez, \tag{2.18}$$

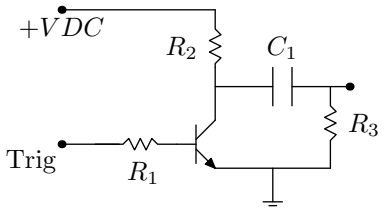

Figure 2.14: Fast rising field ionization pulse circuit diagram. For the constructed circuit $R_1 = 2.8\,\mathrm{k}\Omega$, $R_2 = 10\,\mathrm{k}\Omega$, $R_3 = 50\,\Omega$, and $C_1 = 1\,\mathrm{nF}$.

along the z axis. The $dV/dz = 0$ saddle point is at $z = -E^{-1/2}$. If the electron is bound by an energy W, the field required for ionization is

$$E = \frac{W^2}{4}. \tag{2.19}$$

Equation (2.19) sets the condition for field ionization to occur, and the rest of this section will deal with the experimental creation of these fields. An electric field pulse creates easily detectable charged particles and accelerates them towards a charged particle detector. Two differing field ionization schemes are used. A fast rising pulse is used for high efficiency detection where a signal proportional to the number of surviving atoms is recorded. A slow rising pulse exploits the ionization field n^{-4} dependence to temporally separate final states and is used when the distribution of final states is recorded.

Fast Rising Pulse

The fast rising field ionization pulse is created using a single avalanche transistor[58]. A Zetex ZTX415 avalanche transistor allows for up to 260 V pulses in 3.5 ns. A schematic diagram is shown in Fig. 2.14. Although the circuit operates without fail over more than 10^9 cycles, it is rather sensitive to input DC voltage. The specific circuit used for these experiments required +289 VDC source, with a tolerance of less than $\pm 0.7\%$.

Slow Rising Pulse

The slow rising field ionization pulse is based on a ILC T-105 trigger transformer. The pulser allows for voltages of up to 800 V with a rise time of 2 μs.

2.6.3 Microchannel Plate Dectector

Charged particle detection occurs via a dual microchannel plate (MCP) assembly. A microchannel plate consists of a thin glass disk of densely packed channels with a large potential difference between the front and back faces of the plate, typically 700-1200 V. For these experiments electrons were typically detected, although positive ion detection is possible by simply reversing the polarity of the applied potential. An electron entering a channel hits a channel wall and creates a rapid cascade of electrons which is collected by an anode[59]. Below saturation this system creates a linear current proportional to the number of electrons incident on the detector face. The gain of a MCP plate is typically 10^4. A second microchannel plate is used to increase the gain of the detector. The two plate detector setup is usually operated with a 1900 V potential across the two MCP plates.

2.6.4 Data Acquisition

The signal from the MCP is amplified using either an HP 8447F 0.1-1300 MHz 22 dB gain amplifier, or an HP 416A 40 dB gain amplifier. The signal is sent through an SRS 250 Gated Integrator & Boxcar Averager, and passed through to a Tektronix TDS 3052 500 MHz 5 GS/s oscilloscope. The SRS 250 and TDS 3052 are both triggered by the laser Q-switch sync TTL pulse. The last sample output of the SRS 250 is connected to the data acquisition board of the computer, and computer voltage sampling is triggered by the "busy" output of the SRS 250. I have writ-

ten data collection software using the National Instruments LabView framework which records the MCP, etalon, optogalvanic, and microwave trigger signals while controlling the excitation laser frequency via a stepper motor. When final-state distribution data is needed the 256 or 512-shot averaged oscilloscope trace is recorded by the computer via the GPIB protocol. Completing a transfer of the oscilloscope trace from the scope to the computer effectively takes on the order of half a second, during which the oscilloscope does not record data. Averaging many laser shots on the oscilloscope before transferring data to the computer keeps the effective data acquisition rate closer to the 1 kHz laser pulse repetition frequency than a few Hz maximum GPIB transfer rate.

Chapter 3

Multiphoton Microwave Ionization at 17 GHz

In this chapter I discuss first experiments of multiphoton ionization approaching the photoionization limit using 17 GHz microwave pulses. Previous published experimental investigations of microwave ionization have spanned a range of scaled frequency from $0.01 < \Omega < 6$[24, 28, 60]. In the following chapter I will examine a range of scaled microwave frequency from scaled frequency $\Omega \approx 2$ to beyond the $\Omega = n/2$ photoionization limit.

3.1 Initial Hypothesis

As previously discussed, perturbative N-photon ionization of ground state atoms is an N-th order process[9–12, 61]. Consequently, we initially expected N-photon ionization to scale as I^N, where I is the microwave intensity. Two-photon ionization is more difficult than single photon ionization. Three-photon ionization is more difficult than two-photon ionization. This would yield atomic spectra similar to the calculated spectra cartoon shown in Fig. 3.1.

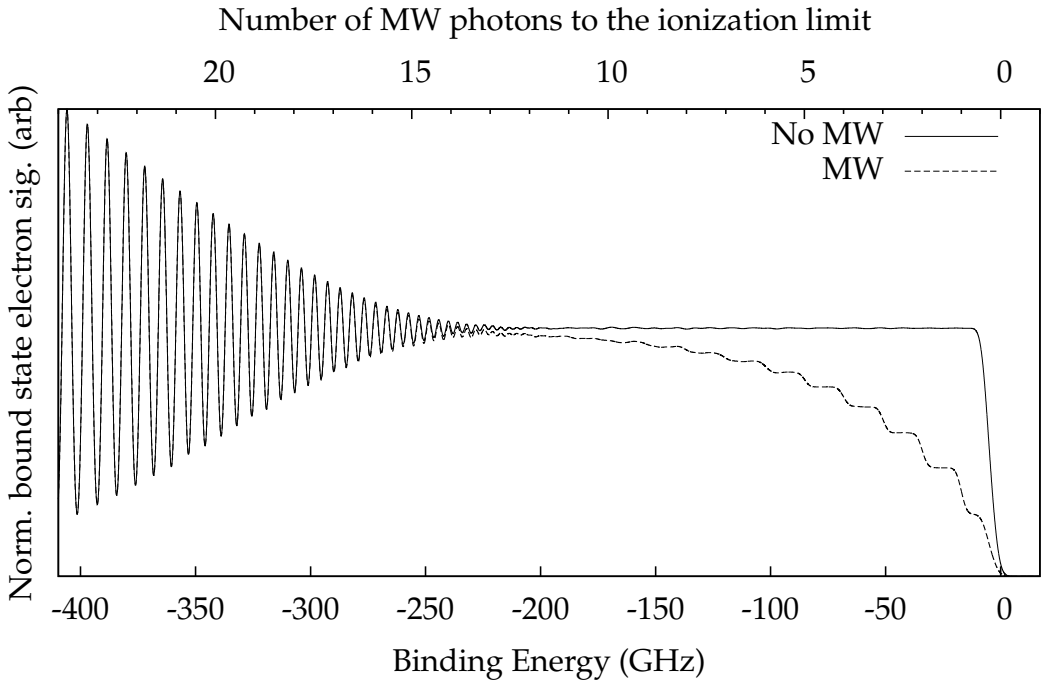

Figure 3.1: Calculated microwave ionization spectra expected for ionization as an I^N process, as a function of binding energy.

3.2 Experimental Results

The experiment setup used for this investigation is described in Chapter 2, and specific details will be illustrated below. The relevant timing diagram is shown in Fig. 2.1. Typically a microwave pulse from 20 ns to 2 μs long is injected into the cavity 100 ns after the laser excitation. One microsecond after the laser pulse we apply a negative voltage pulse to a plate below the cavity to field ionize the atoms not ionized by the microwaves and eject the electrons through a hole in the plate above the cavity. The electrons are detected with a microchannel plate detector, and we record the signal with a gated integrator. Electrons produced by photoionization or microwave ionization leave the interaction region before the voltage pulse and are not detected.

The microwave cavity consists of two brass mirrors of 102 mm radius of curvature separated by 79.1 mm on the horizontal cavity axis. We operate the cavity on

the TE_{06} mode at 17.068 GHz with quality factor $Q = 2900$. With this Q the decay or filling time of the energy in the cavity, $\tau = 27$ ns, sets a lower limit on the pulse length we can use. The maximum field amplitude we can produce in the cavity is 200 V/cm, and we are able to determine the microwave field with an uncertainty of 8%.

3.2.1 Microwave power

The recorded spectra for 200 ns microwave pulses at various field amplitudes is shown in Fig. 3.2. Data points are averaged over 200 laser shots and the microwave pulse is applied on alternating shots for data normalization. In comparison to Fig. 3.1, there are clear differences.

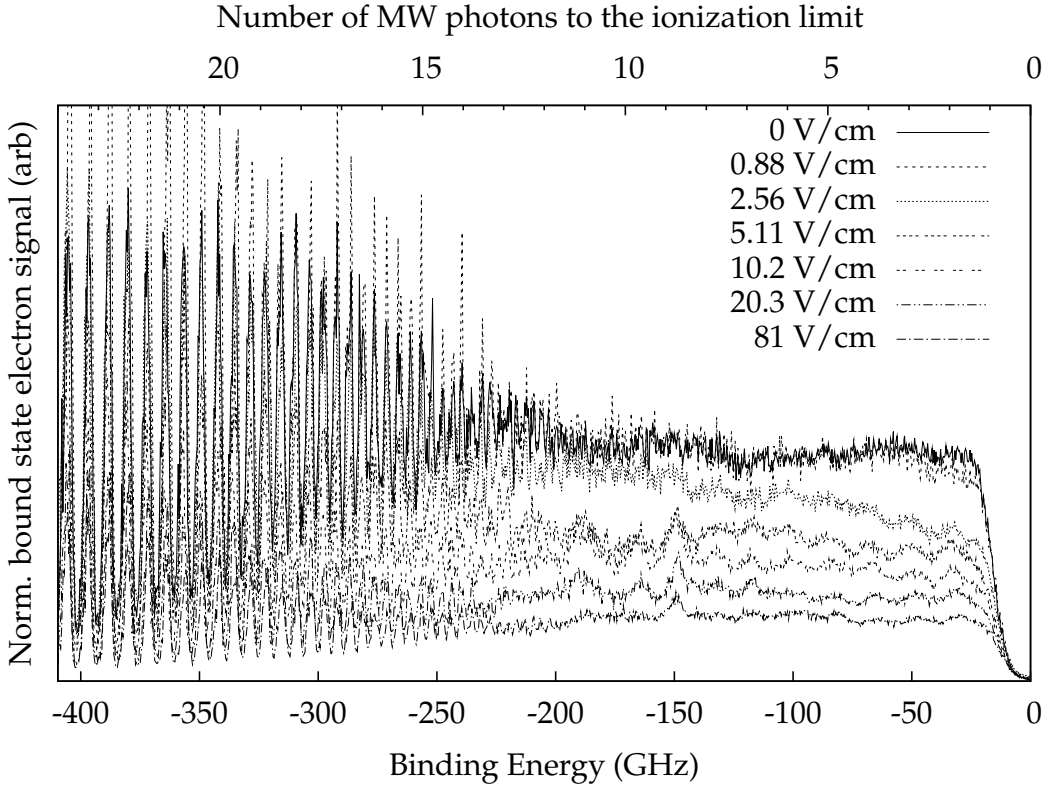

Figure 3.2: Bound state electron signal as a function of binding energy in GHz, for microwave fields from 0 V/cm to 81 V/cm.

We can find the microwave field required for 10% and 50% ionization to compare to theoretical predictions by interpolating between the spectra at a given binding energy, shown in Fig. 3.3. The 50% ionization field is between 5 V/cm and 15 V/cm over the entire range from a binding energy of 400 GHz to the ionization limit.

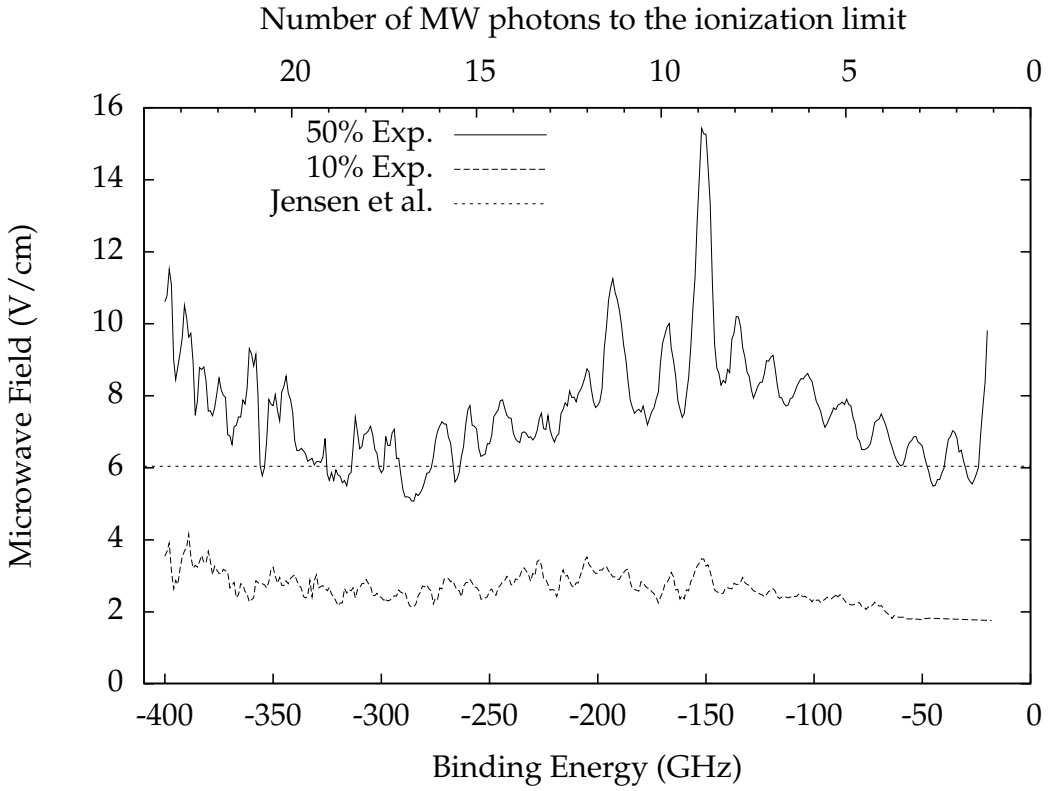

Figure 3.3: Threshold microwave field required for 10% and 50% ionization as a function of binding energy, compared to theoretical prediction of Jensen *et al.*

Microwave ionization in this regime clearly does not scale as I^N, and a comparison between ground state ionization and our excited atom microwave ionization results is shown in Fig. 3.4. Ground state ionization experiments by l'Huiller *et al.*[61], who focused 50 ps laser pulses of up 0.2 J on ground state Xe and Xe^+ atoms, are shown in Fig. 3.4a.The microwave ionization data are plotted in Fig. 3.4b.

Both figures are plotted on a vertical scale that spans eight orders of magnitude,

yet the results shown in Fig. 3.4b spans less than an order of magnitude over 24 microwave photons.

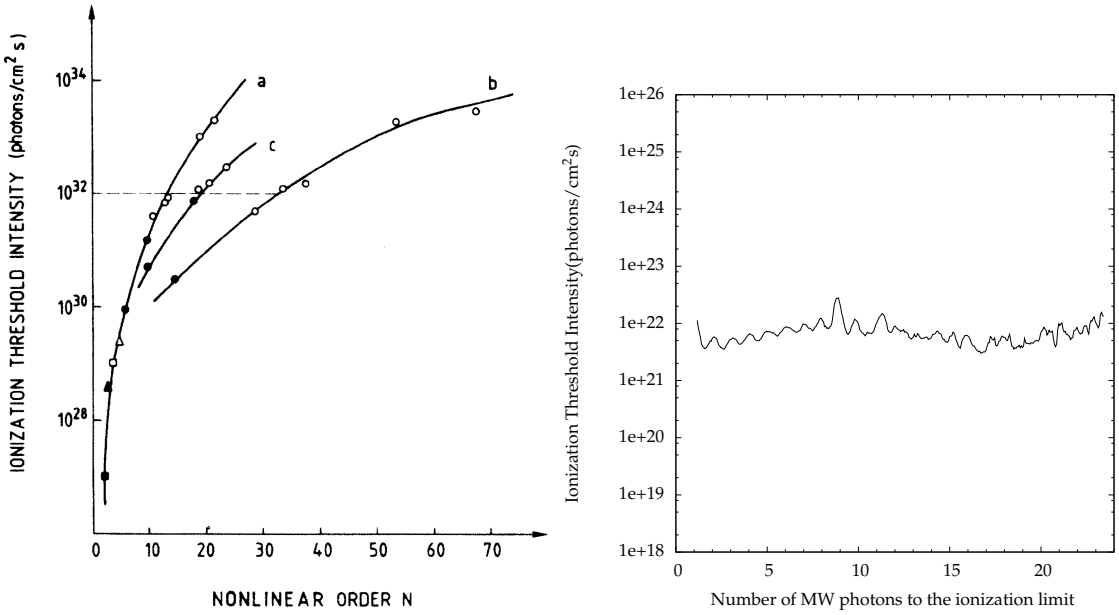

Figure 3.4: Experimental comparison of ground-state multiphoton ionization and Rydberg multiphoton microwave ionization. Figure(a) Results of l'Huillier *et al.*[61] for multiphoton ionization of ground state Xe and Xe^+ atoms, and (b) results of Fig. 3.3 plotted as ionization threshold intensity as a function of the number of microwave photons to the ionization limit.

3.2.2 Bias Voltage

As previously seen at lower values of scaled frequency, an important aspect of these measurements is the control of stray fields[26, 28]. In addition to the plates above and below the cavity there are plates on either side of the cavity, as shown in Fig. 2.12. Applying bias voltages to these four plates and the cavity mirrors enables us to reduce the stray field at the center of the cavity to below 5 mV/cm. The minimum stray field is determined by minimizing the microwave ionization with the laser tuned slightly below the ionization limit. A stray field in the direction

of the microwave field is much more effective in lowering the microwave field required for ionization than a perpendicular field, presumably because it leads to a non-zero average field in the direction of the stronger oscillating microwave field[62].

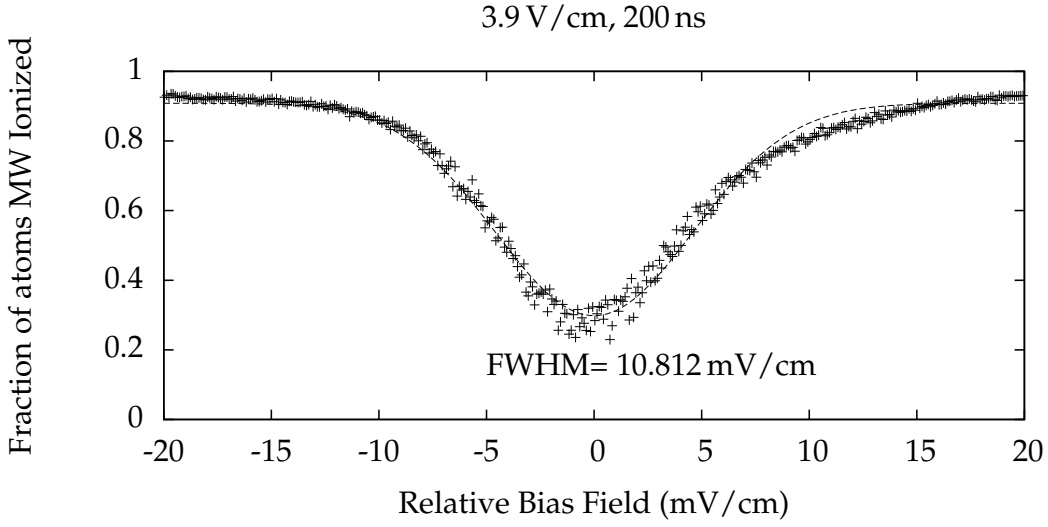

Figure 3.5: Microwave ionization population fraction as a function of external bias field, for binding energy 3 microwave photons from the ionization limit. This corresponds to $n \sim 253$. The plotted curve is a fitted gaussian with FWHM of 10.8l2 mV/cm.

Rather than scan the laser excitation frequency for a fixed field, we can set the laser frequency and scan the voltage on a field plate to measure the fractional ionization as a function of bias field. An example is shown in Fig. 3.5 at a binding energy of 54 GHz. That ionization is easier in an applied field leads to an easy technique to nullify any stray field in the interaction region. Simply applying a microwave pulse to ionize some, but not all, excited atoms while adjusting the applied voltage on a field plate to minimize the microwave ionization signal quickly cancels any stray field in the experimental region. Iterating this process over the six field plates in the chamber reduces the stray field, as seen by the $1/9n^4$ depression in the ionization limit, to within 5 mV/cm. Unlike other methods that require

laser linewidths on the order of MHz or better[63, 64], this technique places no strong requirements on the laser linewidth, microwave frequency or field amplitude. The sensitivity to external fields places no strong limitations on the binding energy of the excited atoms, as shown by Fig. 3.6 for a set of bias fields applied to the top plate from 0 to 10 mV/cm, plotted as a function of the binding energy of the excited atoms. The fraction of atoms microwave ionized is always smallest in zero bias field for the entire range of binding energies shown, from -160 GHz to the ionization limit.

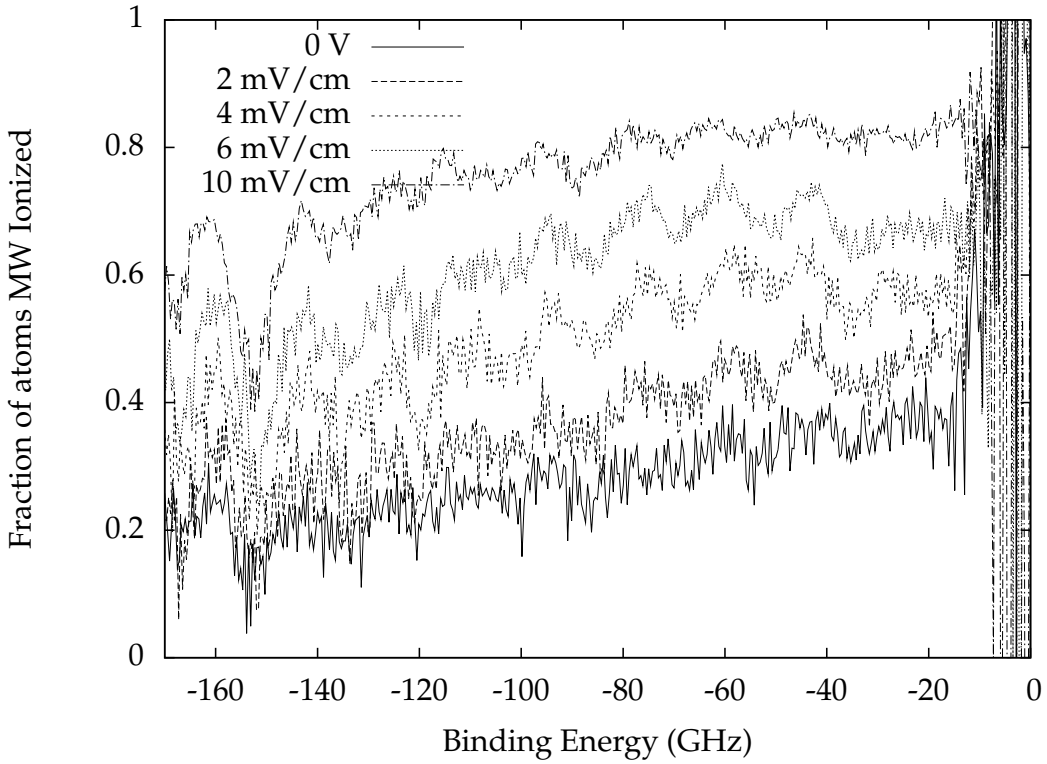

Figure 3.6: Fraction of atoms microwave ionized by a 200 ns 3.9 V/cm 17 GHz microwave pulse as a function of binding energy, for bias fields from 0 to 10 mV/cm in the vertical direction.

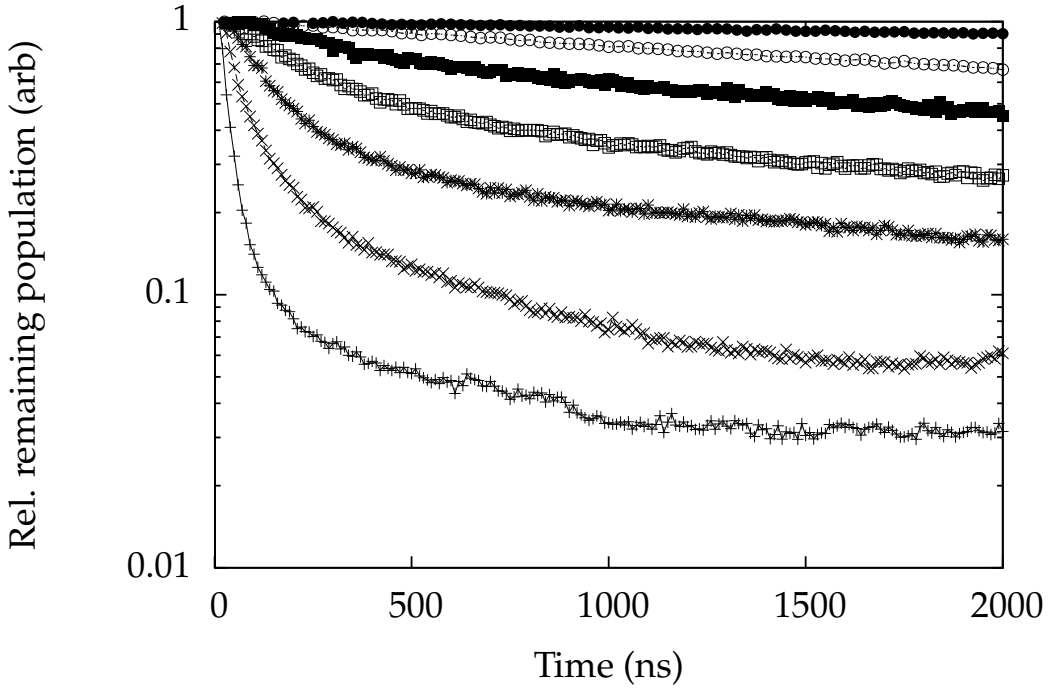

Figure 3.7: Fraction of atoms remaining one 17.045 GHz microwave photon from the ionization limit as a function of microwave pulsewidth. The ionization pulse occurs 2500 ns after laser excitation. Data shown are for 0.13 V/cm (△), 0.25 V/cm (●), 0.47 V/cm (○), 0.83 V/cm (■), 1.48 V/cm (□), 2.64 V/cm (∗), 8.34 V/cm (×), and 26.37 V/cm (+).

3.2.3 Single Photon Ionization Rates

The single photon ionization rates can be measured with a few small changes to the experimental setup. The field ionization pulse is adjusted to occur 3 μs after laser excitation, and the np laser excitation frequency is fixed to excite atoms one microwave photon from the ionization limit, in n states centered at $n = 430$. The microwave pulse length is controlled by the pulse/delay generator and iterated by the computer using GPIB from 0 μs to 2μs in 25 ns steps . This allows us to measure a decay curve for a given microwave field amplitude, and results are shown in Fig. 3.7. For E $>$ 3 V/cm there is an evident multi-exponential decay at the beginning of the pulse, which is certainly consistent with redistribution from easily photoionized states to those less easily ionized. At a low microwave field, E $<$ 1 V/cm,

an approximately exponential decrease in the number of atoms is observed, but the rate differs from the calculated photoionization rate by a factor of ten. The calculated ionization rate for E =0.47 V/cm is $5.2 \times 10^6\,\mathrm{s}^{-1}$, far above the observed rate of $4.6 \times 10^5\,\mathrm{s}^{-1}$. We can compare these rates to the expected perturbation theory rates, given by Fermi's Golden Rule, Eq. (1.15), using the bound-continuum matrix element is given by Delone *et al.*[31],

$$\langle n|r|\epsilon\rangle = \frac{0.4108}{n^{3/2}\omega^{5/3}}, \tag{3.1}$$

and the appropriate angular factor is given by,

$$\langle \ell m|\cos\theta|\ell+1 m\rangle = \sqrt{\frac{(\ell+1)^2-m^2}{(2\ell+3)(2\ell+1)}}. \tag{3.2}$$

A graphical comparison of the zero time ionization rates is shown in Fig. 3.8. The Kepler frequency for the $n = 430$ state is 83 MHz, and an ionization rate approaching this value is not perturbative. High ionization rates deplete the probability of finding the electron near the ion core, distorting the bound state wavefunction and Fermi's Golden Rule can no longer be applied. With microwave fields below 0.2 V/cm we observe an exponential decrease in the number of surviving atoms with a rate proportional to the microwave power, as expected from perturbation theory. However, the observed rates are lower than expected. For example at E = 0.13 V/cm we expect an ionization rate of $3.7 \times 10^5\,\mathrm{s}^{-1}$, but we observe $5.1 \times 10^4\,\mathrm{s}^{-1}$. Part of the rate discrepancy is due to Stark mixing of the levels. We are far above the $1/3n^5$ Inglis-Teller limit, and the stray field of 3 mV/cm converts the states to Stark states. At $n = 430$, the $3nE/2$ Stark frequency in this regime is 15 MHz. However, Stark mixing alone clearly does not account for the order of magnitude discrepancy in ionization rates. Numerically calculated ionization

rates using the Numerov method to generate bound and continuum wave functions are shown in Fig. 3.9 from $n = 10$ to $n = 90$. Similar calculations have been performed for $n = 430$, although numerical errors distort the high-ℓ states. The ℓ-averaged ionization rates are only $\sim$40% smaller than the np ionization rates.

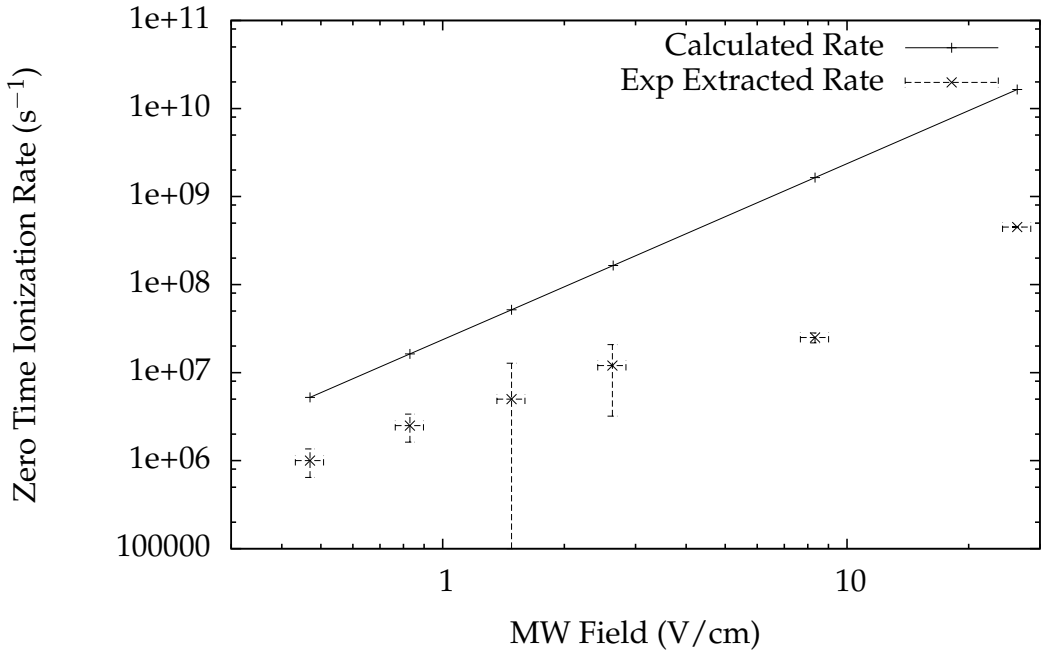

Figure 3.8: Short time single photon ionization rate as a function of microwave field. The calculated rate is given by a simple Fermi's Golden Rule calculation, Eq. (1.15) assuming $n = 430$.

For fields $> 0.2\,\mathrm{V/cm}$ non-exponential decays are observed, and a few percent of the atoms are not ionized even in the strongest fields we can apply. In fact the clearly non-exponential ionization rates seen stem from the fact that we excite a large number of states with different decay rates with our relatively broadband 4.5 GHz laser linewidth. This will be illustrated using a Floquet - MQDT model coherently coupling together many bound levels in Chapter 5.

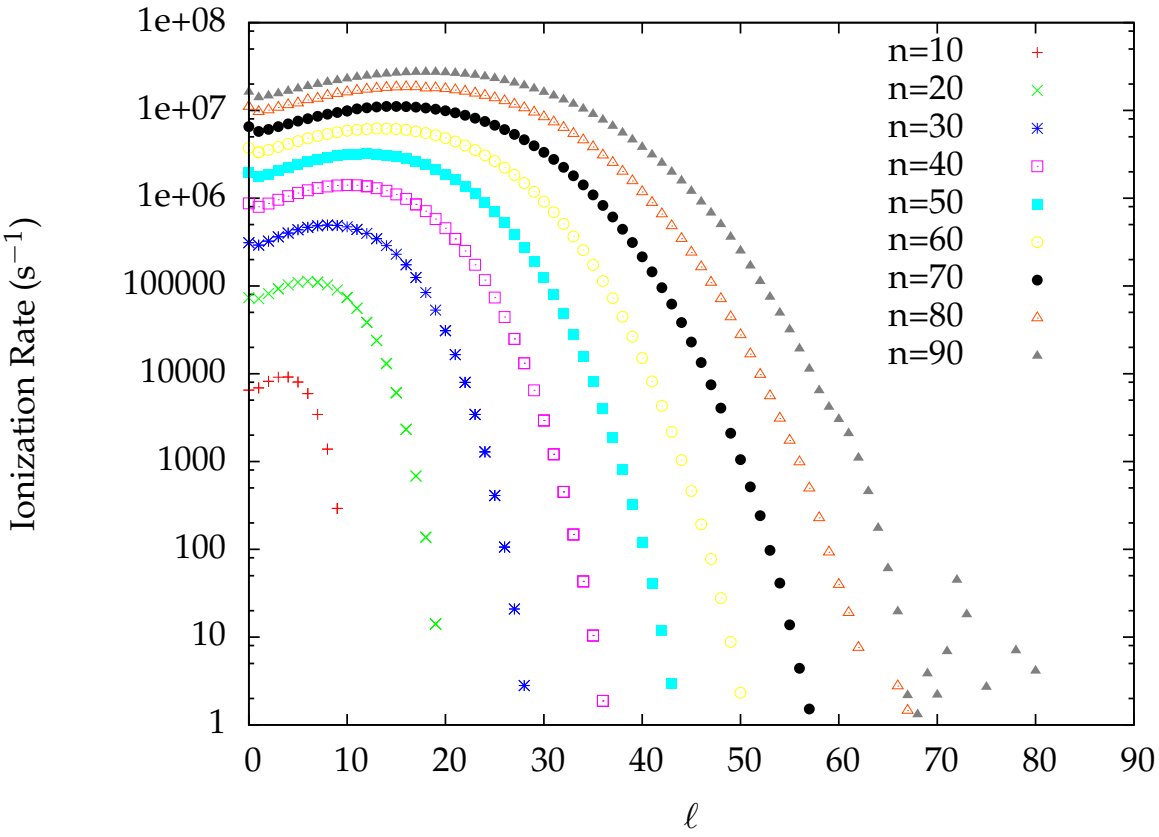

Figure 3.9: Numerically calculated ionization rates for a $m = 0$ n, ℓ state in a 3.5 V/cm microwave field. A congruent ionization rate as a function of ℓ is seen for $n = 430$ rates, although numerical errors distort the high-ℓ states.

3.2.4 Other experimental parameters

At this point it is worth discussing a few of the other experimental parameters that have been explored but are not relevant enough for an entire section.

Atomic Density

The density of Rydberg atoms can be coarsely adjusted by changing the lithium oven current or by attenuating the np excitation laser. Increasing the oven output or attenuating the excitation laser by 50% exhibits no noticeable changes in the microwave ionization spectra. This implies that there are negligible Rydberg-Rydberg interactions.

B-Field

Interesting results are also observed due to the 0.4 G magnetic field of the Earth. Delaying the microwave pulse after initial laser excitation to longer than the cyclotron half-period, $\pi m/Bq$, almost completely suppresses microwave ionization for n states above $n = 150$. For the Earth's magnetic field, measured to be $\sim$0.4 G at an angle of $\pi/4$ from the vertical as measured with a LakeShore 421 gaussmeter, the cyclotron half-period is 440 ns. Results for 200 ns, 7 V/cm, 22 GHz microwave pulses delayed 700 ns after laser excitation are shown as the dashed curve in Fig. 3.10, compared to the zero microwave field plotted as a solid curve.

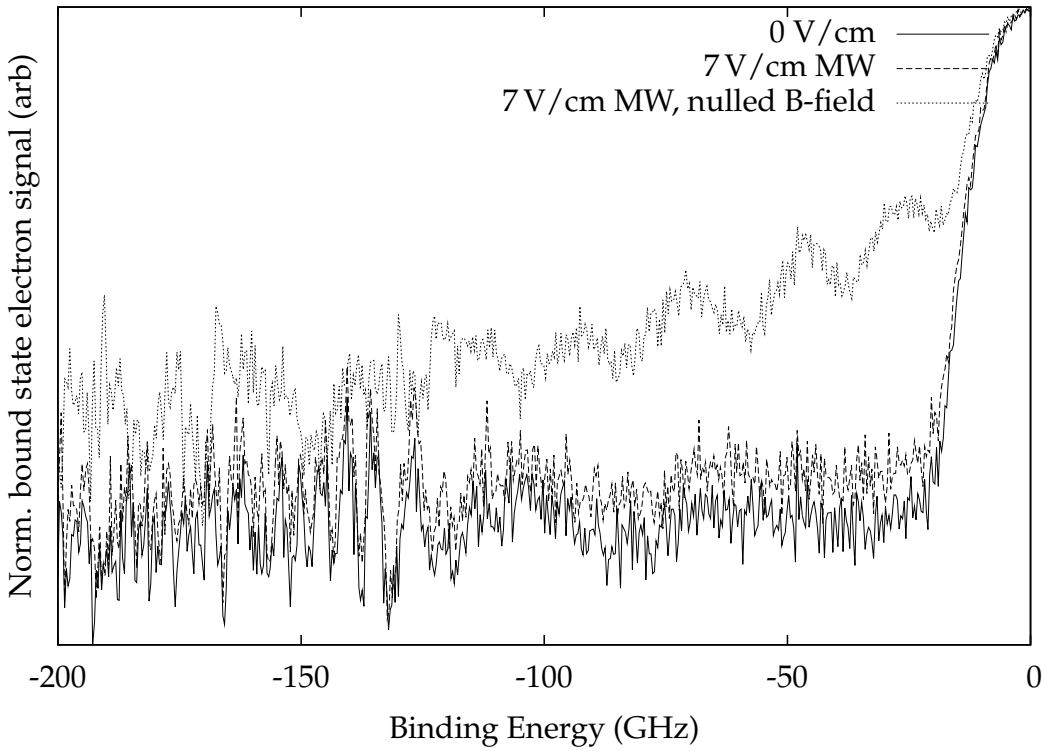

Figure 3.10: Normalized bound state electron signal as a function of binding energy for a 22 GHz microwave pulse 700 ns after laser excitation with and without the Earth's magnetic field.

Three pairs of Helmholtz coils were constructed and placed orthogonally around the experimental region. The magnetic field in the experimental region can be min-

imized to within 40 mG, as measured using a gaussmeter. Canceling the Earth's magnetic field allows microwave ionization to occur, as shown as the dotted curve in Fig. 3.10. The implication is that the 0.4 G magnetic field, along with the 5 mV/cm stray electric field, converts the initial np state to higher angular momentum states. Weak crossed electric and magnetic fields have been proposed by Delande and Gay as a scheme for producing circular Rydberg states[65]. Increasing the electric field above 10 mV/cm in the presence of a B-field when the delay between excitation and the microwave pulse is long also decreases microwave ionization. The implication is that ℓ-mixing decreases microwave ionization. This is unsurprising, as that high-ℓ states do not interact with the ion core and therefore are more difficult to ionize. This can be easily illustrated. The contribution to the bound-continuum matrix integral for the $\langle 430p0|r|0.01\,GHzd0\rangle$ as a function of atomic radius is shown in Fig. 3.11. The dominant contribution to the integral is within first two percent of the n^2 orbital radius. Subsequent microwave ionization experiments (and unless noted all of the data shown in this dissertation) have applied the microwave pulse within 100 ns of laser excitation to alleviate this problem.

3.2.5 Dressed state comparison

The coherent coupling of states extends beyond the bound states over the limit to the continuum states as well. This is easily illustrated by exciting the atoms in the presence of the microwave field. The relevant timing diagram is shown in Fig. 3.12. The results of scanning the laser over the ionization limit from 300 GHz below to 50 GHz above the limit are shown in Fig. 3.13. A fraction of atoms excited as high as three microwave photons above the limit are transferred from continuum to bound states by the microwave pulse and detected after 1 μs using the fast rising field ionization pulse.

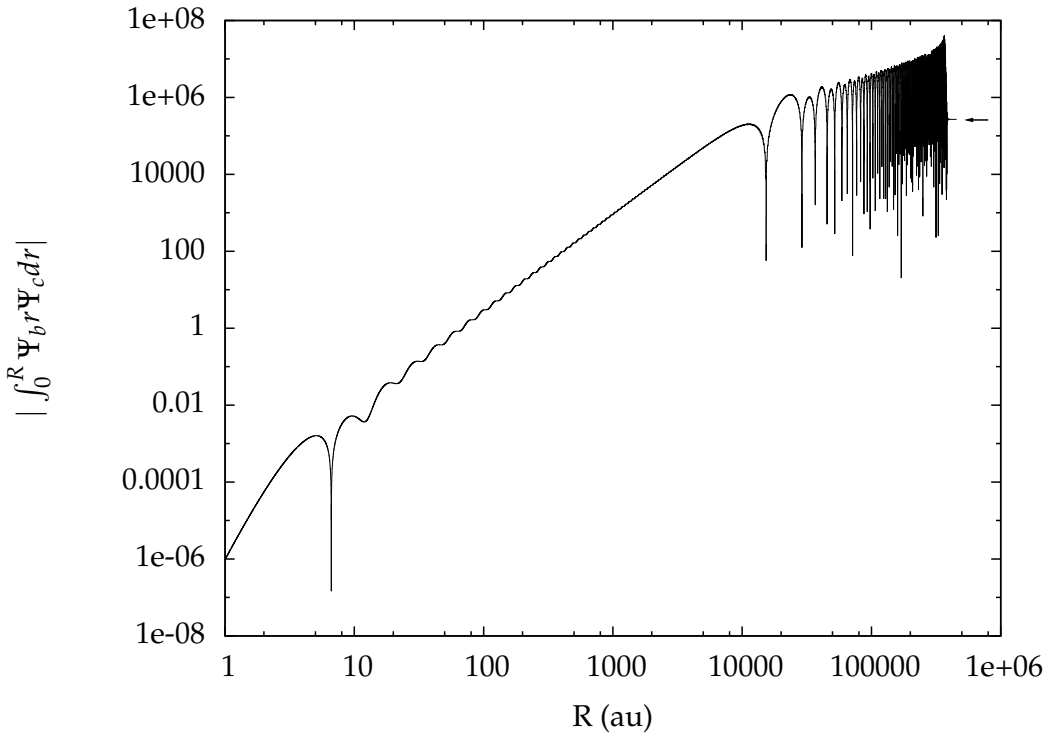

Figure 3.11: The contribution to the bound-continuum matrix integral for the $\langle 430p0|r|0.01\,GHz d0\rangle$ as a function of atomic radius. The small black arrow points to the final value.

The resonance structure previously observed below the limit continues smoothly over the ionization limit, clearly illustrating the strong coherent multi-state coupling both below and across the limit. This implies that the incoherent Anderson localization models in the scaled frequency regime from $\Omega = 2$ to $\Omega = n/2$ are not a proper description of microwave ionization, and a simple Fermi's Golden Rule approach fails above $\Omega = n/2$. A Floquet-MQDT model, detailed in Chapter 5, seems to properly model the results shown here.

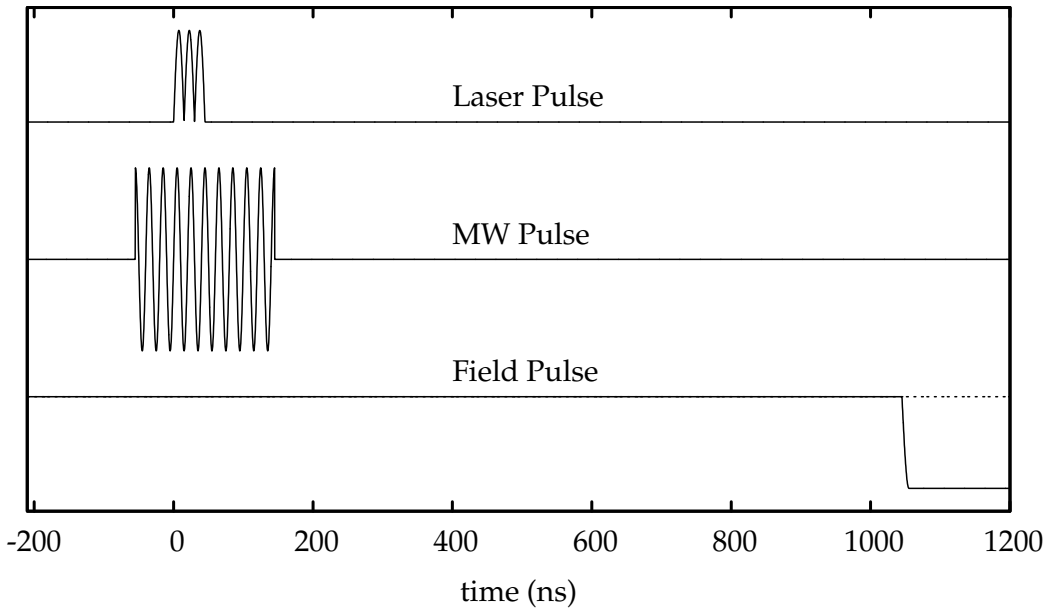

Figure 3.12: Timing diagram for dressed state excitation.

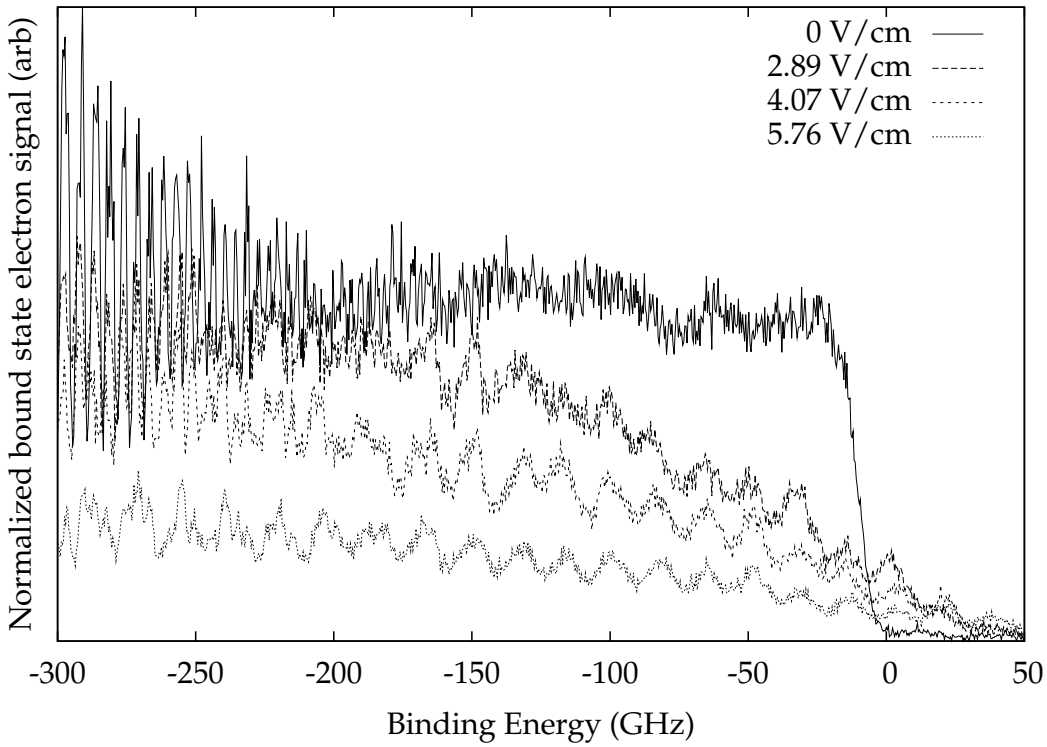

Figure 3.13: Normalized scans of the remaining atoms after 200 ns 17.07 GHz microwave pulses applied 100 ns before laser excitation, plotted vs binding energy.

Chapter 4

Multiphoton Microwave Ionization at 36 GHz

4.1 Introduction

This chapter discusses first experiments of multiphoton ionization approaching the photoionization limit using 36 GHz microwave pulses. The goals of the experiment in this chapter are two-fold. First, by increasing the microwave frequency with respect to the laser bandwidth, we can better resolve the shape of the multiphoton resonances seen. Second, we seek to better understand the above-threshold bound state resonances seen when laser excitation occurs in the presence of a microwave field.

The general experimental methods used in this chapter are discussed in Chapter 2 and specific details will be noted below. An appropriate experimental timing diagram is shown in Fig. 2.1. The experiment is based on a thermal Li beam laser excited to np states at the center of a Fabry-Perot cavity for the frequency range of 26 GHz to 40 GHz, illustrated in Fig. 2.12. The microwave cavity is constructed of two brass mirrors 40.6 mm in diameter with a 75.92 mm radii of curvature, spaced

by 54.2 mm. The cavity is operated on the TE_{010} mode at a frequency of 35.95 GHz with a $Q \approx 1600$. The Q/ω filling time of the cavity is therefore $\tau = 7$ ns.

Typically a 200 ns microwave pulse is injected into the cavity 100 ns after the laser excitation. One microsecond after the laser pulse a negative voltage pulse is applied to a plate below the microwave cavity to field ionize any remaining atoms and eject the resulting electrons through a hole in the plate above the cavity. The electrons are detected with a microchannel plate detector, and we record the signal with a gated integrator. Electrons produced by photoionization or microwave ionization leave the interaction region before the voltage pulse and are not detected.

4.2 Experimental Results

4.2.1 Microwave power

The recorded spectra for 200 ns, 35.95 GHz microwave pulses at field amplitudes from 1 V/cm to 70 V/cm taken in 1 dB power steps are plotted as a function of binding energy in Fig. 4.1. For clarity, the data are plotted in 3 dB power steps.

Interpolation between these data yields the 10% and 50% ionization thresholds, which are shown in Fig. 4.2 for a laser frequency tuned from -280 GHz to 0 GHz below the ionization limit. Each data point is averaged over 2000 laser shots and the microwave pulse is applied on alternating shots for data normalization. We again see that the requisite field for ionization is approximately the same whether the atoms are bound by one microwave photon or seven microwave photons. The theoretical prediction of Jensen *et al.*, Eq. (1.22), is approximately the average value of the experimentally measured 50% threshold field over the binding energy range measured. The theoretical 50% threshold prediction is 20.95 V/cm, plotted as a straight dotted line in Fig. 4.2. Also, we again see an oscillatory structure at the

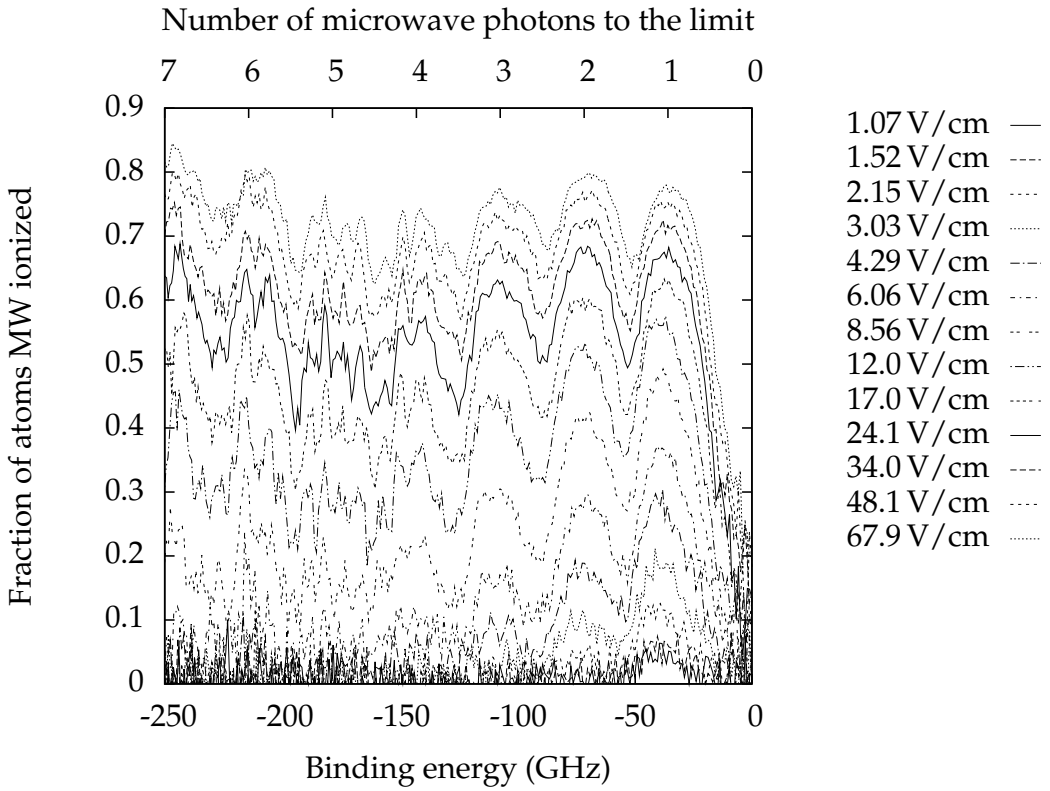

Figure 4.1: Fraction of atoms microwave ionized as a function of binding energy for a 200 ns, 35.95 GHz microwave pulse. Data was collected in 1 dB power steps from 1 V/cm to 70 V/cm, and plotted in 3 dB power steps for clarity.

microwave frequency in the number of atoms surviving the microwave pulse.

From these data we can also extract the fractional ionization as a function of microwave power. These data are plotted at binding energies one microwave photon ($n \sim 300$) and 1.5 microwave photons ($n \sim 247$) below the ionization limit in Fig. 4.3. These binding energies represent a trough (36 GHz) and peak (54 GHz) shown in Fig. 4.2, respectively. These data can be fit to functions of the microwave field amplitude E of the form $f(E) = a(1 - e^{-bE^2}) + c \cdot g(E)$, where a, b, and c are constants and $g(E)$ is a best fit parameter not adhering to perturbation theory. For one microwave photon from the limit, these constants are 0.3, 0.021, and 0.12, respectively, and $g(E)$ =ln(E). Although we cannot experimentally create 100% ionization microwave field amplitudes, these constants imply that the 100%

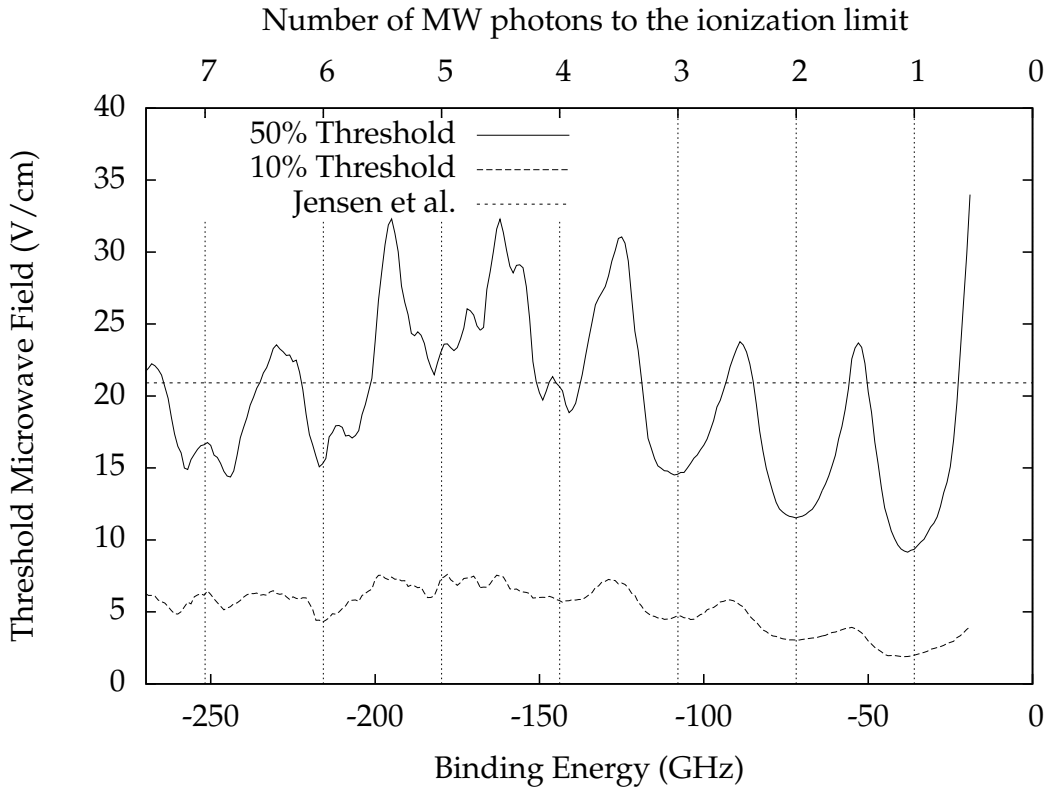

Figure 4.2: Interpolated thresholds for 10% and 50% microwave ionization as a function of binding energy for a 200 ns, 35.95 GHz microwave pulse. The straight dotted line is the prediction of Jensen *et al.*[21], Eq. (1.22).

ionization threshold is more than forty times the 50% ionization threshold observed.For comparison, the single photon perturbation theory curve is given by $f(E) = 1 - e^{-bE^2}$, where $b = 1.15$. This curve, as well as the perturbation theory prediction for $n = 247$, are shown as dot-dashed lines in Fig. 4.3.

4.2.2 Bias Voltage

We can quantify the effects of stray field on the microwave ionization rates, as previous discussed for 17 GHz microwave ionization in section 3.2.2. With the laser frequency fixed at a frequency below the ionization limit a bias voltage is applied to the plate above the microwave cavity. A set of bias fields for a laser tuning one microwave photon and 1.5 microwave photons below the limit is shown in Fig. 4.4.

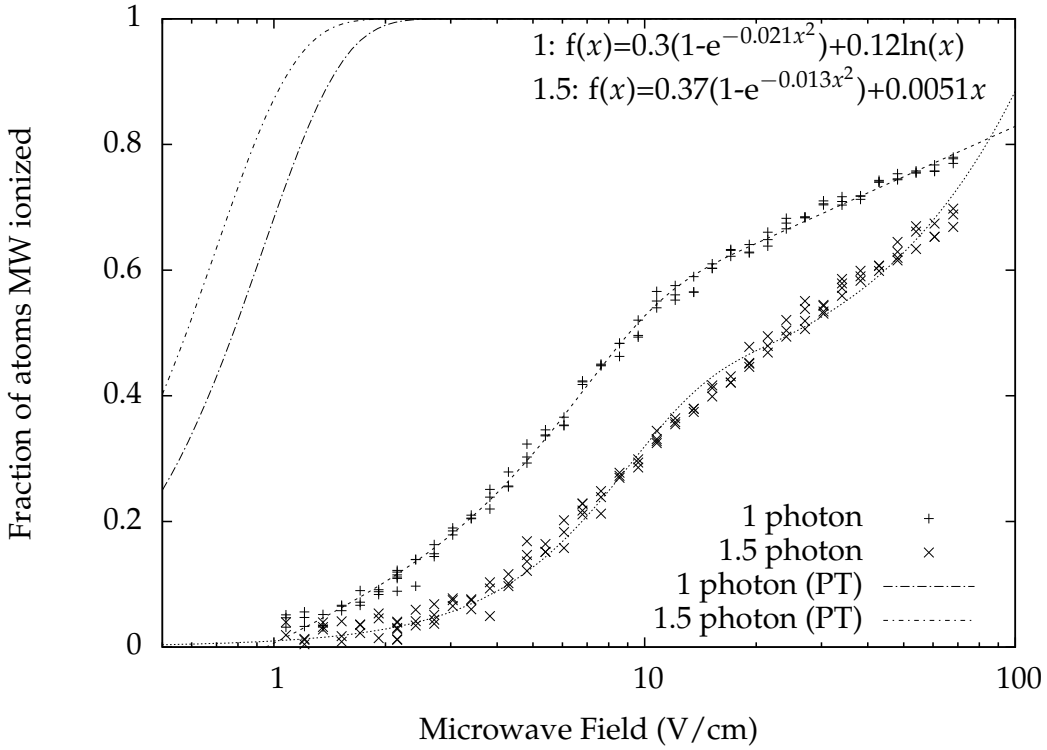

Figure 4.3: Fractional ionization as a function of microwave field amplitude one microwave photon and 1.5 microwave photons from the ionization limit, for a 200 ns, 35.95 GHz microwave pulse. These data sets correspond to $n \sim 300$ and $n \sim 247$, respectively. The fitted curves are of the form $f(x) = a(1 - e^{-bx^2}) + c \cdot g(x)$, where $g(x)$ is a nonperturbation theory best fit function, $\ln(x)$ for one photon and x for 1.5 photons. The perturbation theory predicted results are plotted as dot-dashed lines of the form $f(x) = 1 - e^{-bx^2}$, where b is 1.15 and 2.06 for one and 1.5 photons, respectively.

Stray fields on the order of 20 mV/cm can increase the observed fractional ionization by a factor of two or more, and the fractional ionization as a function of applied field exhibits a gaussian profile with a full width at half maximum (FWHM) on the order of 10 mV/cm. Iterating this process of minimizing the fractional ionization for all field plates in the chamber lets us reduce the stray field to 5 mV/cm in the interaction region, as seen by the $1/9n^4$ depression of the ionization limit. Interestingly, the fields required to greatly increase microwave ionization are much smaller than previously observed at lower n by Pillet *et al.*[26]. The required static

field predicted by Eq. (1.18) is a factor of five larger than the FWHM seen in Fig. 4.4. At this microwave frequency, however, above $n = 71$ the Inglis-Teller limit is below the requisite static field predicted by Eq. (1.18), and whether the simple model of Pillet *et al.* still holds is questionable at best. At $n = 300$, even the 5 mV/cm residual stray field is above the 0.7 mV/cm Inglis-Teller field and the excited atoms are already Stark mixed.

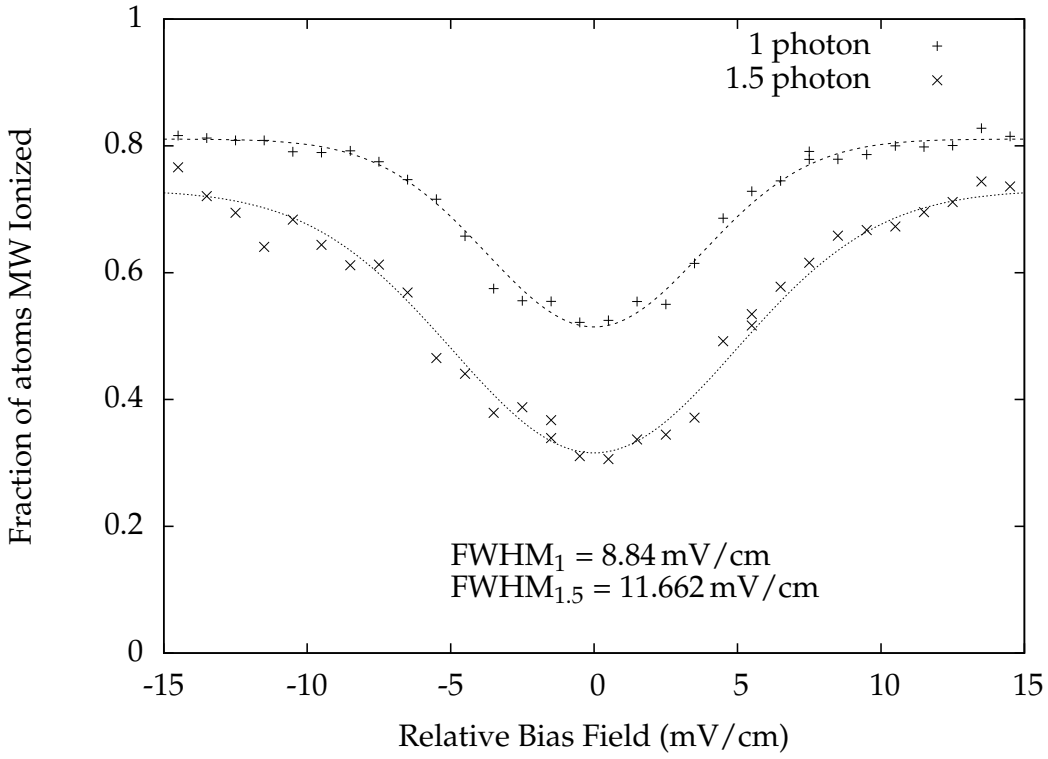

Figure 4.4: Microwave ionization population fraction as a function of external bias field, for binding energies 1 and 1.5 microwave photons below the ionization limit after a 200 ns, 12.6 V/cm, 35.95 GHz microwave pulse. These data sets correspond to $n \sim 300$ and $n \sim 247$, respectively. The fitted curves are fitted gaussians, with FWHM of 8.84 mV/cm and 11.662 mV/cm, respectively.

4.2.3 Dressed state Excitation

We can experimentally observe excitation of the atom dressed by the microwave field by shifting the microwave pulse so that laser excitation occurs at the center

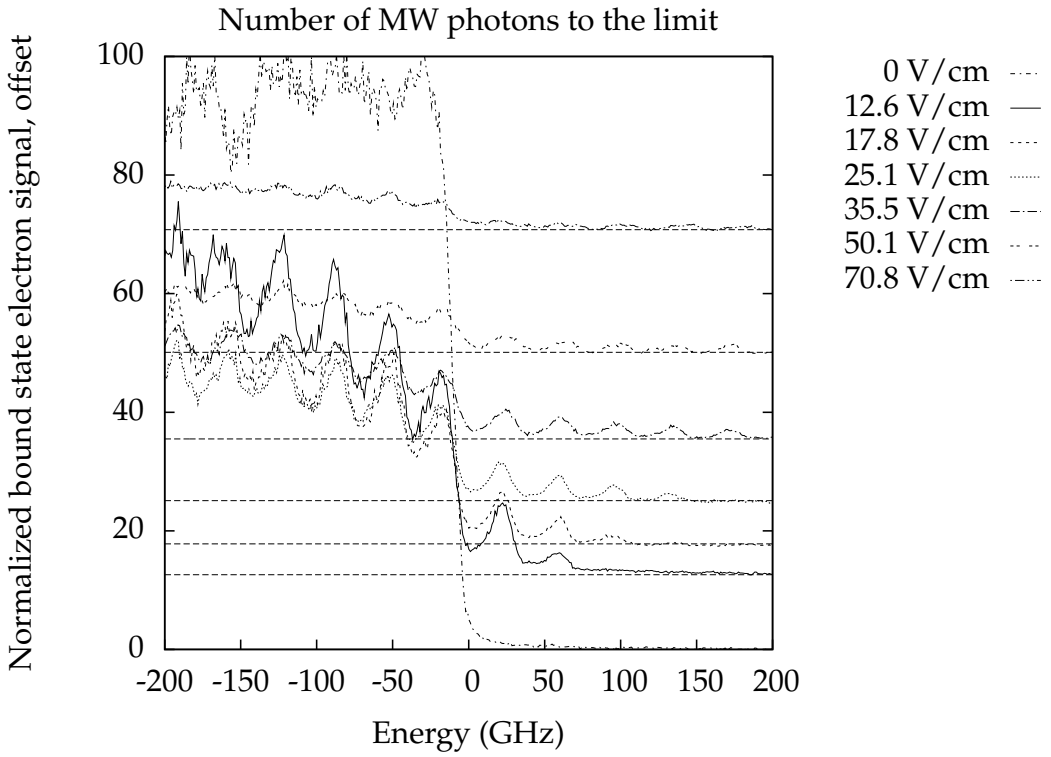

Figure 4.5: Bound state electron normalized signal percentage for a set of microwave field amplitudes as a function of binding energy from 200 GHz below the ionization limit to 200 GHz above the ionization limit for laser excitation centered about a 200 ns, 35.95 GHz microwave pulse. Data are plotted vertically offset by the microwave field amplitude applied.

of the 200 ns microwave pulse. The relevant timing diagram is shown in Fig. 3.12. The results for energies between -200 GHz and 200 GHz of the ionization limit are shown in Fig. 4.5 for a set of microwave field amplitudes, plotted as the normalized bound state electron signal percentage offset by the applied microwave field amplitude. The results for binding energies below the ionization limit are shown in Fig. 4.6 and exhibit an oscillatory structure at the microwave frequency similar to Fig. 4.2 and Fig. 3.13. Over the ionization limit there is clear evidence of the microwave field driving above-threshold atoms down to bound states, as shown in Fig. 4.7. This is similar to the recombination results of Shuman *et al.*[66] and Klimenko[67]. We clearly observe continuum electrons as high as ten photons

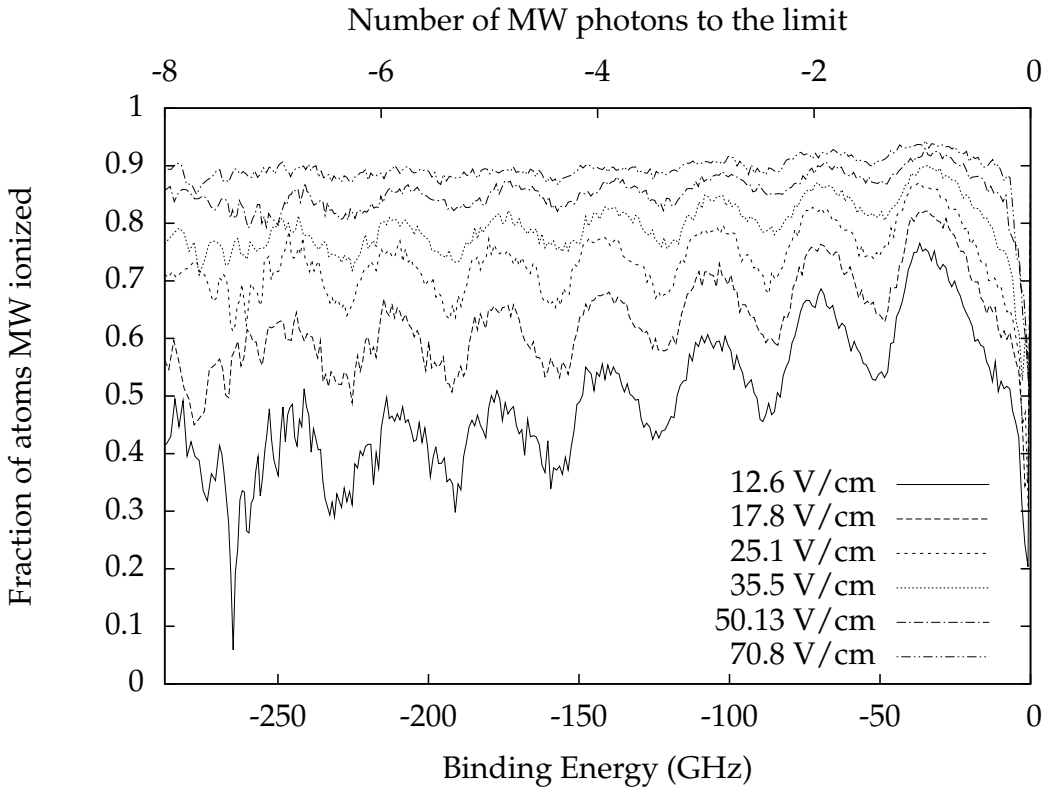

Figure 4.6: Dressed state excitation below the limit for a set of microwave field amplitudes as a function of binding energy below the ionization limit for laser excitation centered about a 200 ns, 35.95 GHz microwave pulse.

above the ionization limit driven back down to bound states.

Simpleman's Model

Previous above threshold ionization experiments have had impressive success explaining results using a simple classical model, known as the Simpleman's Model[68], which will be illustrated below. A free electron created in the field, $E \sin \omega t$, at time t_0, has initial velocity v_0 and corresponding kinetic energy $v_0^2/2$. Integrating the 1-

D equation of motion yields the velocity and position of the electron at time t,

$$v(t) = v_0 + \frac{E}{\omega}(\cos\omega t - \cos\omega t_0) \tag{4.1}$$

$$x(t) = x_0 + v_0(t - t_0) - \frac{E}{\omega}\cos\omega t_0(t - t_0) + \frac{E}{\omega^2}(\sin\omega t - \sin\omega t_0), \tag{4.2}$$

where v_0 and x_0 are the velocity and position of the electron at time t_0, the time when the free electron is created in the field. From this we can calculate the kinetic energy, $K(t)$,

$$K(t) = K_0 + \frac{E^2}{2\omega^2}\left(\cos\omega t - \cos\omega t_0\right)^2 + \frac{Ev_0}{\omega}\left(\cos\omega t - \cos\omega t_0\right), \tag{4.3}$$

where K_0 is the initial kinetic energy.

We can express the cycle averaged kinetic energy in terms of the pondermotive potential, Eq. (1.14),

$$\langle K\rangle = K_0 + 2\Phi_{pond}(\frac{1}{2} + \cos^2\omega t_0) - 2v_0\sqrt{\Phi_{pond}}\cos\omega t_0. \tag{4.4}$$

If the electron is initially at rest, the average kinetic energy is between Φ_{pond} and $3\Phi_{pond}$.

At this point it is worth briefly discussing the ponderomotive force in slightly more detail. A charge e and mass m in an inhomogeneous electric field $E(x,t) = E(x)\cos\omega t$, such as an ionized electron in a microwave cavity, feels a force,

$$F = eE(x)\cos\omega t = m\ddot{x}, \tag{4.5}$$

where the charge trajectory can be thought of as the sum of a large slow drift, x_0 and small fast oscillation, x_1. Taylor expanding Eq. (4.5) about x_0 and solving for

the time averaged drift force gives,

$$F_{pond} = \frac{-e^2}{4m\omega^2}\nabla E^2. \tag{4.6}$$

Equation (4.6) implies charges are pushed towards regions of weak field. The associated ponderomotive energy, Eq. (1.14), can be quite large in the case of strong field laser pulses and the ponderomotive shift brings the ionization limit to higher energies, requiring more photons for ionization[69].

The pondermotive shift for the largest fields used in Fig. 4.7 is only 10 GHz, and although noticeable in the experimental data as the dashed line in Fig. 4.7, is too small to explain our results.

The results, however, can be explained by modifying the Simpleman's Model. Shuman *et al.* account for the atomic $-1/r$ potential neglected in the Simpleman's Model[66]. The work done on an electron by the field E is,

$$W = -\int_0^{t_f} E(t)\cdot v(t)dt, \tag{4.7}$$

The electron's kinetic energy is approximated as $-1/r$ near the core. This gives a velocity $v(t) = \sqrt{2/r} = (4/3t)^{1/3}$. The work integral, Eq. (4.7), can be evaluated by approximating the sinusoidal term by a sum of equal and opposite amplitude parabolas and truncating the integral at $t_f = t_0 + T/2$, where $T = 2\pi/\omega$. The electron's time-averaged velocity rapidly decreases with increasing r, and net energy transfer after one half-cycle is therefore minimal. The maximum energy transfer,

$$\Delta W \approx \frac{3}{2}E\omega^{-2/3}, \tag{4.8}$$

is seen when $t_0 = T/6$. The maximum energy transfer predicted by Eq. (4.8) is

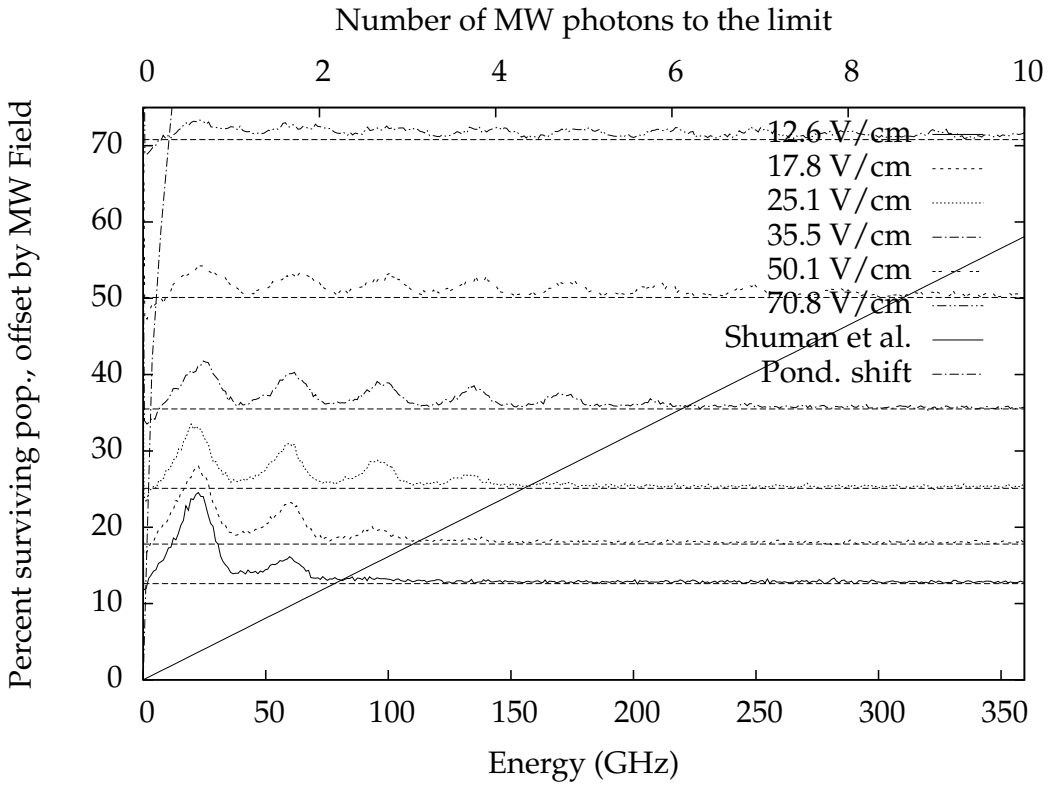

Figure 4.7: Dressed state excitation above the limit for a set of microwave field amplitudes as a function of energy above the ionization limit for laser excitation centered about a 200 ns, 35.95 GHz microwave pulse. The data are plotted as the percent population transferred to bound states, offset by the microwave field amplitude. The simple energy transfer formula of Shuman et al., Equation (4.8), is plotted as the solid diagonal line and the pondermotive shift is plotted as the diagonal dashed line[66].

plotted as the solid diagonal line in Fig. 4.7 and well matches our experimental results. This model also well describes the above-threshold dielectronic recombination results of Shuman *et al.* at 38 GHz[66] and Klimenko at 4 GHz, 8 GHz, and 12 GHz[67]. A few other interesting results can be extracted from Fig. 4.7. The resonances corresponding to integer multiples of the microwave frequency are relative not to the absolute ionization limit, but to the effective ionization limit caused by remaining stray field. Similar to the results of Shuman, we also see a frequency shift of the resonances due to the pondermotive shift[70].

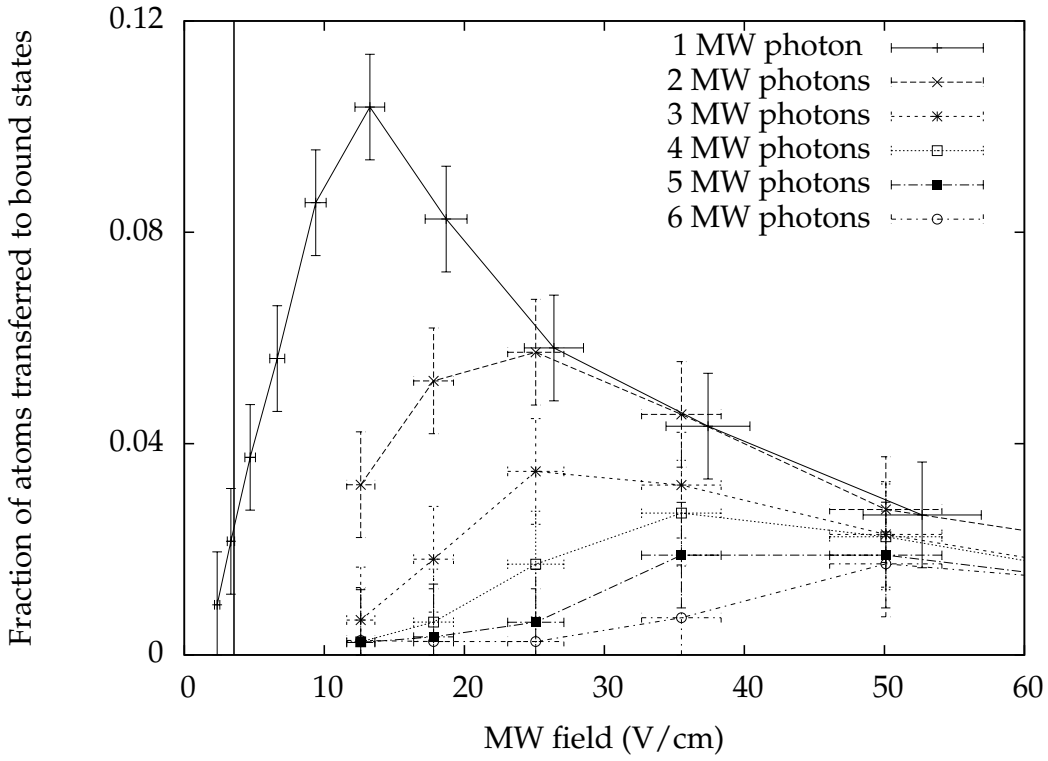

Figure 4.8: Dressed state excitation i microwave photons above the limit, plotted as the fraction of atoms transferred to bound states as a function of microwave field amplitude, for laser excitation centered about a 200 ns, 35.95 GHz microwave pulse.

Figure 4.7 implies that the population transfer from one photon above the ionization limit to bound states decreases as the microwave field is increased. This can be easily quantified by tuning the laser frequency to one microwave photon above the limit and measuring the fractional population transfer as a function of microwave field. The results are shown in Fig. 4.8 with straight lines drawn between data points to better separate data sets. The prediction of Eq. (4.8) is shown as a vertical solid line. Unsurprisingly, only a small fraction of the above threshold population is transferred to bound states when the microwave field is below the prediction of Eq. (4.8). Peak population transfer from one microwave photon above the ionization limit to bound states occurs in a microwave field of 13.2 V/cm.

From Fig. 4.7 we can further extract what microwave field must be used to

maximize transfer i microwave photons above the limit, as shown by traces 2-6 in Fig. 4.8. The optimal field required to transfer above threshold population from between one and six microwave photons from the limit to bound states is shown in Fig. 4.9.

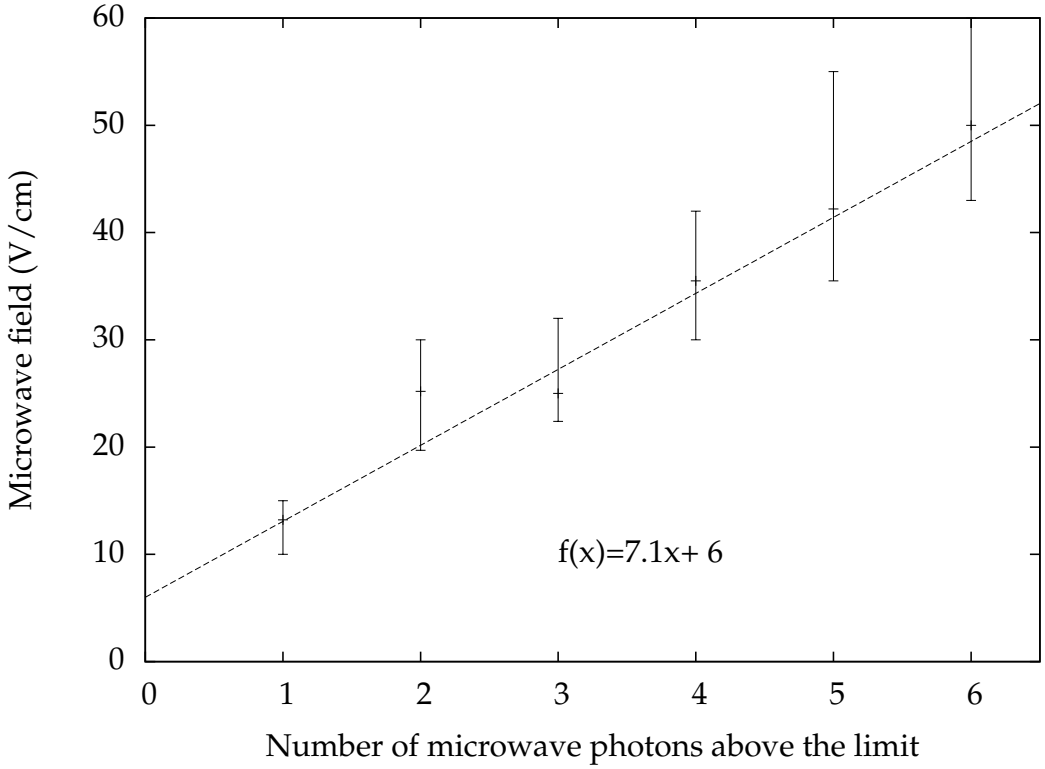

Figure 4.9: Optimal microwave field amplitude required to transfer above threshold population to bound states, as a function of the number of microwave photons above the limit, for laser excitation centered about a 200 ns, 35.95 GHz microwave pulse.

Clearly the requisite field for maximal population transfer to bound states from i microwave photons above the ionization limit must be higher than the minimum field required to transfer population to bound states, governed by Eq. (4.8). We can assume the peak field exhibits a linear energy dependence, like Eq. (4.8), and empirically fit a function $f(i)$ to find the optimal microwave field i microwave photons above the limit as $f(i) = a * i + b$. The coefficients a and b are most likely functions of the microwave frequency, however for now we can only say

that $a = 7.1\,\mathrm{V/cm/photon}$ and $b = 6\,\mathrm{V/cm/photon}$ for ω =35.95 GHz, yielding the optimal field in V/cm.

Much like below the ionization limit, these results are highly sensitive to stray electric fields. We can easily systematically quantify the effects of an applied external field. A DC voltage was applied to the field plate above the microwave cavity. The applied voltage was rastered as the excitation laser energy was iterated, averaged for 1000 laser shots per point, with the microwave pulse applied every other laser shot for normalization. The fractional population transferred to bound states when laser excitation occurs at the center of a 200 ns, 13.2 V/cm, 36 GHz microwave pulse is shown in Fig. 4.10.

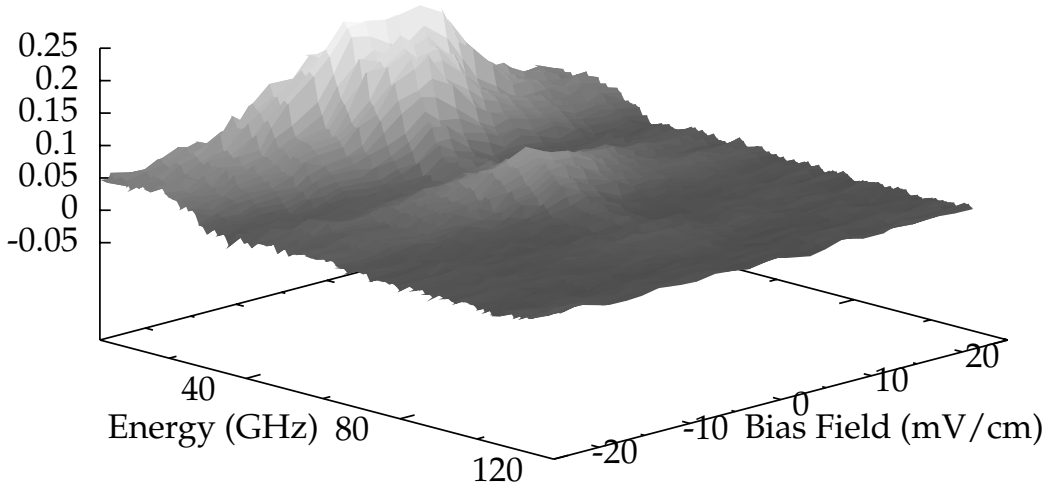

Figure 4.10: Fraction of population above the ionization limit transferred to bound states after laser excitation at the center of a 13.2 V/cm 200 ns microwave pulse at 35.95 GHz as a function of laser energy and bias field applied to the upper field plate.

Applying an external field universally suppresses above-threshold electrons from transferring to bound states. This is best seen by extracting cross-sections from Fig. 4.10 at the one and two microwave photon resonance peaks, as shown in Fig. 4.11. These peaks are both fit to gaussians of widths comparable to those seen below the ionization limit, e.g. Fig. 4.4. That external fields suppress net re-

combination is not surprising since external fields increase ionization below the limit. Recombined bound electrons can be easily ionized by successive cycles of the microwave field.

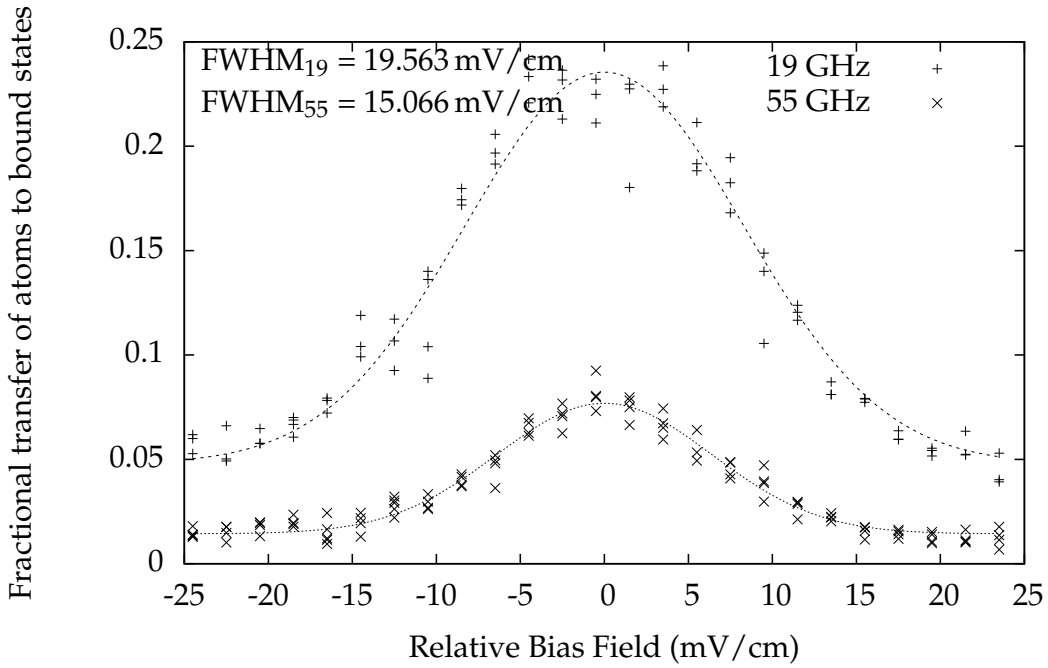

Figure 4.11: Fraction of population one and two photons above the ionization limit transferred to bound states after laser excitation at the center of a 13.2 V/cm 200 ns microwave pulse at 35.95 GHz as a function of bias field applied to the upper field plate.

Chapter 5

A Floquet-MQDT Model of Multiphoton Microwave Ionization

Explaining multiphoton microwave ionization spectra has been possible with a Floquet-Multichannel Quantum Defect Theory (MQDT) model, a coherent coupling of Rydberg levels both above and below the ionization limit. Recent theoretical work on multiphoton microwave ionization by Schelle *et al.* has looked to Anderson localization as an explanation of experimental results[29]. However, an Anderson localization model breaks down for one and few photon ionization, predicting higher ionization rates than experimentally seen. Instead, a combined Floquet - MQDT approach successfully models the observed system dynamics, where the observed spectra are determined by the final bound-continuum coupling. In the sections that follow, Floquet Theory and MQDT will be introduced and the results of the simulations will be explained.

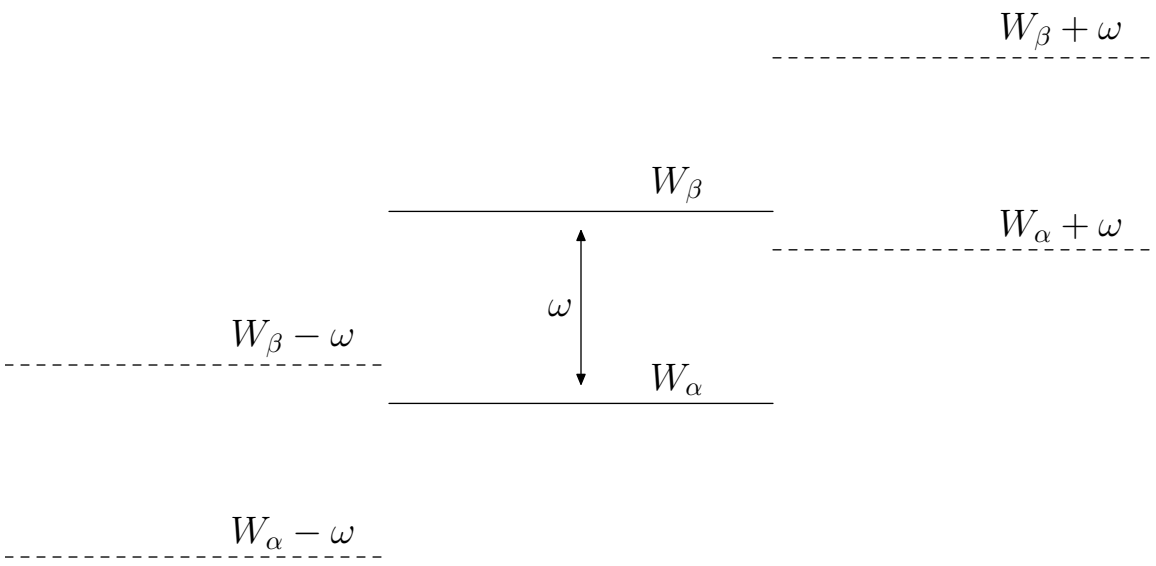

Figure 5.1: Two level Floquet energy diagram.

5.1 Floquet Theory

Floquet theory provides a straightforward method for treating periodic perturbations, positing that periodic perturbations give rise to periodic solutions[35].

We can begin by treating a simple system with a periodic perturbation. The canonical example of Floquet theory is a simple quantum system of two discrete states, α and β, in an oscillating field, illustrated in Fig. 5.1. We can assume state α has energy W_α, and state β has energy W_β. We can write the periodic perturbation as $2b\cos\omega t$. The time dependent wave function for this system is

$$\Psi(r,t) = a_\alpha(t)\Psi_\alpha(r) + a_\beta(t)\Psi_\beta(r). \tag{5.1}$$

From this we can construct the time dependent Schrödinger equation in matrix form,

$$i\frac{d}{dt}\begin{pmatrix} a_\alpha(t) \\ a_\beta(t) \end{pmatrix} = \begin{pmatrix} E_\alpha & 2b\cos\omega t \\ 2b\cos\omega t & E_\beta \end{pmatrix}\begin{pmatrix} a_\alpha(t) \\ a_\beta(t) \end{pmatrix}. \tag{5.2}$$

The essence of the Floquet approach is to replace $a_\alpha(t)$ and $a_\beta(t)$ with the Fourier sums, $\sum_n a_{i\alpha}^n e^{in\omega t}$ and $\sum_n a_{i\beta}^n e^{in\omega t}$, as well as the $e^{-iq_i t}$ time dependent factor for any eigenvalue q_i. Explicitly, $a_\alpha(t)$ and $a_\beta(t)$ are

$$a_\alpha(t) = \sum_n a_{i\alpha}^n e^{in\omega t} e^{-iq_i t} \tag{5.3}$$

$$a_\beta(t) = \sum_n a_{i\beta}^n e^{in\omega t} e^{-iq_i t}. \tag{5.4}$$

These infinite set of $a_{i\{\alpha,\beta\}}^n$ coefficients are time independent and allow us to find a new set of time independent eigenvalues and eigenfunctions for our system.This replacement ensures that the solutions are periodic with period $2\pi/\omega$.

We can explicitly plug these Fourier sums into Eq. (5.2),

$$i\frac{d}{dt}\begin{pmatrix} \sum_n a_{i\alpha}^n e^{in\omega t} e^{-iq_i t} \\ \sum_n a_{i\beta}^n e^{in\omega t} e^{-iq_i t} \end{pmatrix} = \begin{pmatrix} W_\alpha & 2b\cos\omega t \\ 2b\cos\omega t & W_\beta \end{pmatrix} \begin{pmatrix} \sum_n a_{i\alpha}^n e^{in\omega t} e^{-iq_i t} \\ \sum_n a_{i\beta}^n e^{in\omega t} e^{-iq_i t} \end{pmatrix} \tag{5.5}$$

Taking the derivative on the left hand side, as well as simplifying yields,

$$\begin{aligned} (q_i - n\omega)\sum_n a_{i\alpha}^n e^{in\omega t} &= W_\alpha \sum_n a_{i\alpha}^n e^{in\omega t} + b\sum_n a_{i\beta}^n e^{i(n+1)\omega t} + b\sum_n a_{i\beta}^n e^{i(n-1)\omega t} \\ (q_i - n\omega)\sum_n a_{i\beta}^n e^{in\omega t} &= W_\beta \sum_n a_{i\beta}^n e^{in\omega t} + b\sum_n a_{i\alpha}^n e^{i(n+1)\omega t} + b\sum_n a_{i\alpha}^n e^{i(n-1)\omega t} \end{aligned} \tag{5.6}$$

This yields a set of homogeneous equations for a given n,

$$\begin{aligned} (W_\alpha + n\omega - q_i)a_{i\alpha}^n + ba_{i\beta}^{n+1} + ba_{i\beta}^{n-1} = 0 \\ (W_\beta + n\omega - q_i)a_{i\beta}^n + ba_{i\alpha}^{n+1} + ba_{i\alpha}^{n-1} = 0 \end{aligned} \tag{5.7}$$

We can then write out these set of equations in matrix form,

$$\begin{pmatrix} \ddots & & & & & & \\ & W_\beta - \omega & b & 0 & 0 & 0 & \\ & b & W_\alpha & 0 & 0 & b & \\ & 0 & 0 & W_\beta & b & 0 & \\ & 0 & 0 & b & W_\alpha + \omega & 0 & \\ & 0 & b & 0 & 0 & W_\beta + \omega & \\ & & & & & & \ddots \end{pmatrix} \begin{pmatrix} \vdots \\ a_{i\beta}^{-1} \\ a_{i\alpha}^{0} \\ a_{i\beta}^{0} \\ a_{i\alpha}^{1} \\ a_{i\beta}^{1} \\ \vdots \end{pmatrix} = q_i \begin{pmatrix} \vdots \\ a_{i\beta}^{-1} \\ a_{i\alpha}^{0} \\ a_{i\beta}^{0} \\ a_{i\alpha}^{1} \\ a_{i\beta}^{1} \\ \vdots \end{pmatrix} \tag{5.8}$$

Written in this fashion, it is clear that this vector composed of $a^n_{i\{\alpha,\beta\}}$ is simply the eigenvector of Floquet energy q_i and the above Floquet Hamiltonian, denoted H_F.

In the matrix of Eq (5.8) the off-diagonal matrix elements couple the nearly resonant W_β and $W_\alpha + \omega$ components and the far off-resonant W_α and $W_\beta + \omega$ components. The far off-resonant coupling is usually ignored, and this approximation is termed the rotating wave approximation. With the rotating wave approximation it is evident that the matrix of Eq. (5.8) breaks into two by two blocks which are identical other than overall shifts in energy by multiples of ω. The rotating wave approximation is widely used for single photon transitions, but is not necessarily valid for multiphoton transitions.

5.1.1 N-Level Systems

Expanding Floquet theory to a larger N-level atomic system is essentially trivial, although the resultant energy spectra are often unwieldy. In practice, infinite matrices are not used for numerical calculations. The Floquet matrix only has to be large enough that the Floquet energies do not significantly change by extending the

matrix. By the rotating wave approximation the non-resonant off-diagonal matrix elements coupling $W_\beta \rightarrow W_\alpha - \omega$ can be ignored, letting us break the Hamiltonian matrix into separable blocks. A Floquet approach has been successfully ap-

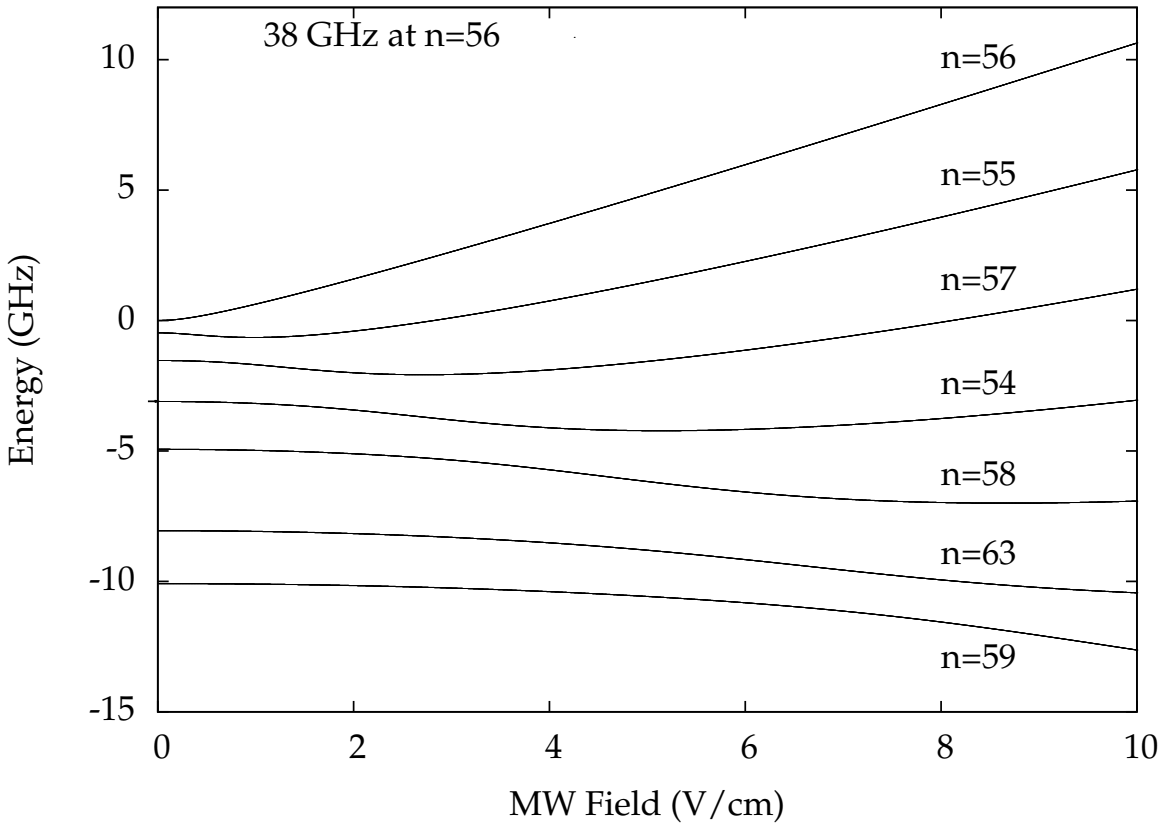

Figure 5.2: Floquet energy spectrum for a 1D n=56 Rydberg atom in a 38 GHz microwave field.

plied to nondispersing wave packets, which are composed of states coupled by a microwave field where the microwave frequency equals the n spacing. The near resonant photon $\Delta n = 1$ couplings are by far the most important, and the rotating wave approximation can be employed. In this case the Floquet matrix for a 1D

atom has the form,

$$H = \begin{pmatrix} \ddots & & & & & & & & \\ & W_{n'''}+3\omega & b'' & & & & & & \\ & b'' & W_{n''}+2\omega & b' & & & & & \\ & & b' & W_{n'}+\omega & b & & & & \\ & & & b & W_n & b^+ & & & \\ & & & & b^+ & W_{n^+}-\omega & b^{++} & & \\ & & & & & b^{++} & W_{n^{++}}-2\omega & & \\ & & & & & & & \ddots & \end{pmatrix}, \tag{5.9}$$

where the off-diagonal couplings are given by $b = \frac{1}{2}(0.3n^2E)$[71]. Diagonalizing the matrix yields the Floquet energies shown in Fig. 5.2 for $n = 56$ and a 38 GHz microwave field. In states with positive Stark shifts the electron's dipole oscillates out of phase with the microwave field, and in states with negative Stark shifts the dipole oscillates in phase with the microwave field[72].

Localization models applied to high scaled frequency microwave ionization suggest the the dominant couplings are the single photon $n - n'$ transitions, where n and n' are separated by approximately one microwave photon and $|n - n'| \gg 1$. In this case one could reasonably expect to use the rotating wave approximation, again reducing the Floquet Hamiltonian matrix to a single block in tridiagonal form, as shown in Eq. (5.9). However, there are two difficulties in this procedure. First, selecting the appropriate near resonant states while keeping the matrix size reasonable is difficult. When the state spacing is small compared to the photon energy, selecting the appropriate near resonant state or states is no longer obvious. Second, the above picture does not have a clear prescription for modeling photoionization to the continuum. Thankfully, both of these problems are solved by

adopting a quantum-defect theory approach, which will be discussed below.

5.2 Multichannel Quantum-Defect Theory

Multichannel quantum-defect theory (MQDT) has been quite successful in predicting atomic spectra of multi-electron atoms[73, 74]. Originally developed by Fano[75, 76] and Seaton[77, 78], much of treatment of MQDT illustrated here is taken from Cooke and Cromer[79].

The basic principle of MQDT is that the atomic valence electron spends most of its time far from the ionic core in a coulomb potential. However, when the electron come close to the core there is a probability of scattering into other states due to a short range interaction. In spite of the fact that the interaction of the Rydberg electron with the microwave field does not sound like a short range interaction, energy exchange can only occur when the electron is near the core, and the interaction is effectively short range. This allows for the use of MQDT, as first noted by Giusti-Suzor and Zoller[16].

5.2.1 A 2-Level Example

Cooke and Cromer best illustrate the methods employed in this section, we will follow them and begin with a simple two level system, in this case a spin-$\frac{1}{2}$ particle in a box of length L with magnetic spin coupling at one end of the box. For clarity, we can say there is a field $\vec{B}$ from $0 < x < a$, where $a < L$.

We can denote our two spin states as m_1 and m_2 for spin up and down, respectively. We can construct a set of spinors appropriate to the direction of our magnetic field as,

$$M_\alpha = \sum_i U_{i\alpha} m_i, \tag{5.10}$$

where U is the correct unitary transformation matrix. We can then construct a set of basis wavefunctions for the region of zero magnetic field. Matching boundary conditions at $x = a$, we can write a set of basis wavefunctions inside the box as,

$$\psi_\alpha = M_\alpha \sin(kx + \Delta_\alpha), \tag{5.11}$$

where Δ_α is the phase shift induced by the magnetic field. Our basis wavefunctions must also go to zero at our outer infinite wall at $x = L$, so we can write a second set of basis functions,

$$\phi_i = m_i \sin\big(k(x - L)\big). \tag{5.12}$$

We can construct a complete wavefunction out of linear combinations of either set of basis functions,

$$\Psi = \sum_i A_i \phi_i = \sum_\alpha B_\alpha \psi_\alpha. \tag{5.13}$$

Substituting Eqs. (5.10), (5.11), and (5.12) into (5.13), as well as judicious use of Euler's formula, we can express conditions for our coefficients as,

$$A_i e^{-ikL} = \sum_\alpha U_{i\alpha} B_\alpha e^{i\Delta_\alpha} \tag{5.14}$$

Multiplying both sides by $\sum_i U_{ik}$, gives us

$$\sum_i U_{ik} A_i e^{-ikL} = \sum_i \sum_\alpha U_{ik} U_{i\alpha} B_\alpha e^{i\Delta_\alpha}. \tag{5.15}$$

We can now exploit the fact that,

$$\sum_i U_{i\alpha} U_{ik} = \delta_{k\alpha}, \tag{5.16}$$

which lets us reduce Eq. (5.15) to,

$$\sum_i U_{i\alpha} A_i e^{-ikL} = B_\alpha e^{i\Delta_\alpha} \tag{5.17}$$

If we multiply Eq. (5.14) by e^{ikL} we have,

$$A_i = \sum_\alpha U_{i\alpha} B_\alpha e^{i(\Delta_\alpha + kL)} \tag{5.18}$$

If we impose the condition that A_i and B_α are real, we can split Eq. (5.18) into two equations,

$$A_i = \sum_\alpha U_{i\alpha} B_\alpha \cos(\Delta_\alpha + kL) \tag{5.19a}$$

$$0 = \sum_\alpha U_{i\alpha} B_\alpha \sin(\Delta_\alpha + kL) \tag{5.19b}$$

Similarly, we can multiply Eq. (5.17) by $e^{-i\Delta_\alpha}$ and have two relevant equations,

$$B_\alpha = \sum_i U_{i\alpha} A_i \cos(\Delta_\alpha + kL) \tag{5.20a}$$

$$0 = \sum_i U_{i\alpha} A_i \sin(\Delta_\alpha + kL) \tag{5.20b}$$

Both Eqs. (5.19*b*) and (5.20*b*) must have nontrivial solutions, and therefore,

$$\det|U_{i\alpha} \sin(\Delta_\alpha + kL)| = 0 \tag{5.21}$$

Setting $\Delta_1 = -\Delta_2 = \Delta$, we find solutions for k,

$$k = \frac{N\pi \pm \Delta}{L}, \tag{5.22}$$

and the associated energy,

$$E = \frac{N^2\pi^2 \pm 2N\pi\Delta}{2L^2}. \tag{5.23}$$

5.2.2 N-Level Atomic System

We can now walk through the same MQDT approach for calculating spectra for an N-level atomic system. Initially, we must first define a set of basis functions. The previous box outer wall at $x = L$ is replaced with the $-1/r$ Coulomb potential. The boundary condition at $r \to \infty$ is satisfied by

$$\phi_i = s(W_i, r)\cos(\pi\nu_i)\chi_i + c(W_i, r)\sin(\pi\nu_i)\chi_i, \tag{5.24}$$

for an electron of energy W_i and effective quantum number ν_i, where χ_i functions are a product of the angular components of the atomic wavefunction and the inner core electron wavefunctions. The $s(W_i, r)$ and $c(W_i, r)$ are the regular and irregular functions, as defined by Seaton[78], yielding wavefunctions that are normalized per unit energy. They are equivalent to Fano's f and g functions, the regular and irregular Coulomb functions and exhibit the appropriate asymptotic behavior as $r \to \infty$[80],

$$f(\nu, r) \to u(\nu, r)\sin\pi\nu - v(\nu, r)e^{i\pi\nu} \tag{5.25}$$

$$g(\nu, r) \to u(\nu, r)\cos\pi\nu + v(\nu, r)e^{i\pi(\nu+1/2)}, \tag{5.26}$$

with $u(\nu, r)$ and $v(\nu, r)$ are exponential increasing and decreasing functions of r, given by,

$$u(\nu, r) = (-1)^{\ell} \nu^{1/2} \pi^{-1} (2r/\nu)^{-\nu} e^{r/\nu} \left(\Gamma(\nu - \ell)\Gamma(\nu + \ell + 1)\right)^{1/2} \tag{5.27}$$

$$v(\nu, r) = (-1)^{\ell} \nu^{1/2} (2r/\nu)^{\nu} e^{-r/\nu} \left(\Gamma(\nu - \ell)\Gamma(\nu + \ell + 1)\right)^{-1/2}, \tag{5.28}$$

where Γ is the gamma function, defined as,

$$\Gamma(z) = \int_0^{\infty} t^{z-1} e^{-t} dt. \tag{5.29}$$

We can assume that for large r the potential is just a Coulomb potential, and only within some value r_c is the potential perturbed. We can therefore match our boundary conditions at $r = r_c$, forming

$$\psi_{\alpha} = \left(\sum_i U_{i\alpha} \chi_i s(W_i, r) \right) \cos(\pi \mu_{\alpha}) - \left(\sum_i U_{i\alpha} \chi_i c(W_i, r) \right) \sin(\pi \mu_{\alpha}), \tag{5.30}$$

where $-\pi\mu_{\alpha}$ is a scattering phase shift. Equations (5.30) and (5.24) are exactly analogous to Eqs. (5.11) and (5.12) in the previous section, where m_i is now represented by χ_i and the phase shift Δ_{α} is now $-\pi\mu_{\alpha}$. We can generate a total wavefunction out of linear combinations of either set of these basis functions,

$$\Psi = \sum_i A_i \phi_i = \sum_{\alpha} B_{\alpha} \psi_{\alpha} \tag{5.31}$$

Similar to Eqs. (5.14) and (5.17), we can generate a set of equations

$$\begin{aligned} A_i e^{-i\pi\nu_i} &= \sum_{\alpha} U_{i\alpha} B_{\alpha} e^{i\pi\mu_{\alpha}} \\ B_{\alpha} e^{i\pi\mu_{\alpha}} &= \sum_i U_{i\alpha} A_i e^{-i\pi\nu_i} \end{aligned} \tag{5.32}$$

If we again impose the condition that A_i and B_α are real, we generate a set of four equations,

$$A_i = \sum_\alpha U_{i\alpha} \cos\big(\pi(\nu_i + \mu_\alpha)\big) B_\alpha \tag{5.33a}$$

$$0 = \sum_\alpha U_{i\alpha} \sin\big(\pi(\nu_i + \mu_\alpha)\big) B_\alpha \tag{5.33b}$$

$$B_\alpha = \sum_i U_{i\alpha} \cos\big(\pi(\nu_i + \mu_\alpha)\big) A_i \tag{5.33c}$$

$$0 = \sum_i U_{i\alpha} \sin\big(\pi(\nu_i + \mu_\alpha)\big) A_i. \tag{5.33d}$$

Exploiting a few trigonometric identities, Eq (5.33*d*) can be rewritten as,

$$\cos \pi\mu_\alpha \Big(\sum_i U_{i\alpha} \big(\tan(\pi\nu_i) + \tan(\pi\mu_\alpha)\big) A_i \cos(\pi\nu_i) \Big) = 0. \tag{5.34}$$

This can be condensed to,

$$(\tan(\pi\mu) U^T + U^T \tan(\pi\nu))\vec{a} = 0, \tag{5.35}$$

where $\tan(\pi\mu)$ and $\tan(\pi\nu)$ are diagonal matrices and $\vec{a}$ has elements composed of $\cos(\pi\nu_i)A_i$. We can multiply both sides of the above equation by U, and substitution of $R = U \tan(\pi\mu) U^T$ further reduces Eq. (5.35) to

$$[R + \tan(\pi\nu)]\vec{a} = 0. \tag{5.36}$$

We can define $R + \tan(\pi\nu)$ as our effective Hamiltonian, with pseudoenergy Q,

$$\big(R + \tan(\pi\nu)\big)\vec{a} = Q\vec{a}. \tag{5.37}$$

The diagonal matrix $\tan(\pi\nu)$ describes the original basis, and R the perturbation.

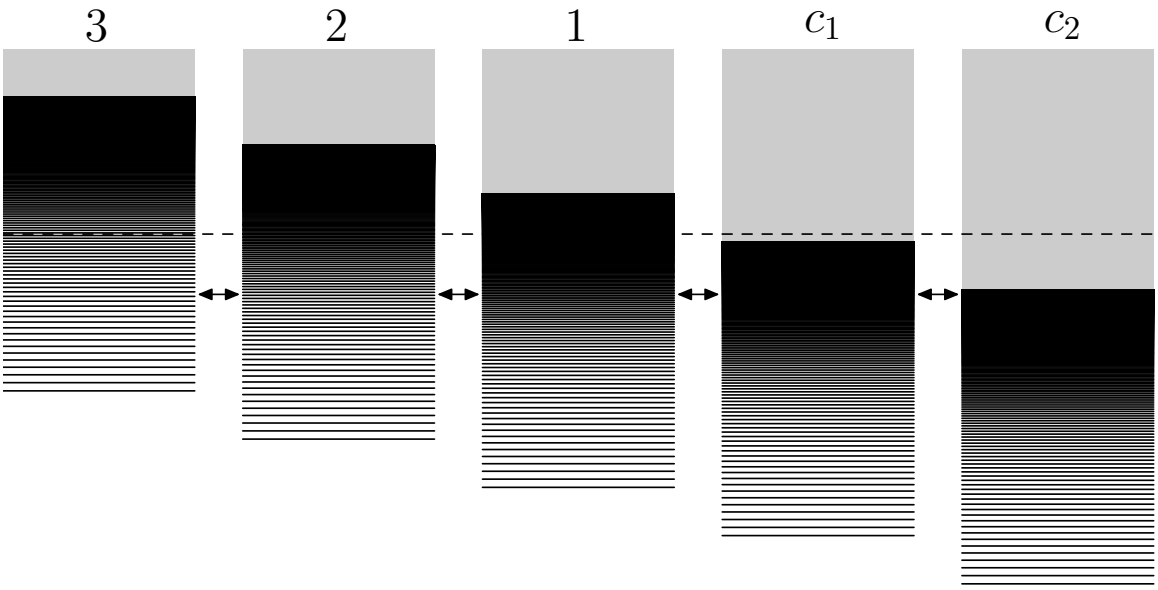

Figure 5.3: Simple MQDT model of microwave ionization, illustrating three bound channels and two continua, each shifted by one microwave photon.

The vector $\vec{a}$ represents an eigenstate constructed out of the original unperturbed basis. The R perturbation controls the mixing of the original states on to the $\vec{a}$ eigenstates.

As we have derived Eq. (5.36), it appears to apply only to bound states. However, we are interested in coupling to the continuum as well, the problem illustrated by Fig. 5.3.

We can note that the ν_i in Eq. (5.34) and ν in Eq. (5.36) represent both a binding energy and a phase, $\pi\nu_i$ or $\pi\nu$, respectively. It is the phase which is important in quantum defect theory, and we can include continuum states by replacing $\pi\nu_i$ by τ for all continuum states. The QDT matrix that describes the three bound, two

continua channels shown in Fig. 5.3 can be written as,

$$\begin{pmatrix} tan\pi\nu_3 & R_{bb} & & & & \\ R_{bb} & tan\pi\nu_2 & R_{bb} & & & \\ & R_{bb} & tan\pi\nu_1 & R_{bc} & & \\ & & R_{bc} & tan\tau & R_{cc} & \\ & & & R_{cc} & tan\tau & \end{pmatrix}. \tag{5.38}$$

Diagonalizing the QDT matrix at any energy gives the eigenphase-shifts τ_ρ. If there are n_c continua then there are n_c τ_ρ phase shifts. Diagonalizing the QDT matrix of Eq. (5.37) also gives the eigenfunctions. At any energy, for each ρ we obtain the wave function,

$$\Psi_\rho = \sum_i a_{i_\rho} \cos(\pi\nu_i)\psi_i(\nu_i) + \sum_j a_{c_{j_\rho}} \cos(\tau_\rho)\psi_{c_{j_\rho}}(\tau_\rho). \tag{5.39}$$

The effective quantum number ν_i in the bound channels in simply calculated as the positive solution to

$$W = W_i - \frac{1}{2\nu_i^2} \tag{5.40}$$

The wavefunction of Eq. (5.39) is not normalized, and we wish to normalize it as a continuum wave function, i.e. normalized per unit energy. The most straightforward method is to define a normalization constant for each ρ, such that,

$$N_\rho^2 = \sum_j A_{c_{j\rho}}^2 = \sum_j \frac{a_{c_{j\rho}}^2}{\cos^2 \pi\tau_\rho} \tag{5.41}$$

The normalized wavefunction is simply the unnormalized wavefunction, Eq. (5.39),

divided by N_ρ. Explicitly,

$$\Psi_\rho = \frac{1}{N_\rho}\left(\sum_i a_{i_\rho}\cos(\pi\nu_i)\psi_i(\nu_i) + \sum_j a_{c_{j_\rho}}\cos(\tau_\rho)\psi_{c_{j_\rho}}(\tau_\rho)\right). \tag{5.42}$$

Each normalized bound state coefficient can be written as

$$A^2_{i_\rho}(W) = (\frac{a_{i_\rho}}{N_\rho\cos(\pi\nu_i)})^2. \tag{5.43}$$

For each bound channel, the ρ values of $A^2_{i_\rho}$ are summed to produce i normalized A^2_i coefficients. Explicitly,

$$A^2_i(W) = \sum_\rho A^2_{i\rho}(W). \tag{5.44}$$

It is important to remember that this is the coefficient for the square of a wavefunction normalized per unit energy, which differs from the normal bound state normalization by $1/\nu_i^3$.

5.3 Combined Floquet-MQDT analysis

Typically, MQDT is used to model the different ionic states of an atom with different ionization limits. In this case, the different limits in this problem are the single ionization limit shifted by different numbers of microwave photons,

$$W_i = 0 + (i-1)\omega. \tag{5.45}$$

This defines the limit of channel 1 as $W_1 = 0$, channel 2 as $W_1 = \omega$, $W_2 = 2\omega$, and so forth. Similarly, we define the limits of continuum channels as

$$W_j = 0 - j\omega, \tag{5.46}$$

shifting the continuum limits to successively lower energies. The effective quantum number ν_1 is simply calculated as the positive solution to

$$W = \frac{-1}{2\nu_1^2}, \tag{5.47}$$

and successive ν_i are calculated as positive solutions to

$$\frac{1}{2\nu_i^2} = \frac{1}{2\nu_1^2} + (i-1)\omega \tag{5.48}$$

where ω is the microwave frequency in atomic units.

A requirement of QDT is that the coupling between channel be of short range. The n to n' electric dipole matrix element is given by[31],

$$\langle n|z|n'\rangle = \frac{0.4108}{(nn')^{3/2}\omega^{5/3}}. \tag{5.49}$$

The $1/n^3$ due to the normalization of the radial matrix elements at the core implies that the coupling is of short range, and thus satisfactory for use in a MQDT calculation.

It is straightforward to connect the electric dipole matrix element to the R matrix element of QDT. We can consider a bound state which can be ionized by a single photon, what in Fig. 5.3 would be a state in channel 1 going to channel c_1. In the low microwave field, or Fermi's golden rule limit, the photoionization rate Γ can be written as,

$$\Gamma = 2\pi|\langle n|\frac{zE}{2}|\epsilon\rangle|^2 = \frac{R^2}{\pi n^3}, \tag{5.50}$$

where the bound-continuum dipole matrix element is given by[31],

$$\langle n|\frac{zE}{2}|\epsilon\rangle = \frac{0.4108E}{2n^{3/2}\omega^{5/3}} \tag{5.51}$$

From this we can calculate the off-diagonal coupling R as a function of the field strength, E, as

$$R = \frac{0.4108\pi E}{2^{1/2}\omega^{5/3}}. \tag{5.52}$$

Note that this coupling matrix element does not depend on n and is therefore identical for all the bound-bound, bound-continuum, and continuum-continuum interchannel couplings.

To illustrate this method, we will perform an example calculation for a 5 V/cm 17.068 GHz microwave field with i bound channels and j continuum channels, where $i = j = 4$. The specific number of bound and continuum channels used is not important, as long as multiple continua are included in the calculation. It is only necessary to make a compromise between including all the relevant coupled states and keeping the computation time reasonably short.

From Cooke and Cromer we can find the j appropriate MQDT eigenvalues and eigenvectors by splitting our R matrix into four quadrants (bound-bound, bound-continuum, continuum-bound, and continuum-continuum) and solving,

$$\{R'_{cb}[R' + \tan \pi\nu']^{-1}_{bb} R'_{bc} - R'_{cc}\} a'_c = \epsilon_j a'_c. \tag{5.53}$$

Here R'_{cb} is a matrix of the form,

$$R'_{cb} = \begin{pmatrix} \cdots & 0 & R \\ \cdots & 0 & 0 \\ \iddots & \vdots & \vdots \end{pmatrix}. \tag{5.54}$$

The matrix R'_{bc} is similarly composed,

$$R'_{bc} = \begin{pmatrix} \vdots & \vdots & \iddots \\ 0 & 0 & \cdots \\ R & 0 & \cdots \end{pmatrix}. \tag{5.55}$$

Explicitly, we can also write down the R'_{cc} matrix as,

$$R'_{cc} = \begin{pmatrix} 0 & R & 0 & 0 & \cdots \\ R & 0 & R & 0 & \cdots \\ 0 & R & 0 & R & \cdots \\ 0 & 0 & R & 0 & \cdots \\ \vdots & \vdots & \vdots & \vdots & \ddots \end{pmatrix}. \tag{5.56}$$

Finally, the $[R' + \tan \pi\nu']^{-1}_{bb}$ matrix can be written as,

$$[R' + \tan \pi\nu']^{-1}_{bb} = \begin{pmatrix} \ddots & \vdots & \vdots & \vdots & \vdots \\ \cdots & \tan \pi\nu_4 & R & 0 & 0 \\ \cdots & R & \tan \pi\nu_3 & R & 0 \\ \cdots & 0 & R & \tan \pi\nu_2 & R \\ \cdots & 0 & 0 & R & \tan \pi\nu_1 \end{pmatrix}^{-1}. \tag{5.57}$$

Solving the above eigenvalue problem generates j eigenvectors, any one of which we can denote as a'_j. If we combine these eigenvectors into a $j \times j$ matrix, A'_{cc}, where each column represents a normalized eigenvector, we have a rotation matrix that transforms our initial continuum basis into eigencontinuum for a given ν. The general approach is to then calculate the admixture of the bound channels into the eigencontinua, and rotate then back to our original basis.

As pointed out by Jones, if we want to eventually compute the time propagated observed spectrum, it is important to keep track of the complex phase factors, $\frac{1-i\epsilon}{\sqrt{1+\epsilon^2}}$[81, 82]. This is not handled in the original Cooke and Cromer formulation presented above, since they are only interested in calculating the spectral amplitudes. A similar treatment of autoionizing $4pNd$ calcium wave packets by Pisharody and Jones[83] serves as an example, although an incorrect phase factor creates a factor of two discrepancy.

To calculate the admixture of bound channels into continuum channels, we can simply compute the matrix A_{bc}, computed as,

$$A_{bc} = -C_{bb}^{-1}[R' + \tan \pi\nu']_{bb}^{-1} R'_{bc} A'_{cc} \epsilon_{cc} A'^{T}_{cc} e^{i\pi\nu'}. \tag{5.58}$$

The matrix C_{bb}^{-1} is a diagonal matrix with elements $\frac{1}{\cos \pi\nu_i}$, and ϵ_{cc} is a diagonal matrix with elements $\frac{1-i\epsilon_j}{1+\epsilon_j^2}$, which provides the appropriate phase and normalization factors. The $e^{i\pi\nu'}$ factor shifts the maximum rate out of the bound states to time $t = 0$. Each row of the matrix A_{bc} represents the admixture of bound channel i in each of the j continuum channels, at a given ν. Repeating this process over many different ν lets us compute j arrays, where each array is the complex spectral amplitudes of the bound channels into one of the j continuum channels. The bound-continuum admixture amplitudes as a function of ν are plotted for each continuum channel in Fig. 5.6 for a 5 V/cm, 17.068 GHz coupling field. The complex phase is retained throughout the calculation, but not plotted in the figure below. Structure in the admixture amplitude at the 17 GHz microwave frequency is evident in all four channels.

However, we want to calculate the spectra not at time $t = 0$, but after a microwave pulse of time T. To do this we must convolute our calculated spectra with a sinc function that is the Fourier Transform of a step function of width T. We in

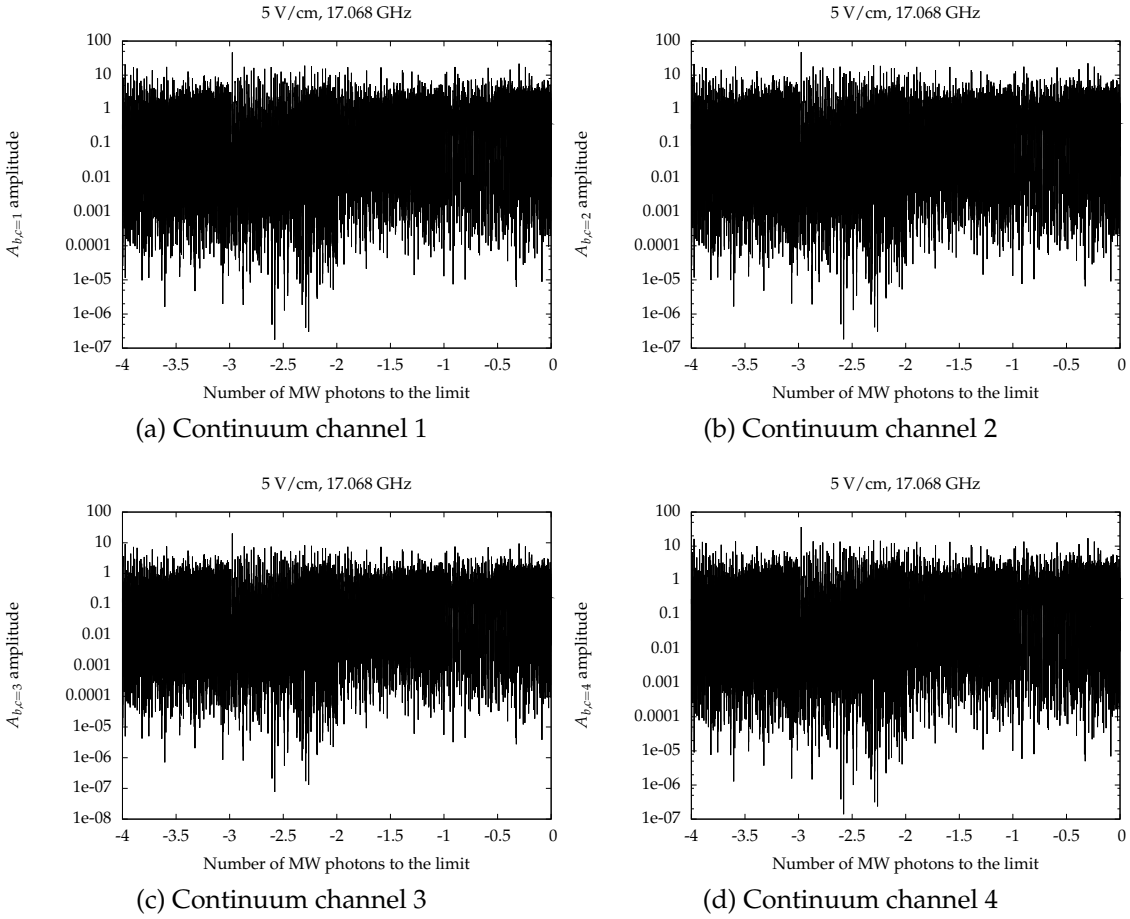

(a) Continuum channel 1 (b) Continuum channel 2

(c) Continuum channel 3 (d) Continuum channel 4

Figure 5.4: Admixture amplitudes for each of the four continuum channels in a four bound, four continuum MQDT calculation, with channels coupled by a 5 V/cm, 17.068 GHz microwave field. The complex phase is retained throughout the calculation, but not plotted here.

fact do not need to actually generate the required sinc function, and can instead compute the Fast Fourier Transform of the complex spectral amplitudes, and multiple each element of the k element transformed array by our step function of width T.

In practice, the step function array is defined as being a k element array of elements equal to one between $0 \leq t \leq T$, and zero elsewhere. If the initial complex spectral amplitude array begins at energy W_1 GHz and ends at W_2 GHz, the difference between successive elements of the step function are $1/abs(W_2 - W_1)$ ns. The step function array begins at time $t = 0$, and the second half of the array represents negative times. After multiplying the complex spectral amplitude array by the step function array, we can perform an inverse FFT to produce the complex spectral amplitudes after a microwave pulse of width T. We can refer to the complex spectral amplitude after pulse T as $F(T)$. The convolution with the sinc function is repeated for all j arrays representing transfer to each of the j continuum states included in the calculation. The results of the convolution of the admixture spectra with the sinc function corresponding to a 200 ns step function for each continuum channel are plotted in Fig. 5.5. The structure at the microwave frequency that was evident in the $t = 0$ spectra is now less clear.

In the lab we measure real values, and we must therefore convert our complex amplitudes to real amplitudes. We also measure not the population transferred out of the bound states, but instead the population remaining in the bound states. So, we can finally compute the remaining population not transferred to the continuum as,

$$1 - \sum_c |F(T)^2|, \tag{5.59}$$

at each ν and plot the results as a function of ν, as shown in Fig. 5.6, for a 200 ns, 5 V/cm, 17 GHz microwave pulse. A 5000-point moving average simulates the ex-

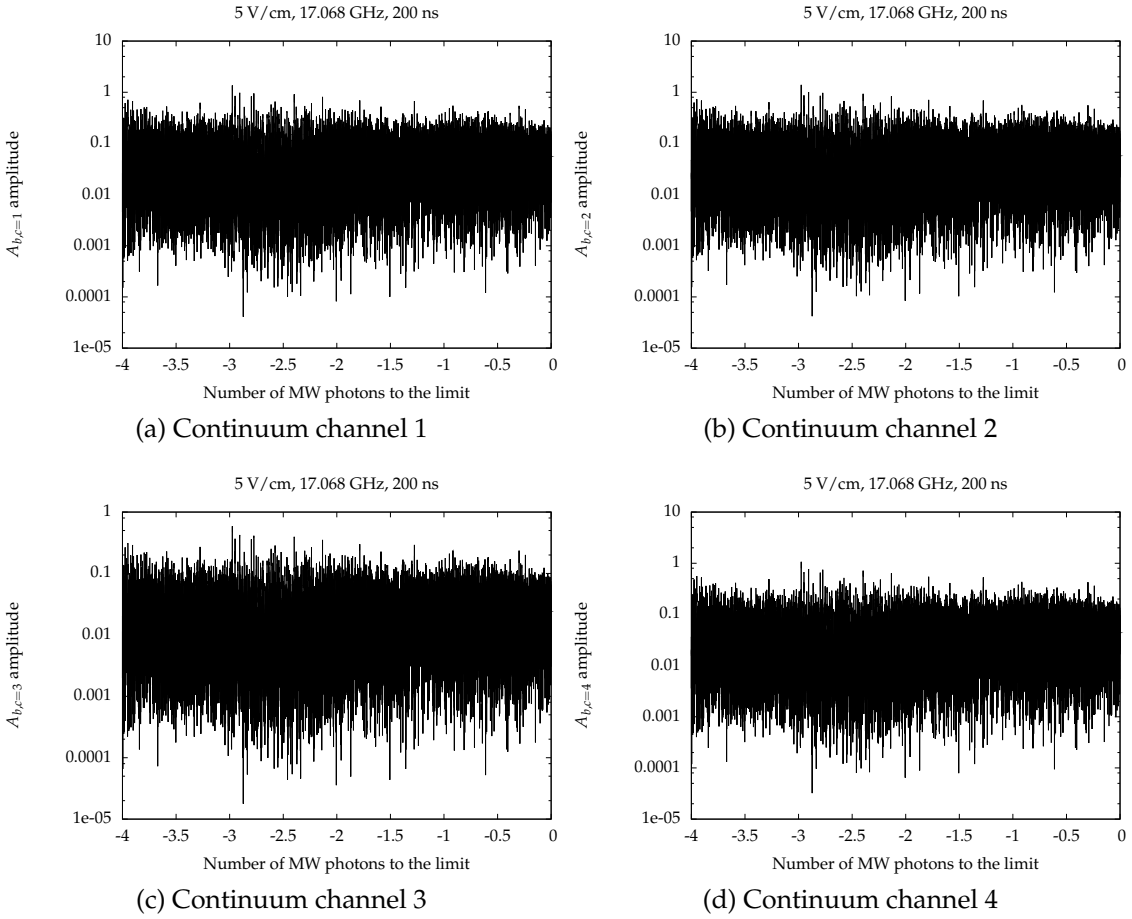

Figure 5.5: Admixture amplitudes for each of the four continuum channels in a four bound, four continuum MQDT calculation, with channels coupled by a 5 V/cm, 17.068 GHz microwave field, after a 200 ns pulse. The complex phase is retained throughout the calculation, but not plotted here.

perimental incoherent bandwidth of the excitation laser. Unfortunately, the 17 GHz structure experimentally observed is non-evident in the calculated results. However, the above MQDT process is not without promise. Increasing the coupling between channels drives more population from bound to continuum states, as does increasing the microwave pulse duration.

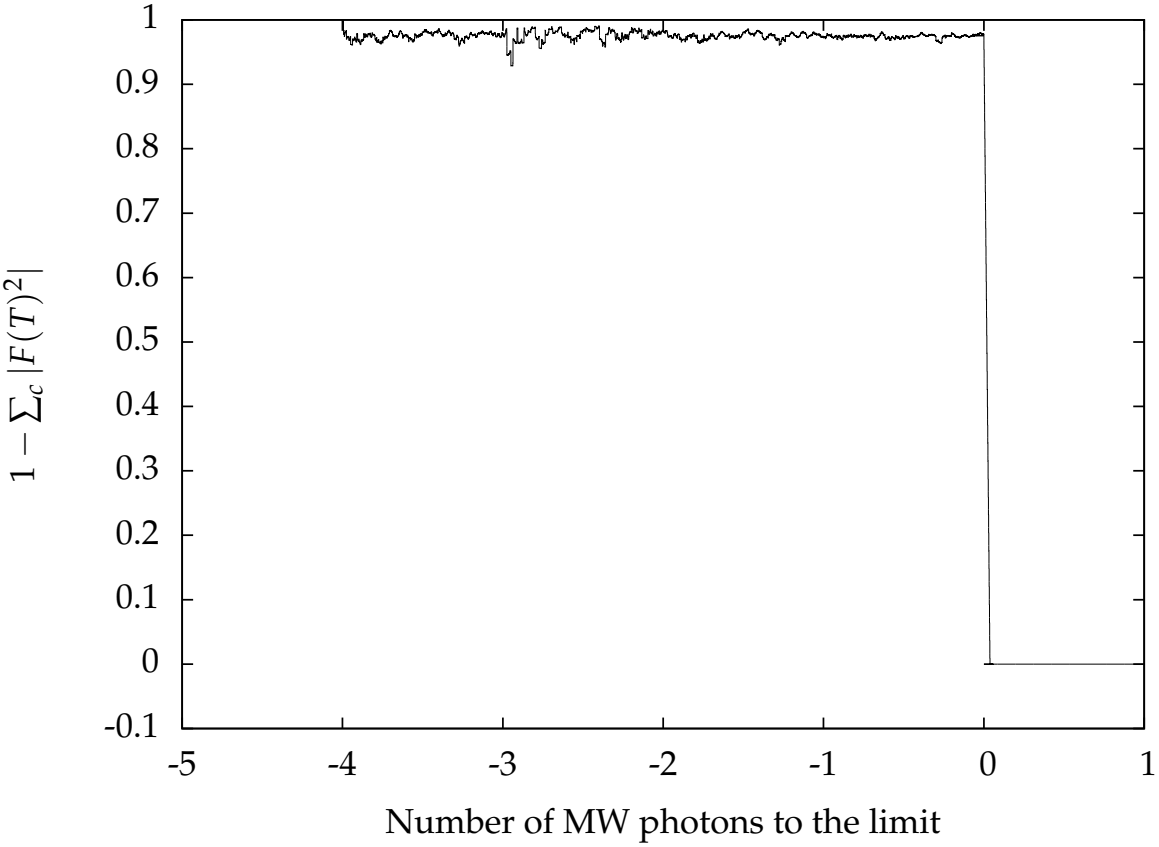

Figure 5.6: Calculated MQDT remaining atom spectra for a 200 ns, 5 V/cm 17 GHz microwave pulse.

Chapter 6

Final State Distributions

Previous work by Maeda and Gallagher[84, 85] and Noel, Griffith, and Gallagher[86, 87] has well illustrated atomic population transfer using microwave pulses in the regime where the scaled frequency is close to unity. The question remains of whether non-ionized atoms are transferred out of initial np states at high scaled frequency. This is best investigated by replacing the fast rising field ionization pulse used previously with a slower rising field ionization pulse. An example timing diagram is shown in Fig. 6.1.

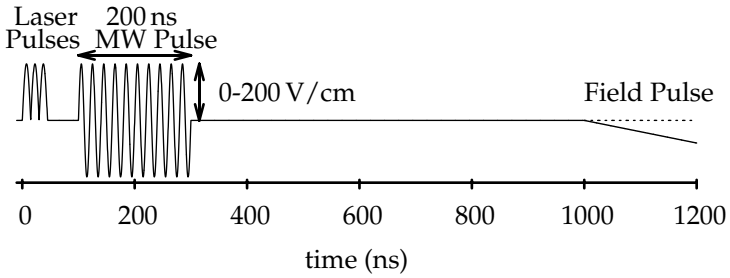

Figure 6.1: Experimental timing diagram.

The slowly rising field ionization pulse is generated using a trigger transformer, rising to 400 V in 1 μs. Excited atoms diabatically ionize at a field proportional to $1/9n^4$, so as the field increases lower n states ionize. This creates a temporal map

of the distributions of final states. A calibration scan with no applied microwave field is shown in Fig. 6.2a.

Rather than using a gated integrator, data are collected by capturing the oscilloscope trace of the MCP signal. The data are averaged over 256 laser shots and recorded by the computer via the oscilloscope's GPIB interface. The data can then be plotted as greyscale maps as a function of binding energy and detection time, where the greyscale corresponds to the MCP signal amplitude in millivolts. Since electrons are detected the signal is negative, and a large signal shows as black in the greyscale plots. The beginning of this chapter is an overview of the experimental results, followed by a simple Floquet model as a possible explanation of the observations.

6.1 Calibration

Previous work by Noel et al.[88] has shown that higher angular momentum states ionize in higher fields. If microwave pulses distribute initial np states to other n states, this needs to be discerned from transfer to other ℓ states. Since higher angular momentum states are not easily optically accessible, particularly with our current excitation scheme, this is a nontrivial problem.

This problem can be overcome by distributing the laser excited population over the Stark manifold using a small DC field pulse during state excitation. The electric field needs to also be smaller than the $1/3n^5$ Inglis-Teller limit to avoid mixing n-states. Experimentally, the SRS DG535 pulse/delay generator variable amplitude pulse that controls the microwave pulse was connected to the top plate over the excitation region, providing a 200 ns DC pulse during laser excitation. The results of 0.1 V/cm 0.2 V/cm, and 0.3 V/cm fields are shown in Fig. 6.2. These fields reach the Inglis-Teller limit at 265 GHz, 349 GHz, and 411 GHz, respectively. The $82p$

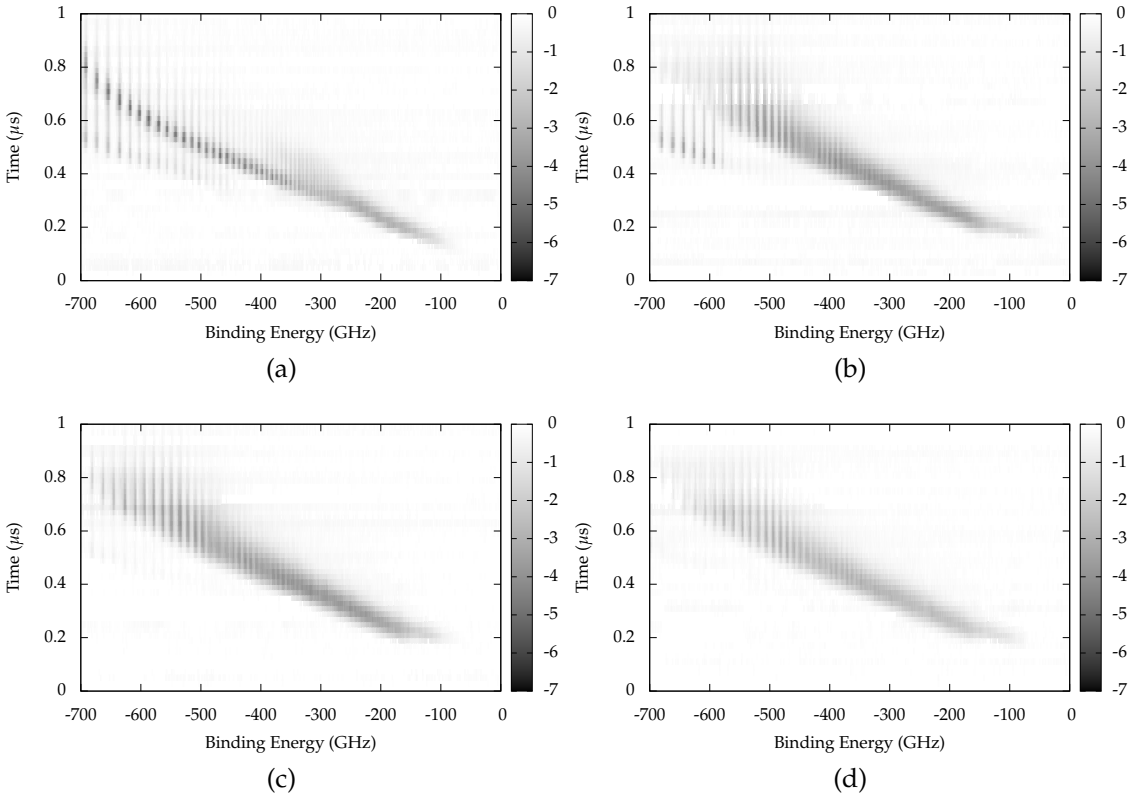

Figure 6.2: Extracting the final state angular momentum distributions. Figure (a) is the zero field state distribution. Figures (b)-(d) are the final state distributions when laser excitation occurs in the center of a 200 ns 0.1, 0.2, and 0.3 VDC pulse, respectively.

state, for example, bound by 490 GHz, is shown in Fig. 6.3, along with the $n = 82$ states in a 0.1 V/cm field. Both the diabatic and adiabatic ionization peaks are visible in the zero field case, and the peaks have a FWHM of approximately 50 ns. Applying a 0.1 V/cm field delays the diabatic peak of the detected atoms by 50 ns and broadens the electron signal to a FWHM of 160 ns. Therefore, higher ℓ states require slightly higher fields to ionize. The higher ℓ states for a given n appear to require roughly a factor of two higher field for ionization. The implications of this are that it is difficult to differentiate between transfer to higher ℓ states and transfer to lower n states.

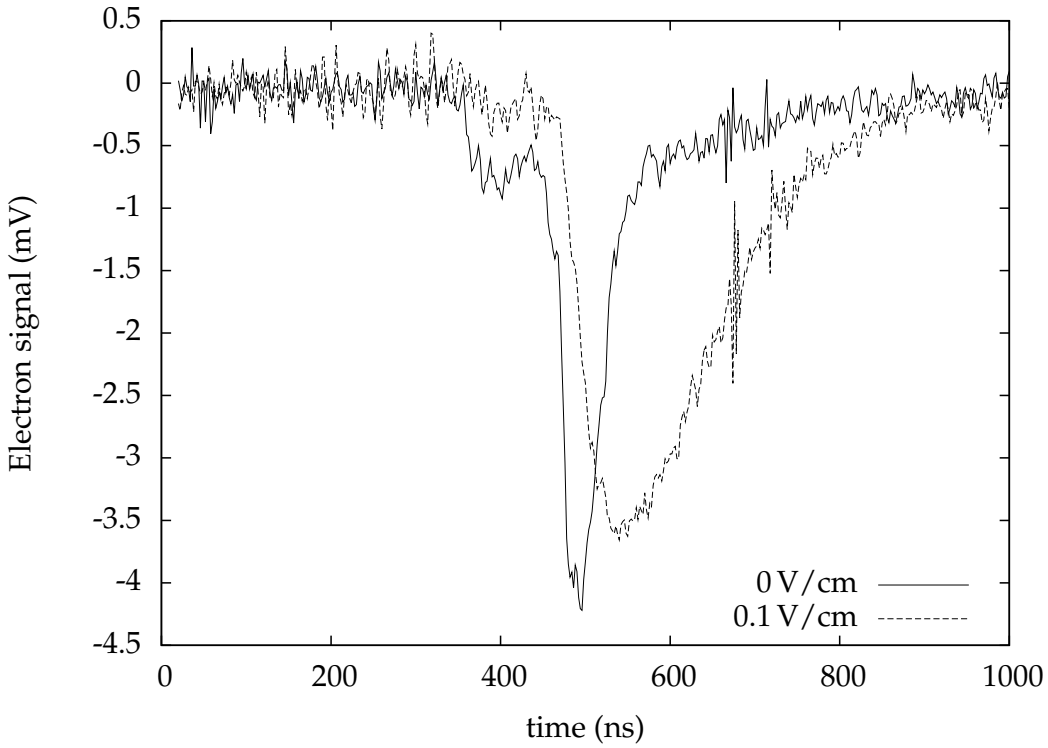

Figure 6.3: The $n = 82$ state excited in zero field and in a 0.1 V/cm DC pulse, as a function of detection time.

6.2 Experimental Results

6.2.1 Microwave power

Applying a microwave pulse redistributes the initial np population to both higher and lower lying states. Results for a 200 ns microwave pulse at 17.1105 GHz for a set of field amplitudes from 0.6 V/cm to 1.8 V/cm are shown in Fig. 6.4. State redistribution is small for the lowest field amplitude shown, and microwave ionization begins to interfere with final state detection for the largest field amplitude shown.

Scaling the final state distribution map, for example Fig. 6.4b, as a function of scaled microwave frequency is shown in Fig. 6.5. Population transfer out of the initial state occur near scaled frequencies, $\Omega = 1, 2, 4$. However, integer scaled

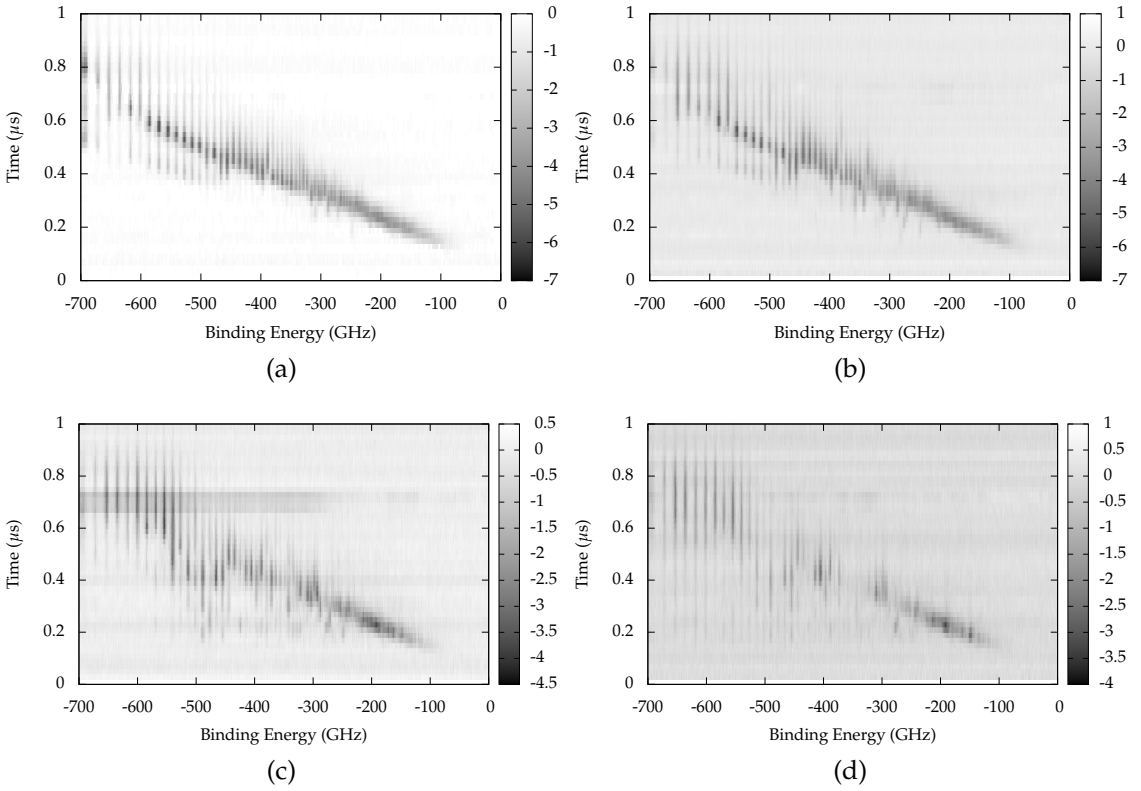

Figure 6.4: Final state distributions for 200 ns 17.1105 GHz microwave pulses for a set of field amplitudes. Figures (a) - (d) are for field amplitudes of 0.6 V/cm, 0.9 V/cm, 1.2 V/cm, and 1.8 V/cm, respectively.

frequencies do not predict whether population transfer occurs to higher states, such as at $\Omega = 4$, or lower states, such as at $\Omega = 1, 2$. The most likely explanation for population transfer near integer scaled frequency values is that they lie close to integer Δn transitions resonant transitions. The respective $p - s$ and $p - d$ $\Delta n = 2$ transitions occurs at $\Omega = 1.59$ and $\Omega = 1.93$, the $\Delta n = 3$ transitions at $\Omega = 2.54$ and $\Omega = 2.9$, and $\Delta n = 4$ transitions at $\Omega = 3.46$ and $\Omega = 3.83$. It appears as though there is no strong correlations between population transfer and scaled microwave frequency.

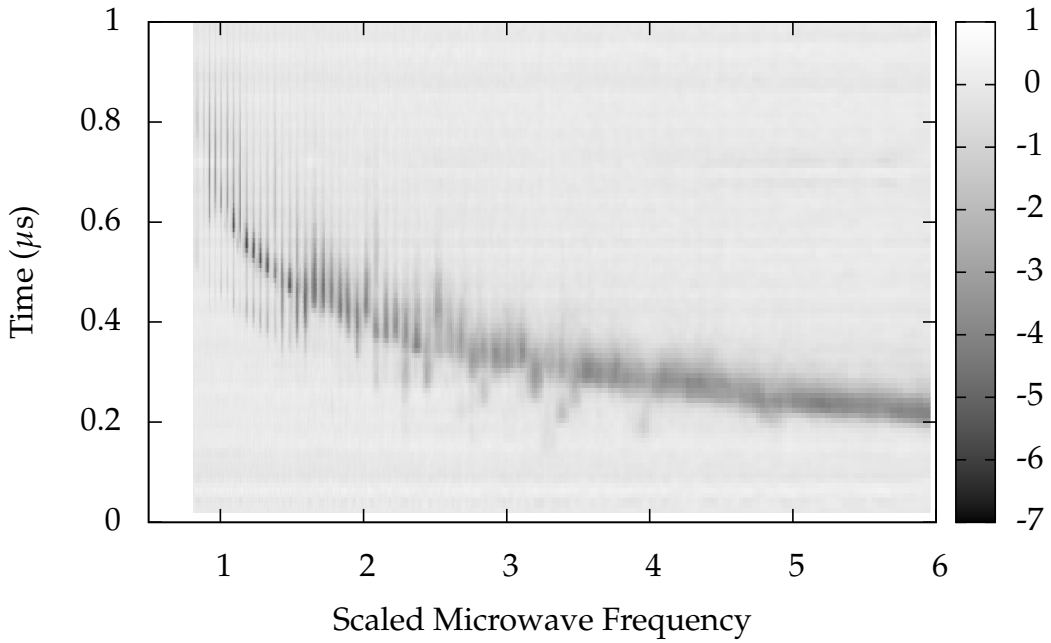

Figure 6.5: Final State distribution for 200 ns 17.1105 GHz, 0.9 V/cm microwave pulse as a function of scaled microwave frequency.

6.2.2 Microwave frequency

The Fabry-Perot cavity was tuned slightly off-resonant to determine the final state distribution changes as a function of microwave frequency. The -3 dB power points of the cavity were located 6 MHz apart, so the microwave frequency was tuned 3 MHz above the cavity resonant frequency of 17.1095 GHz and the input power was doubled. The results are shown in Fig. 6.6 for 200 ns 0.6 V/cm microwave pulses. There seems to be no discernible difference between the two data sets taken with a frequency difference of 6 MHz. However, when the cavity is operated well off-resonance, essentially as a microwave horn, significant spectral differences are observed. The results of 200 ns microwave pulses at 17.1095 GHz (on-resonant) and 17.2085 GHz (off-resonant) are shown in Fig. 6.7. The off-resonant microwave power is estimated to be comparable to the on-resonant 0.6 V/cm by comparison of microwave ionization rates.

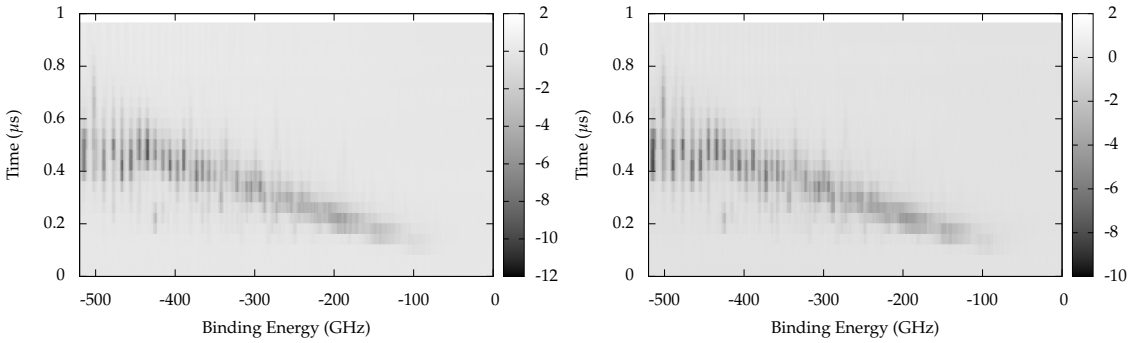

Figure 6.6: Final state distributions for 200 ns, 0.6V̇/cm microwave pulses at (a) 17.1065 GHz and (b) 17.10125 GHz.

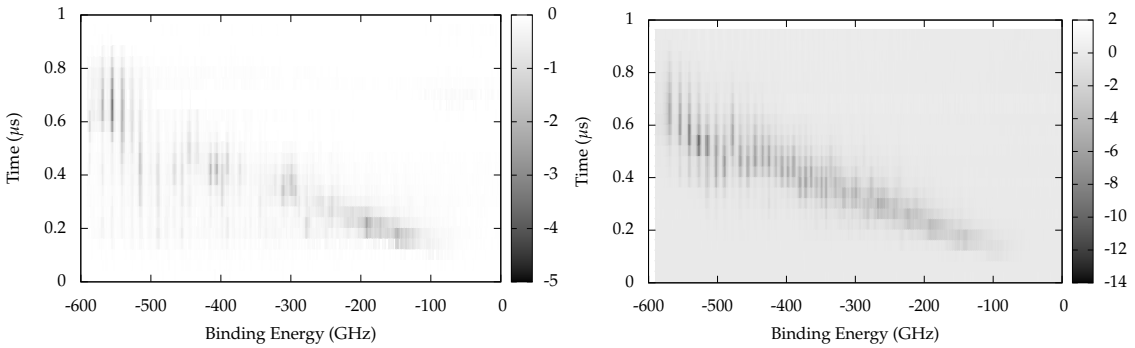

Figure 6.7: Final state distribution for 200 ns 0.6 V/cm microwave pulses at (a) 17.1095 GHz and (b) 17.2085 GHz

6.2.3 Microwave pulse length

Increasing the microwave pulse length does not significantly alter the final state distributions. Final state distributions for 17.1105 GHz, 0.6 V/cm microwave pulses at pulse lengths of 200, 400, 600, and 2000 ns are shown in Fig. 6.8. More microwave cycles would presumably allow for greater population transfer to weakly coupled final states, but the differences over an order of magnitude are negligible. However, 200 ns is already more than 3000 microwave cycles, and further work should investigate few-cycle microwave population transfer as previously done at lower scaled frequency[88].

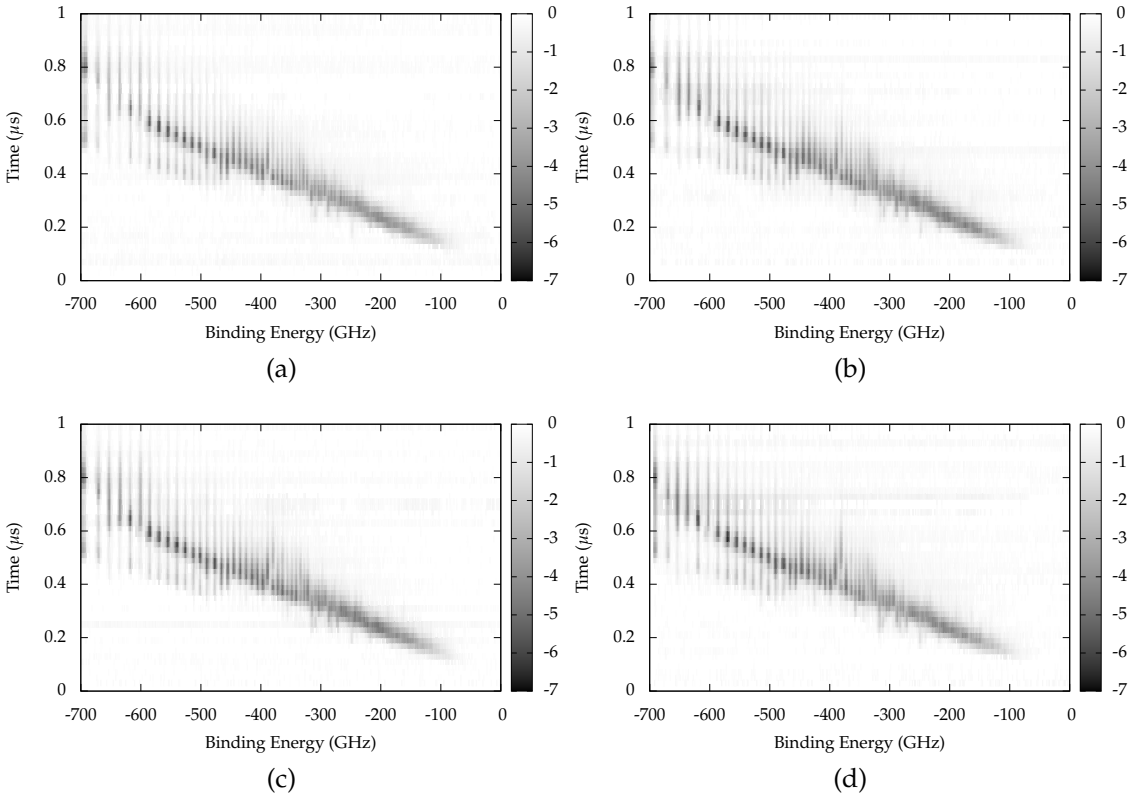

Figure 6.8: Final state distributions for 17.1105 GHz, 0.6 V/cm microwave pulses for a set of microwave pulse lengths. Figures (a) - (d) are for 200 ns, 400 ns, 600 ns, and 2 μs microwave pulse lengths, respectively.

6.2.4 High n

Some of the most interesting final state distribution results are seen at very high n, near the ionization limit. However, final state distributions of very high n states are experimentally the most difficult to obtain. The slowly rising field pulse is not as efficient as the ~ 5 ns field pulse for bound state electron detection, with efficiency decreasing as a function of increasing n. Electrons ionized by the fast field pulse receive a larger impulsive kick in the direction of the detector. When using the slow field pulse the ionized electrons are not strongly pushed towards the detector, and the detection efficiency suffers. This can best be overcome by decreasing the distance between the experimental region and the detector, at the expense of

increasing the stray field the atoms are exposed to. Data were taken with higher efficiency that better illustrate the dynamics at higher n by using a microwave horn and a field plate spacing of 2 cm. These data are shown for a 200 ns microwave pulse at 17.85 GHz and a field amplitude of approximately 3 V/cm in Fig. 6.9.

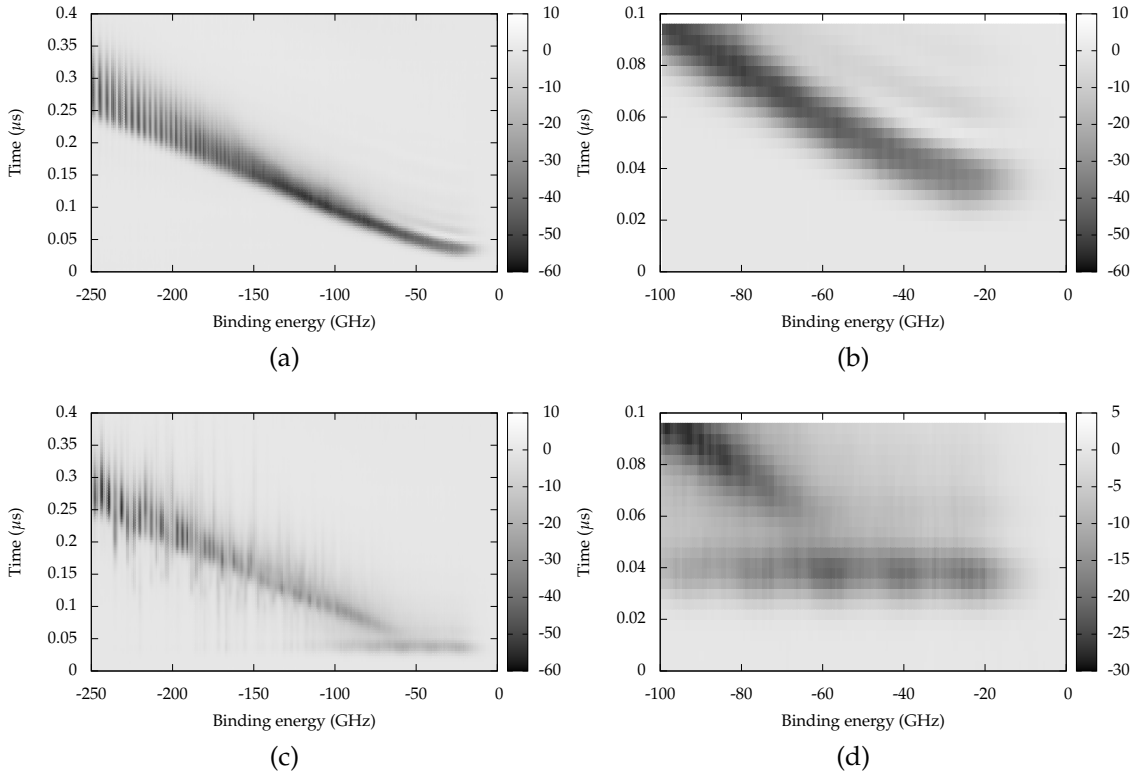

Figure 6.9: Final state distributions for (a)-(b) zero microwave and (c)-(d) 200 ns, 17.85 GHz, 3 V/cm.

Notably, for atoms bound by less than 100 GHz, population is clearly transferred out of the initial state to n states one photon below the ionization limit, as shown in Fig. 6.9d. Oscillations in the remaining population at the microwave frequency are clearly visible. These high n results illustrate that population is "trapped" one microwave photon below the limit, with population easily moving to n states centered about $n = 430$, but not ionizing. For example, a significant portion of the population initially bound by 90 GHz, five microwave photons from

the ionization limit, is transferred to n states one microwave photon from the ionization limit. There appears to be almost no population transfer from n states five microwave photons from the limit to states four, three, or two microwave photons from the ionization limit. This implies that the coupling between the final bound state and the continuum is what mediates microwave ionization. This coincides with the Floquet-MQDT model discussed in Chapter 5, as illustrated in Fig. 5.3.

6.2.5 Bias Voltage

Applying a small bias field has greatly increased the microwave ionization yield, both at low scaled frequency[26] and high scaled frequency[28]. This has previously been discussed in sections 3.2.2 and 4.2.2. The final state distributions when a small bias voltage is applied to top field plate are shown in Fig. 6.10, for bias fields from 0 to 30 mV/cm in 10 mV/cm steps. A 10 mV/cm bias field increases population transfer out of the initial np state to both higher and lower states.

6.3 Single State Analysis

Transitions from an initial np state to a distribution of final states appear to be describable using a Floquet diagram, with the initial np state making transitions to other $n\ell$ states via a series of avoided crossings. To make the calculations more manageable and the resultant plots clearer, angular momentum states for $\ell > 6$ have been omitted. At least ten microwave photons above and ten microwave photons below the initial state are included in the calculation. The resultant Floquet diagrams are, in a word, messy. This section will use some of the clearer Floquet diagrams of adjacent n states to illustrate the viability of the technique to describe experimental final state spectra, shown in Fig. 6.11. The general observable trend

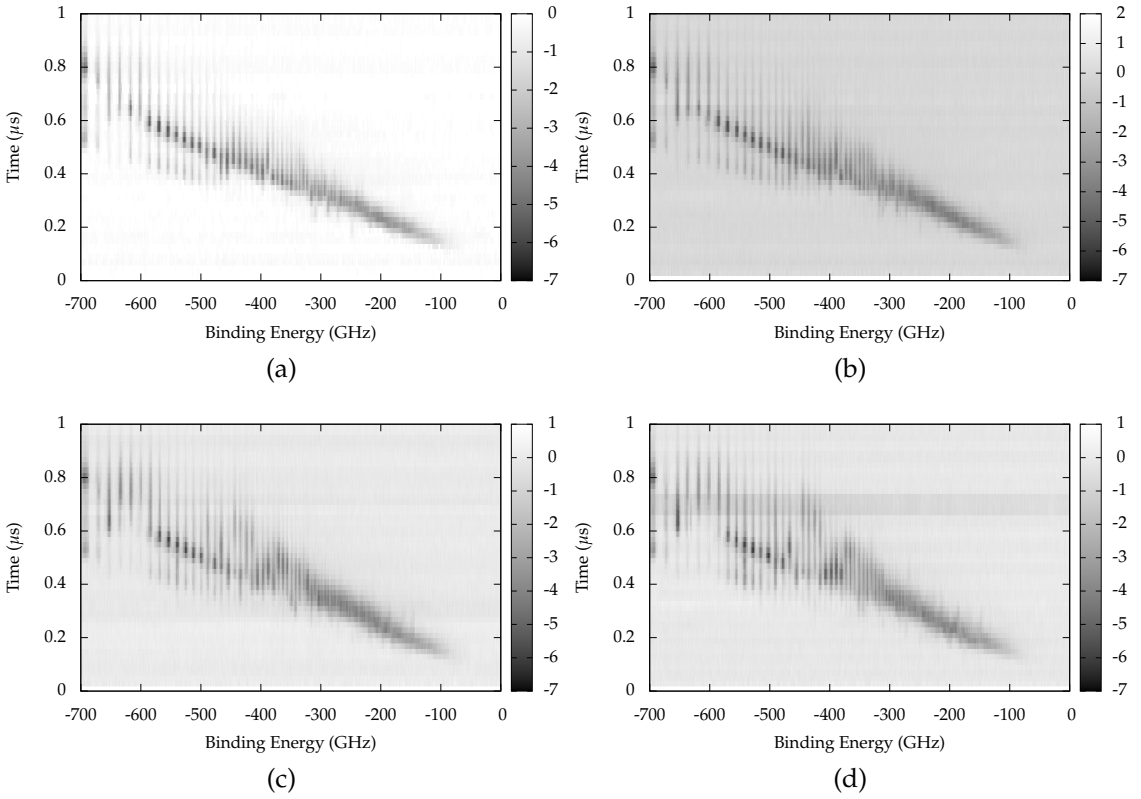

Figure 6.10: Final state distributions for bias voltages from 0 to 30 mV/cm and 17.1105 GHz, 0.6 V/cm, 200 ns microwave pulses. Figures (a) - (d) are bias fields 0 mV/cm, 10 mV/cm, 20 mV/cm, and 30 mV/cm, respectively.

seen in these single state plots is that the results are dominated by whether the microwave frequency is resonant with the states lying one photon above or below the initial state. In this energy regime for 17 GHz microwave photons, this corresponds to the $\Delta n = 2$ states.

The final state distributions for the initial $90p$ state after a 200 ns 17.1015 GHz microwave pulse for field amplitudes up to 1.8 V/cm are shown in Fig. 6.12a. The spectra are extracted vertical slices from Fig. 6.4 . The equivalent Floquet diagram is shown in Fig. 6.12b. The $90p$ state does not appear to strongly couple to other states, and the non-ionizing population primarily remains in the initial state.

The final state distributions when the laser is tuned to the $n = 91p$ transi-

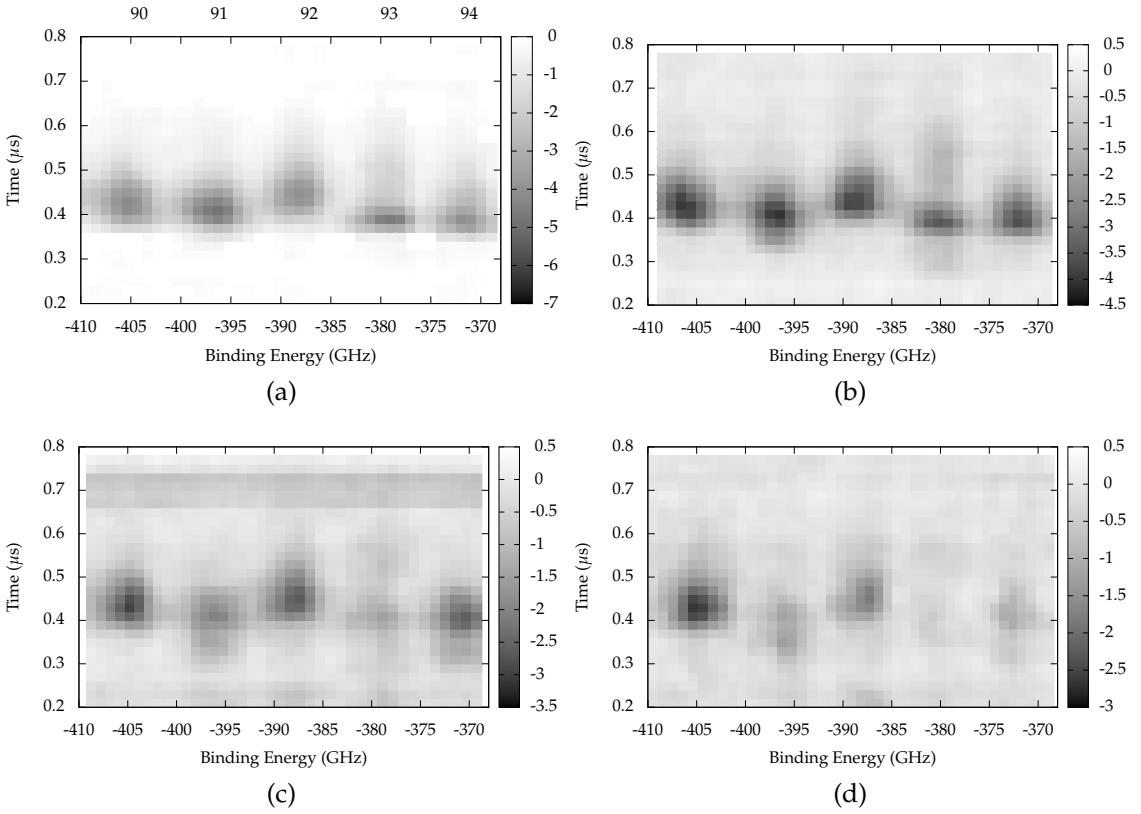

Figure 6.11: Final state distributions for 200 ns 17.1105 GHz microwave pulses for a set of field amplitudes in the range of $n = 90$ to $n = 94$. Figures (a) - (d) are for field amplitudes of 0.6 V/cm, 0.9 V/cm, 1.2 V/cm, and 1.8 V/cm, respectively.

tion for a set of 17.1015 GHz microwave fields from zero to 1.8 V/cm are shown in Fig. 6.13a. As the microwave field amplitude increases, the final state distribution begins to include higher and lower n states. Extracting the ionization times of np states in zero field, Fig. 6.2a, allows for decoding the composition of final states. For even small field amplitudes there is coupling to the $n = 84$ ($t = 462$ ns) state and $n = 100$ ($t = 342$ ns) state. For fields above 1.2 V/cm the initial $91p$ state is transferred to the $n = 116$ ($t = 286$ ns) state. These results are congruent with the $n = 91$ Floquet map, shown in Fig. 6.13b, where the $91p$ state couples with the $n = 116$ manifold in a field of 1.3 V/cm.

Final state distributions for the initial $n = 92p$ state are shown in Fig. 6.14a. For all microwave field amplitudes from 0.6 V/cm to 1.8 V/cm there is strong coupling

to lower lying states. At zero microwave field the $92p$ state is near-resonant with $n = 90$ transitions, lying between the $90d$ state and the rest of the $n = 90$ manifold. From the experimental spectra, transitions are most likely multiphoton transitions to $n = 90\ell$ states where $\ell \geq 4$. The $90p$ state ionize at $t = 412\,\text{ns}$, and higher angular momentum states ionize later. The $n = 92$ Floquet map, Fig. 6.14b, suggests an avoided crossing between the $n = 92p$ state and the $n = 90$ ($t = 412\,\text{ns}$) manifold in fields as small as $0.1\,\text{V/cm}$. However, dipole selection rules prevent direct transitions from $91p$ to states other than $90s$ and $90d$. Therefore, the transitions must be mediated by other off-resonant s and d states to reach higher angular momentum states. Experimentally, if the microwave field amplitude is increased to $1.2\,\text{V/cm}$ there is population transfer to $n = 134$ ($t = 216\,\text{ns}$), which is also in agreement with the calculated Floquet map, as well as small coupling to $n = 111$ at $t = 304\,\text{ns}$.

For a fourth state distribution, we can look at the $n = 93p$ initial state. The experimental final state distributions are shown in Fig. 6.15a for the same set of microwave fields as $n = 91p$ and $n = 92p$. The $n = 93p$ final state distributions are more complicated than the previously discussed states. Experimentally, there is coupling to the $n = 106$ and $n = 116$ states for fields greater than $0.9\,\text{V/cm}$, and coupling to the $n = 137$ state for a microwave field amplitude of $1.2\,\text{V/cm}$. There also is transfer to lower n states with coupling to the $n = 76$ manifold for a field of $0.9\,\text{V/cm}$. Interestingly, the initial $93p$ is almost completely depleted by a $1.8\,\text{V/cm}$ microwave pulse, which is well below the $\sim 8\,\text{V/cm}$ required for 50% ionization discussed in Chapter 3. The relevant Floquet map is shown in Fig. 6.15b. The Floquet map implies coupling at $1\,\text{V/cm}$ to higher 93ℓ states that is not obvious in the experimental spectra.

Finally, the final state distribution for the initial $n = 94p$ state is shown in

Fig. 6.16a. The equivalent Floquet map is shown in Fig. 6.16b. Much like the $n = 91$ state, there appears to only be some transfer to higher n states with microwave field amplitudes above 1 V/cm. These initial results suggest a more detailed exploration of these final state distributions as a function of applied microwave field and frequency is needed.

6.3.1 Dressed-state comparison

Non-ionizing population transfer to higher or lower states appears to depend primarily on the applied microwave frequency for a given n state. We can easily compare the final state distributions when the microwave pulse occurs after and during laser excitation, as shown in Fig. 6.17. As previously seen in the spectra shown in Chapters 3 and 4, the bound-state yield is lower when laser excitation occurs in the microwave field. However, it appears as though it again does not really matter how the initial state is excited and bound-bound population transfer is similar in the two cases. This implies that there is no adiabaticity condition necessary for turning on and off the microwave field.

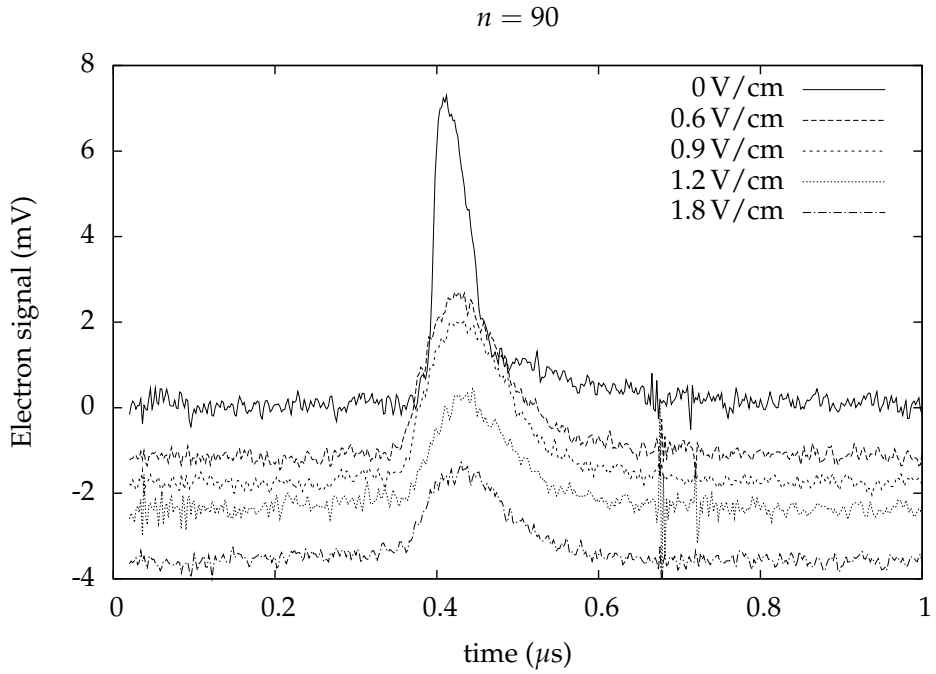

(a) $n = 90$

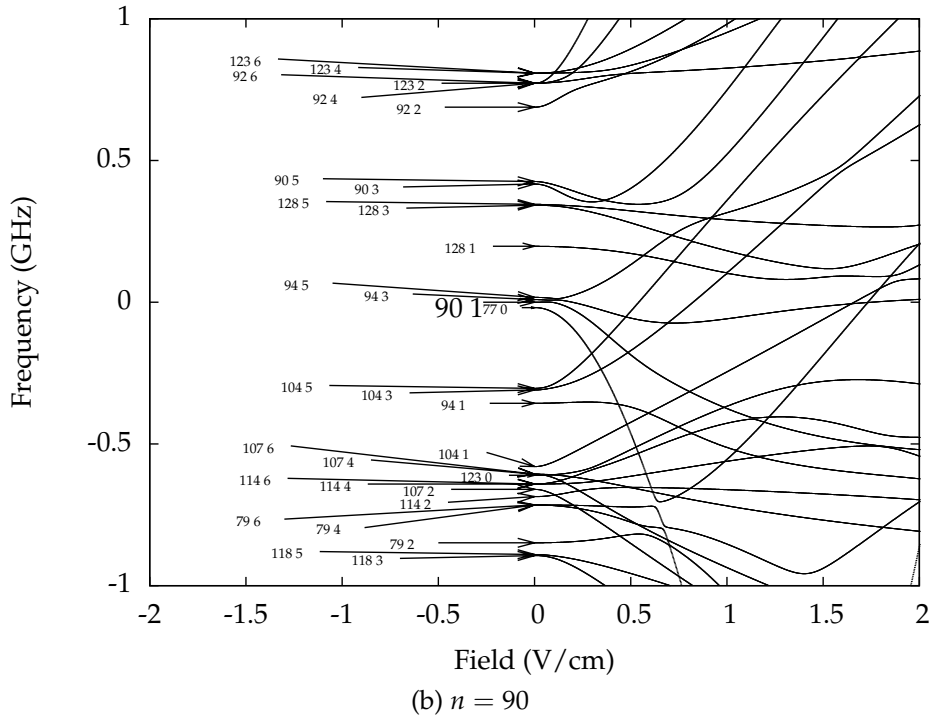

(b) $n = 90$

Figure 6.12: Final state distribution for $n = 90$ after a 200 ns 17.1015 GHz microwave pulse and the equivalent Floquet map. Zero field states are labeled by $n\ell$. The initial $n = 90p$ state is at 0 GHz in the Floquet map.

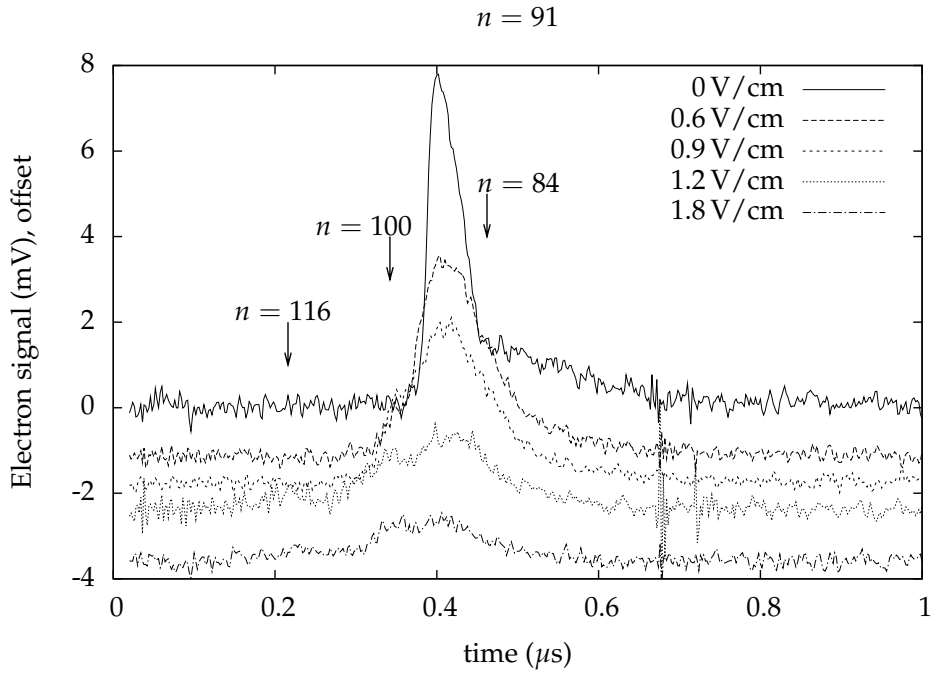

(a) $n = 91$

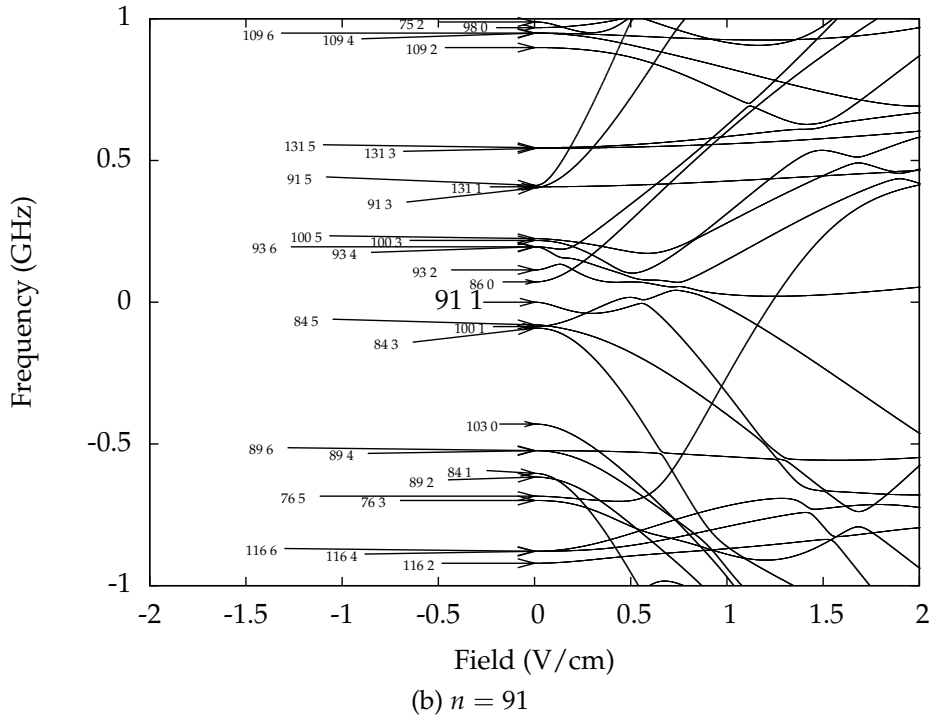

(b) $n = 91$

Figure 6.13: Final state distribution for $n = 91$ and the equivalent Floquet map. Zero field states are labeled by $n\ell$. The initial $n = 91p$ state is at 0 GHz in the Floquet map.

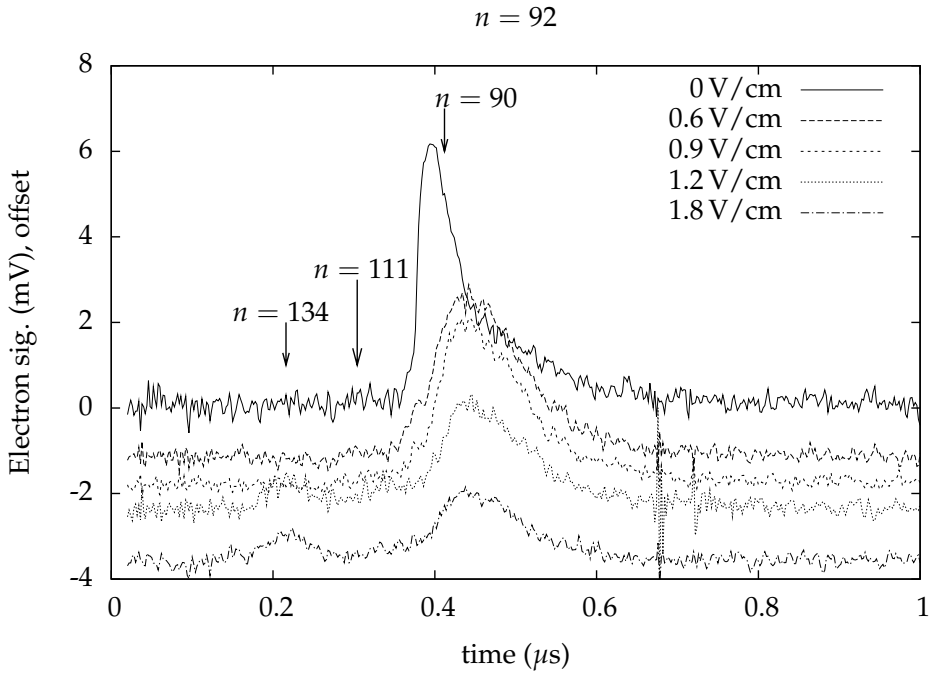

(a) $n = 92$

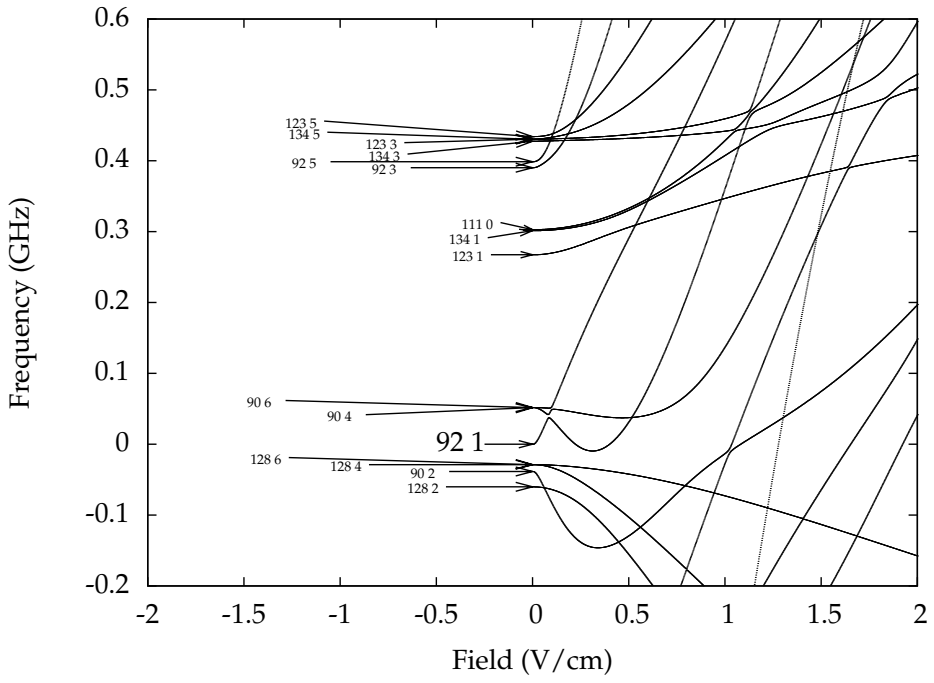

(b) $n = 92$

Figure 6.14: Final state distribution for $n = 92$ and the equivalent Floquet map. Zero field states are labeled with $n\ell$.

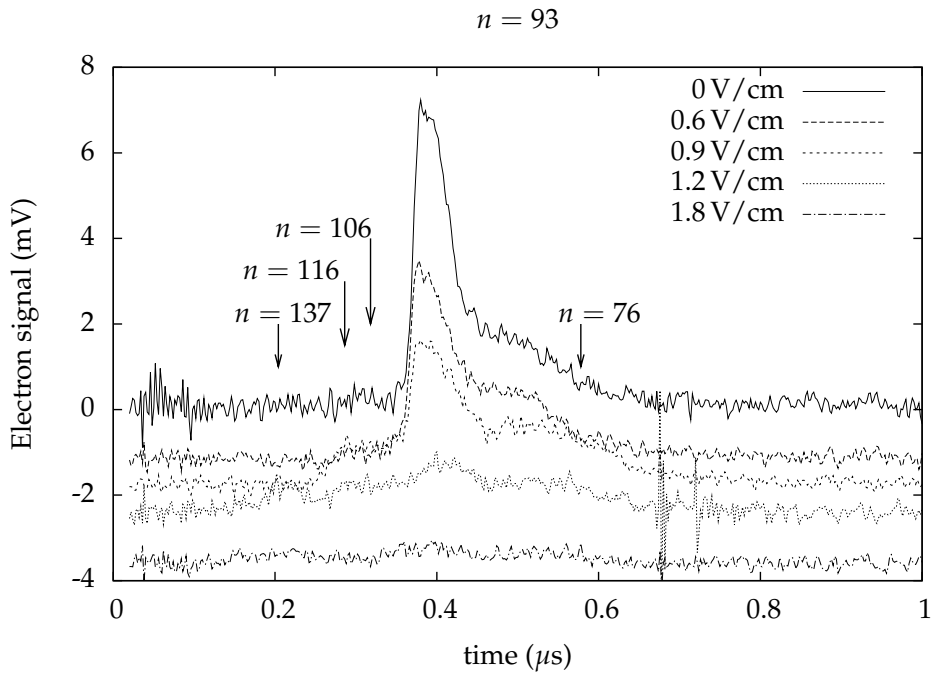

(a) $n = 93$

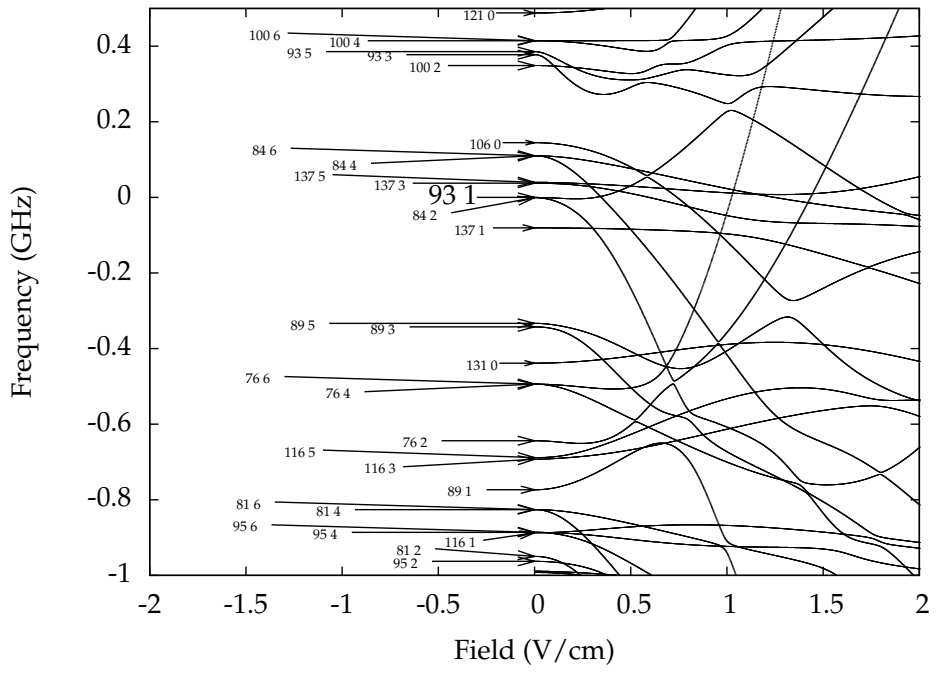

(b) $n = 93$

Figure 6.15: Final state distribution for $n = 93$ and the equivalent Floquet map. Zero field states are labeled with $n\ell$.

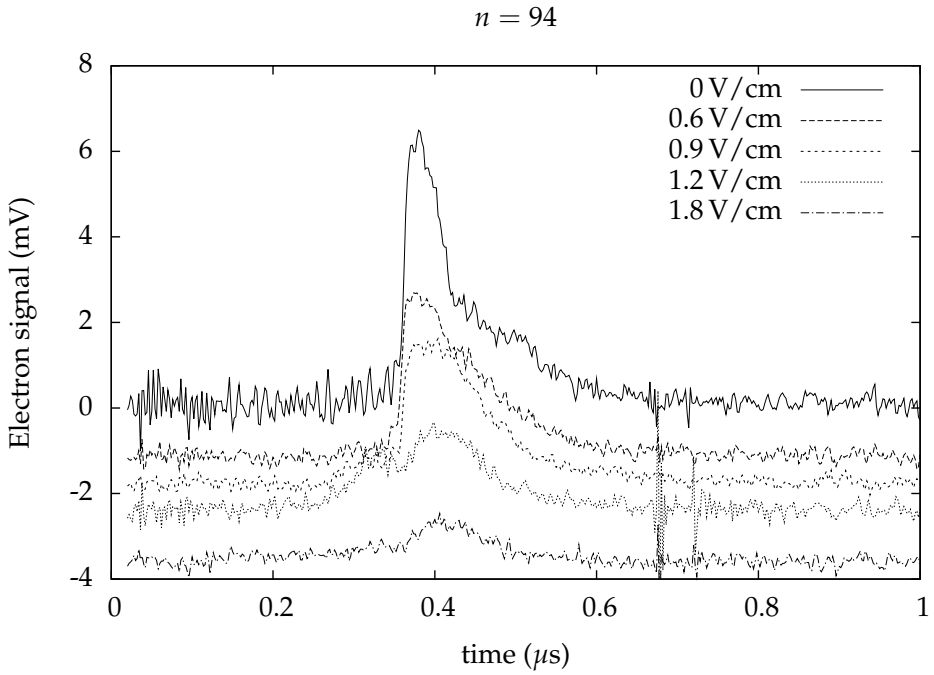

(a) $n = 94$

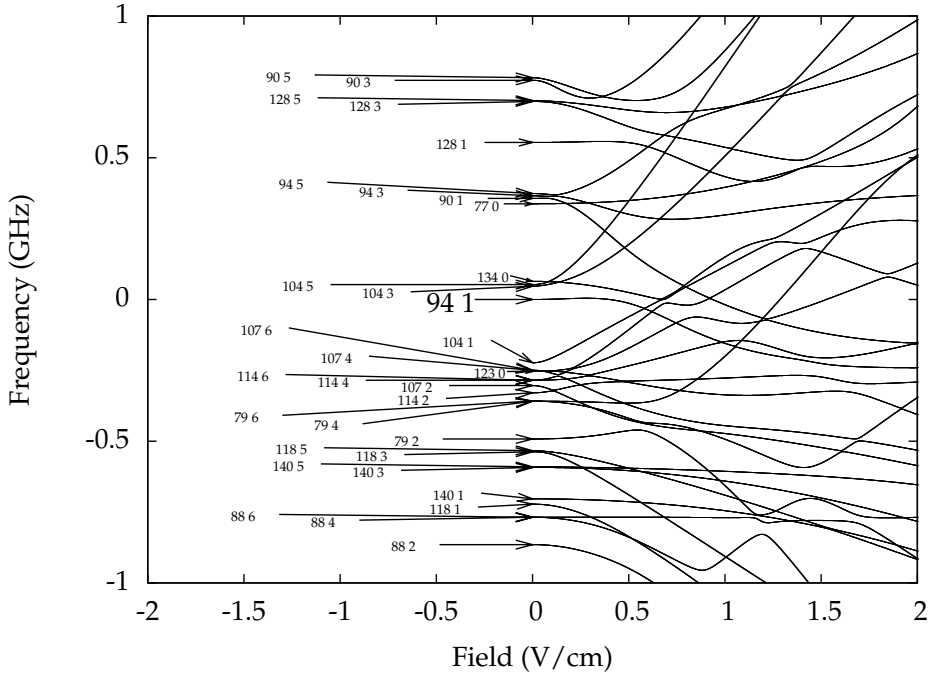

(b) $n = 94$

Figure 6.16: Final state distribution for $n = 94$ and the equivalent Floquet map. Zero field states are labeled with $n\ell$.

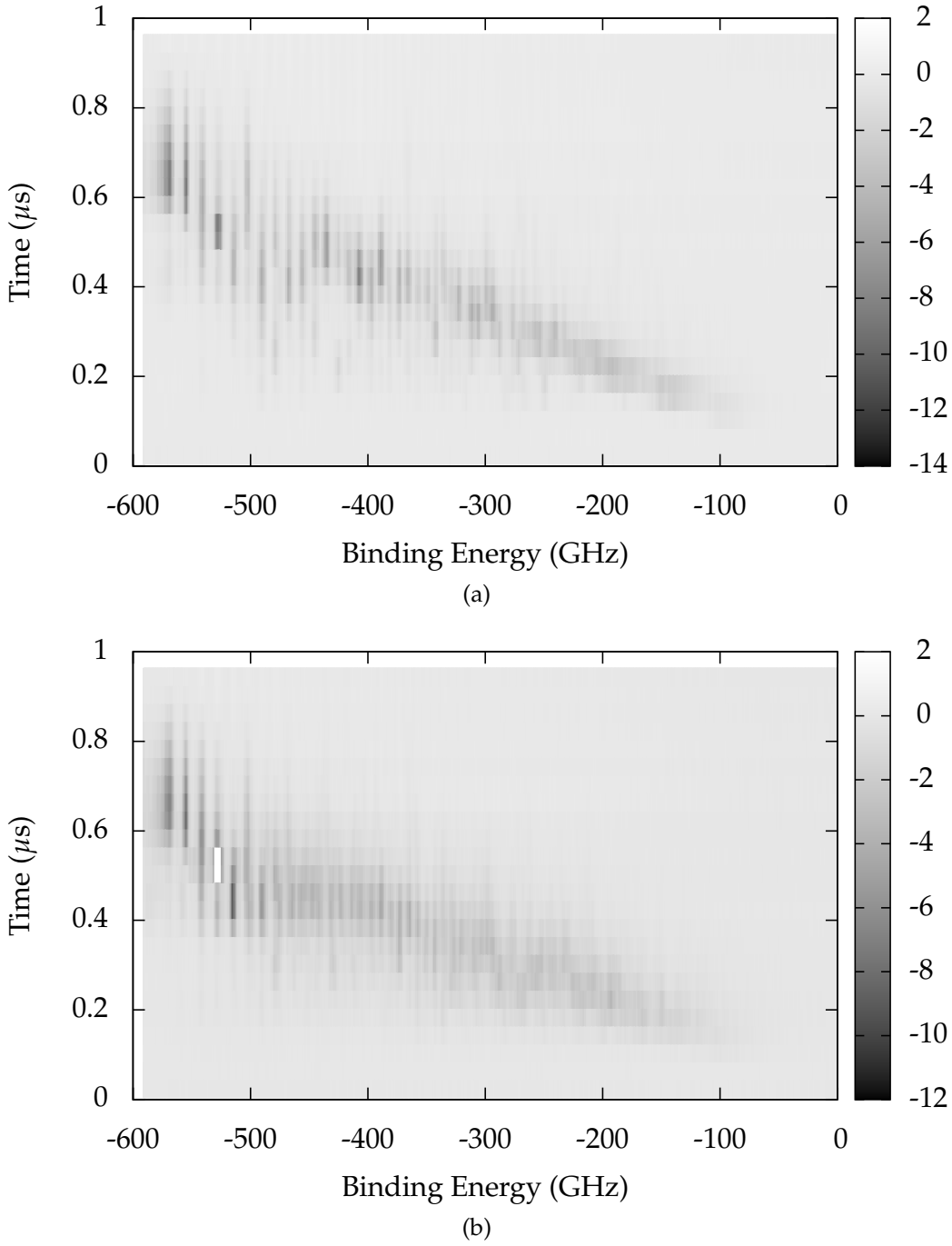

Figure 6.17: Final state distributions for laser excitation (a) before and (b) at the center of a 200 ns, 0.6 V/cm, 17.095 GHz microwave pulse.

Chapter 7

Conclusions

The results presented in this dissertation present an interesting picture of microwave ionization of Rydberg atoms. The original intent of the project was to connect field ionization to photoionization. It appears as though, as they say in New England, "you can't get there from here." The original picture of dynamic Anderson localization crossing over to a multi-photon photoionization picture simply does not hold. Instead, a coherent coupling of levels both above and below the ionization limit describe multiphoton microwave ionization.

Multiphoton microwave ionization occurs at rates similar to the single photon microwave ionization rates observed, where ten or fifteen microwave photon ionization appears to require a similar threshold field as single microwave photon ionization. The rates at which single microwave photon ionization occurs are more than an order of magnitude below the Fermi's Golden Rule predicted ionization rates for microwave fields on the order of 1 V/cm and above. These multiphoton ionization rates can be well described using a MQDT-Floquet model, coherently coupling together levels both above and below the ionization limit.

Along the path of connecting field and photoionization, this dissertation presents a variety of smaller conclusions. Temporally splitting the Coherent Evolution-30

pump light using a system of external Pockels cells to drive dye lasers has been ideal for np Rydberg Li creation at a kHz pulse repetition frequency. The high repetition rate of the Nd:YLF laser allows for data collection and analysis techniques not feasible at 30 Hz prf, and more than makes up for the slightly lower dye laser peak pulse powers.

Similar to the results seen at low scaled frequency, microwave ionization at both high scaled frequency and above the ionization limit is greatly increased by the application of a small electric field.

Above the ionization limit, maximum multiphoton microwave transfer to bound states is well described by a simple classical model first developed by Shuman*et al.* that accounts for the Coulomb potential of the atom. This model seems to well describe the maximum above-threshold energy transfer to bound states as a function of microwave field at 36 GHz, and properly describes previous results by Klimenko at 4, 8, and 12 GHz[67].

Finally, an initial survey of final state distributions for microwave transfer to higher and lower bound states is presented in Chapter 6. Bound state population appears to be "trapped" one microwave photon from the ionization limit, lending credence to a model of multiphoton microwave ionization where all ionization occurs through the n state one photon from the ionization limit. Population transfer to other bound states appears to be dominated by resonant single-photon transitions. A more comprehensive study of the final state distributions as a function of microwave frequency should be undertaken in the future. The most obvious next experiment would be to simply fix the excitation laser energy and microwave field amplitude, measuring the final state distribution as a function of microwave frequency. A similar experiment would be to instead fix the microwave frequency and measure the final state distributions as a function of microwave field ampli-

tude. These experiments should be relatively straightforward to conduct and analyze, and provide a solid jumping-off point for a future student new to the lab.

Appendix A

Nondispersing Bohr Wave Packets

PRL 102, 103001 (2009) Selected for a Viewpoint in *Physics* PHYSICAL REVIEW LETTERS week ending 13 MARCH 2009

Nondispersing Bohr Wave Packets

H. Maeda,[1,2,*] J. H. Gurian,[1] and T. F. Gallagher[1]

[1]*Department of Physics, University of Virginia, Charlottesville, Virginia 22904-0714, USA*
[2]*PRESTO, Japan Science and Technology Agency (JST), Kawaguchi, Saitama 332-0012, Japan*

(Received 30 September 2008; published 9 March 2009)

Long-lived, nondispersing circular, or Bohr, wave packets are produced starting from Li Rydberg atoms by exposing them first to a linearly polarized microwave field at the orbital frequency, 17.6 GHz at principal quantum number $n = 72$, which locks the electron's motion into an approximately linear orbit in which the electron oscillates in phase with the microwave field. The microwave polarization is changed to circular polarization slowly compared to the orbital frequency, and the electron's motion follows, resulting in a nondispersing Bohr wave packet.

DOI: 10.1103/PhysRevLett.102.103001 PACS numbers: 32.80.Rm, 32.80.Ee, 32.80.Qk

The most intuitive picture of an atom is classical, one in which the electron moves about the ion in a circular Bohr orbit. Although it may not be obvious how to reconcile this simple picture with the quantum mechanical description of an atom, given in terms of time-independent wave functions of energy eigenstates, the resolution of this apparent paradox was provided by Schrödinger [1]. He showed that for the harmonic oscillator that wave packets, with localized probability distributions which move as a classical particle does, can be constructed from coherent superpositions of the time-independent spatial wave functions of different energy eigenstates.

Wave packets remained theoretical constructs until the advent of mode-locked lasers, which have pulses short enough to provide adequate frequency bandwidth to produce coherent superpositions of several Rydberg states [2–4]. Rydberg states, those of high principal quantum number n, have small binding energies, Ry/n^2, where Ry is the Rydberg constant. More important, the energy spacing between adjacent n levels is $2\ \mathrm{Ry}/n^3$, which changes slowly with n. Thus, the Rydberg levels are approximately evenly spaced, and the orbital, or Kepler motion of the electron in a wave packet with an average principal quantum number $\bar{n}$ occurs at the Kepler frequency $f_K = 2\ \mathrm{Ry}/h\bar{n}^3$, where $2\ \mathrm{Ry}/h = 6.58 \times 10^{15}$ Hz. For $\bar{n} = 72$, $f_K = 17.6$ GHz. In Ref. [4], the Rydberg wave packets made were radial wave packets in which coherent superpositions of typically five np states were created, and the radial probability distribution breathed in and out at f_K, while maintaining p character [4]. More complex excitation schemes combining laser excitation with short unipolar pulses, often termed half-cycle pulses (HCP) [5–7], have been used to generate angularly localized wave packets in which the electron oscillates in an approximately linear or circular orbit [8,9].

As pointed out by Lorentz, the initial localization of the wave packet persists only for the harmonic oscillator, with its evenly spaced energy levels [10]. If, as in the Rydberg states, the levels are not evenly spaced the initially localized wave packet becomes dispersed in space, typically after five or ten orbits [11]. With a finite number of states, the spatial localization can revive, but eventually, decoherence destroys the localization, with the result that at most tens of orbits are observed, and the typical lifetime of a Rydberg wave packet is 100 ps [12]. Bialynicki-Birula *et al.* suggested that it should be possible to create a long-lived nondispersing circular wave packet by adding a weak circularly polarized field at the Kepler frequency to phase-lock the motion of the Rydberg electron [13]. Adding a magnetic field and using a linearly instead of circularly polarized field have also been proposed [14,15]. To date, nondispersing wave packets (NWP) have only been made with linearly polarized microwaves [16–18] and trains of HCPs [19], resulting in wave packets in which the motion of the electron is roughly linear [20], more like a mass oscillating on a spring than an electron in a Bohr orbit.

Here we report a straightforward and robust way of making nondispersing Bohr wave packets (NBWP). The essence of the method is to create a nondispersing, approximately linearly oscillating wave packet phase-locked to a linearly polarized microwave (MW) field and then slowly change the MW polarization from linear to circular. We chose this approach based on the observation that the electron's motion in a NWP in a linearly polarized MW-field remains phase locked either after a 40% change in the MW frequency [17], or turning the MW field off and then on again [21], the latter investigation suggested by Hänsch [22].

The essential idea of NBWP can be understood by considering an electron in a two-dimensional circular Bohr orbit around an ion in the x-y plane (Fig. 1). The combination of the Coulomb and centrifugal potentials forms a circular potential trough in the x-y plane, in which a classical electron with binding energy Ry/n^2 circulates about the ion at the Kepler frequency $f_K = 2\ \mathrm{Ry}/n^3$.

If we add a circularly polarized MW field rotating in the x-y plane at frequency f_K, the potential seen by the elec-

PRL 102, 103001 (2009) PHYSICAL REVIEW LETTERS week ending 13 MARCH 2009

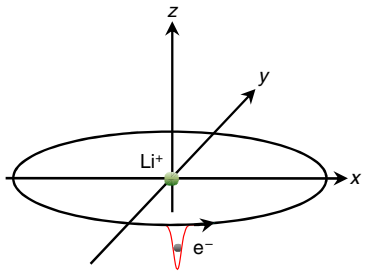

FIG. 1 (color online). Schematic diagram of the nondispersing Bohr wave packet showing the low point in the potential which rotates about the ion core.

tron is tilted with a low point which rotates about the z axis at f_K, as shown schematically in Fig. 1. In its lowest energy state the electron is localized at the low point, which rotates about the ion at f_K, and will remain there indefinitely.

In the experiment, Li atoms in a thermal beam in a vacuum chamber pass through a 17.564 GHz Fabry-Pérot MW cavity as shown in Fig. 2(a). The atoms are excited at the center of the cavity by three 5-ns laser pulses to np states of $70 \leq n \leq 75$ via the route $2s \rightarrow 2p \rightarrow 3s \rightarrow np$. The dye lasers are pumped by the first of two Nd:YAG lasers running at a 20-Hz repetition rate. Subsequent to the laser excitation the atoms are exposed to a combination of x- and y-polarized MW pulses. One such combination is shown in Fig. 2(b). First a pulse is injected through the upper mirror of the cavity, producing a y-polarized MW field. If the Kepler frequency of the atom is within 500 MHz of the MW frequency, a 1 V/cm MW field converts the atoms in the np state to a NWP in which the electron's motion is approximately one dimensional and phase-locked to the oscillating field, as shown in Fig. 2(c). Then a second MW pulse is injected into the cavity through the lower mirror to produce a field polarized in the x direction, the phase of which is shifted by 90° from the y-polarized field. As the amplitude of the x-polarized field rises to match that of the y-polarized field the MW polarization changes from linear to circular. The electron's motion is locked to the field and evolves from a linear to a circular orbit, as shown in Fig. 2(c).

To detect that the Rydberg atom has been converted from an np eigenstate to a linearly oscillating wave packet and then to a circular wave packet we observe the time variation of the x or y momentum of the electron with a 1/2-ps HCP, which is short compared to the 56-ps period of the Kepler orbit and the MW-field cycle. The HCP can be polarized in either the x or y direction. Typically the amplitude of, for example, an x-polarized HCP is set to ionize those atoms in which the electron has x momentum $p_x > 0$. We detect the remaining Rydberg atoms not ionized by the HCP by applying a field-ionization pulse after the HCP, as shown by Fig. 2(b). A negative voltage pulse is applied to the lower cavity mirror to field ionize the atoms

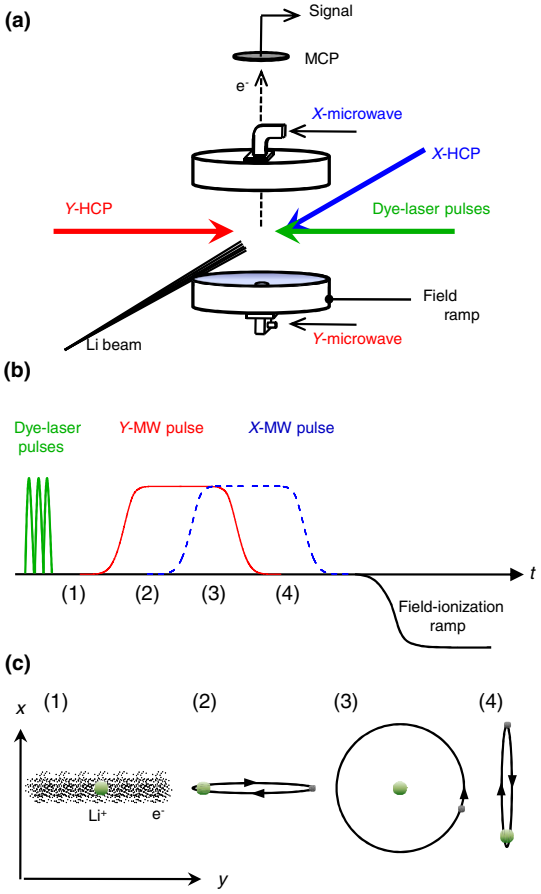

FIG. 2 (color online). Schematic diagram of the experiments. (a) The Li atomic beam passes through the center of the Fabry-Pérot MW cavity where it is excited by the dye-laser pulses. The x- and y-polarized MW fields are injected into the cavity through the mirrors, and a field-ionization pulse applied to the lower mirror ionizes the Rydberg atoms and ejects the resulting electrons for detection. (b) Timing diagram. After the dye-laser excitation a y-polarized MW pulse is injected into the cavity (—), then an overlapping 90°-phase shifted x-polarized pulse of the equal amplitude (- - -). Finally, a field-ionization pulse is applied to the lower mirror. The time-resolved momentum is sampled at times (1) to (4), when the MW field is zero, y-polarized, circularly polarized, and x-polarized, respectively. (c) The Rydberg electron orbits at times (1) to (4) showing the evolution from an eigenstate to y-polarized linear, then circular, and finally x-polarized linear wave packets.

and drive the resulting electrons through a hole in the upper cavity mirror to a dual microchannel-plate (MCP) detector [23]. The detector output is recorded with a gated integrator as the fine time delay of the HCP relative to the MW field is scanned. If the atom is in an energy eigenstate and

PRL 102, 103001 (2009) PHYSICAL REVIEW LETTERS week ending 13 MARCH 2009

the electron's motion is not phase-locked to the MW field there is no variation in the signal, but if the atom has become a NWP there is a variation with the 56-ps period of the MW field [16,18].

The Fabry-Pérot cavity is composed of two 82-mm-diameter brass mirrors of 102-mm radius of curvature with an on axis separation of 25.6 or 42.7 mm. The cavity is operated at 17.564 GHz on the TE 002 or TE 004 mode, with a typical cavity Q of 3800 and a filling time of 35 ns. The source of the MW field is a Hewlett Packard 8350B/83550A sweep oscillator which is amplified by a MITEQ solid-state or Hughes traveling-wave-tube amplifier to a power of up to 300 mW.

The HCP is generated when an amplified 200 fs, 810 nm Ti:sapphire laser pulse strikes a biased GaAs wafer. The MW oscillator is phase locked to the 230th harmonic of the 76 MHz repetition rate of the mode-locked Ti:sapphire oscillator. The coarse timing of the HCP is set by the electronic delay of the second Nd:YAG laser, which pumps the Ti:sapphire amplifier, and the fine delay is varied with an optical delay line for the 810 nm pulse. The jitter between the HCP and the MW field is 5 ps.

In Fig. 3 we show the transformation of Li atoms in the $72p$ eigenstate into a wave packet oscillating linearly in the y direction, then to a circularly polarized Bohr wave packet, and finally to a wave packet oscillating linearly in the x direction, as shown schematically in Fig. 2(c). The MW field amplitudes of the x- and y-polarized fields are ~ 1 V/cm, far smaller than the typical atomic field, $\propto 1/n^4$, felt by the Rydberg electron, 191 V/cm for $n = 72$. Specifically, we show the result of exposing atoms initially excited to the $72p$ state in zero field to the MW pulse shown in Fig. 2(b), a MW field initially polarized in the y direction, then circularly polarized, and finally polarized in the x direction.

We expose the atoms to x- and y-polarized HCPs at the four different times indicated in Fig. 2(b). The ionization produced by the HCP is detected as the fine delay of the HCP relative to the MW field is slowly scanned over many laser shots. If the HCP arrives before the MW pulse (1), we see no variation in the signal as the delay of the HCP is scanned for either polarization, as expected; the atoms are in the $72p$ state, an eigenstate. If the HCP arrives at (2), when only the y-polarized field is present, we observe the signals shown in Figs. 3(a) and 3(b). A strong modulation is observed with the y-polarized HCP but essentially none with the x-polarized HCP, as expected for a phase-locked wave packet oscillating in the y direction. We attribute the very weak modulation of Fig. 3(b) to a slight misalignment of the MW and HCP polarizations. If the HCP arrives at (3), when the field is circularly polarized, we observe the signals of Figs. 3(c) and 3(d). Modulation in the signal is seen for both polarizations, with a relative phase shift between them of 90°, as expected for a nondispersing circularly polarized Bohr wave packet. It is also apparent

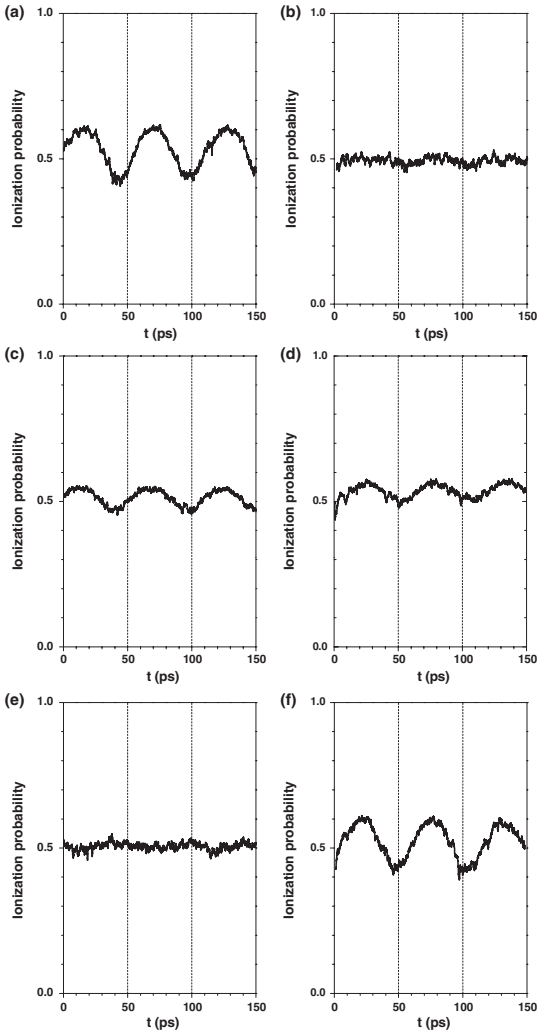

FIG. 3. Signals observed when atoms are exposed to y- and x-polarized HCPs and the fine time delay is scanned at the 4 times at the times of (2), (3), and (4) of Fig. 2(b). At time (2), with a y-polarized MW field (a) y-polarized HCP shows motion in the y direction, but (b) obtained with an x-polarized HCP shows no motion. At time (3), with a circular polarization, (c) y-polarized HCP and (d) x-polarized HCP both show motion, with a phase shift. At time (4), x-polarized MW field, (e) y-polarized HCP shows no y motion, but (f) the x-polarized HCP shows x motion.

that the modulations of both signals are smaller than the y-polarized signal of Fig. 3(a) by approximately $\sqrt{2}$, which is consistent with the fact that the peak momenta in the x and y directions are reduced by $\sqrt{2}$. Finally, if the HCP arrives at (4) a clear modulation is observed in the signal

PRL 102, 103001 (2009) PHYSICAL REVIEW LETTERS week ending 13 MARCH 2009

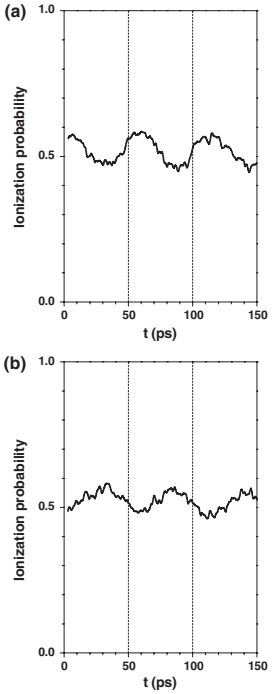

FIG. 4. Signals observed in right- and left-circularly polarized fields, time (3) of Fig. 2(b), when scanning the fine delay of the x-polarized HCP. (a) x-polarized MW field phase shifted by 90°. (b) x-polarized field phase shifted by $-90°$.

from the x-polarized HCP, as shown by Fig. 3(f), but not the y-polarized HCP, as shown by Fig. 3(e), indicating that there is now a NWP oscillating in the x direction. The polarization of the NWP has been changed from linear to circular to the orthogonal linear polarization by performing the same transformation on the MW field to which the wave packet is phase locked.

A circularly polarized wave packet can have left or right circular polarization, and in Fig. 4 we show the result of turning on the x-polarized field of Fig. 2(b) with phase shifts of $\pm 90°$. As shown, when the atoms are exposed to an x-polarized HCP at (3) of Fig. 2(b) the modulation exhibits a 180°-phase shift, while the modulation from the y-polarized HCP is unchanged, as expected for left- and right-hand circularly polarized wave packets.

In conclusion, we report the first observation of NBWP. The technique we have used is relatively simple and robust, and it is possible to make long-lived wave packets which can be used in other experiments. For example, one can imagine using the synchronized electron motion as the basis of phase sensitive detection. More generally, this work shows that it is straightforward to take advantage of the fact that a NWP is phase-locked to the MW field to manipulate the wave packet using the polarization, amplitude, and frequency of the MW field.

It is a pleasure to thank B. C. Gallagher, E. A. Bollwerk, and R. R. Jones for helpful comments. This work has been supported by the NSF Grant PHY-0555491.

*Present address: Department of Physics and Mathematics, Aoyama Gakuin University, Fuchinobe, Sagamihara 229-8558, Japan.

[1] E. Schrödinger, in *Collected Papers on Wave Mechanics* (Blackie & Son Ltd., London, 1928), p. 41.
[2] J. A. Yeazell and C. R. Stroud, Jr., Phys. Rev. Lett. **60**, 1494 (1988).
[3] A. ten Wolde *et al.*, Phys. Rev. Lett. **61**, 2099 (1988).
[4] J. A. Yeazell *et al.*, Phys. Rev. A **40**, 5040 (1989).
[5] C. Raman *et al.*, Phys. Rev. Lett. **76**, 2436 (1996).
[6] R. R. Jones, Phys. Rev. Lett. **76**, 3927 (1996).
[7] C. O. Reinhold *et al.*, Phys. Rev. A **54**, R33 (1996).
[8] J. Bromage and C. R. Stroud, Jr., Phys. Rev. Lett. **83**, 4963 (1999).
[9] J. J. Mestayer *et al.*, Phys. Rev. Lett. **100**, 243004 (2008).
[10] J. Mehra and H. Rechenberg, in *The Historical Development of Quantum Theory* (Springer-Verlag, New York, 1987), Vol. 5, p. 633.
[11] L. S. Brown, Am. J. Phys. **41**, 525 (1973).
[12] J. A. Yeazell, M. Mallalieu, and C. R. Stroud, Jr., Phys. Rev. Lett. **64**, 2007 (1990).
[13] I. Bialynicki-Birula, M. Kalinski, and J. H. Eberly, Phys. Rev. Lett. **73**, 1777 (1994).
[14] D. Farrelly, E. Lee, and T. Uzer, Phys. Rev. Lett. **75**, 972 (1995)
[15] D. Farrelly, E. Lee, and T. Uzer, Phys. Lett. A **204**, 359 (1995).
[16] H. Maeda and T. F. Gallagher, Phys. Rev. Lett. **92**, 133004 (2004).
[17] H. Maeda, D. V. L. Norum, and T. F. Gallagher, Science **307**, 1760 (2005).
[18] H. Maeda and T. F. Gallagher, Phys. Rev. A **75**, 033410 (2007).
[19] C. O. Reinhold *et al.*, Phys. Rev. A **70**, 033402 (2004).
[20] A. Buchleitner and D. Delande, Phys. Rev. Lett. **75**, 1487 (1995).
[21] H. Maeda and T. F. Gallagher (unpublished).
[22] T. W. Hänsch (private communication).
[23] T. F. Gallagher, *Rydberg Atoms* (Cambridge University Press, Cambridge, England, 1994), p. 103.

Appendix B

Coherent Population Transfer in an Atom by Multiphoton Adiabatic Rapid Passage

PRL 96, 073002 (2006) PHYSICAL REVIEW LETTERS week ending 24 FEBRUARY 2006

Coherent Population Transfer in an Atom by Multiphoton Adiabatic Rapid Passage

H. Maeda, J. H. Gurian, D. V. L. Norum, and T. F. Gallagher
Department of Physics, University of Virginia, Charlottesville, Virginia 22904-0714, USA
(Received 2 August 2005; published 23 February 2006)

Coherent population transfer in an atom using a sequence of adiabatic rapid passages through single-photon resonances is well-known, but it requires that the frequency sweep match the changing frequencies of the atomic transitions. The same population transfer can be effected via a single multiphoton adiabatic rapid passage, which requires only a small frequency sweep, if it is possible to select the desired multiphoton transition from the many possible transitions. Here we report the observation of population transfer between Rydberg states by high order multiphoton adiabatic rapid passage.

DOI: 10.1103/PhysRevLett.96.073002 PACS numbers: 32.80.Rm, 32.80.Bx, 32.80.Qk

Adiabatic rapid passage (ARP) is an approximately 100% efficient way to transfer population from one state to another, which makes coherent population transfer using a sequence of ARP's practical. Examples are using a chirped infrared-laser pulse to make a sequence of vibrational transitions in a slightly anharmonic diatomic molecule [1–3], the production of circular states by a sequence of $\Delta m = +1$ or -1 microwave (MW) transitions [4], and using a chirped MW pulse to change the principal quantum number n of atomic Rydberg states [5–7]. In the above examples the frequency of the atomic or molecular motion, i.e., the single-photon transition frequency, follows the changing frequency of the radiation. Consider the example of Fig. 1(a), a Rydberg atom initially in the state of $n = 72$, which has a Kepler or $\Delta n = 1$ transition frequency of 17.3 GHz. If this atom is exposed to a MW pulse chirped from 17.5 to 12 GHz it undergoes a sequence of ARP's up in n to the $n = 82$ state, which has a Kepler frequency of 12.2 GHz.

Here we report an alternative method of coherent population transfer, in which we replace the sequence of ARP's of single-photon transitions with ARP of a single multiphoton transition. For example, replacing the sequence of one-photon ARP's of Fig. 1(a) by ARP of the ten-photon $n = 72$ to $n = 82$ transition at 15.2 GHz [see Fig. 1(b)]. Using a multiphoton transition necessitates higher power, but, since there is only one transition, the range of the frequency sweep can be dramatically reduced. The advantages of using ARP's of multiphoton transitions for coherent population transfer were first suggested by Oreg *et al.* [8], and more recently by Gibson [9]. A well-known example is the "counterintuitive" pulse sequence [10], which leads to coherent population transfer in three-level systems by ARP of a two-photon transition, as demonstrated by Broers *et al.* [11]. The measurements reported here can be thought of as a multiphoton generalization of the counterintuitive pulse sequence, and they demonstrate that ARP using multiphoton transitions is, in fact, quite robust. In the sections which follow we outline the essential idea, describe our experiments, and discuss the implications.

A useful way of describing ARP is as an adiabatic traversal of an avoided crossing of Floquet levels [12]. We calculate the Floquet energy levels using a one-dimensional model for the atom in which the energy W is given by $W = -1/2n^2$ and the matrix element coupling adjacent n states by $\langle n|x|n+1\rangle = 0.3n^2$. We use atomic units, unless specified otherwise. A one-dimensional model provides a good description of Rydberg atoms in strong, linearly polarized MW fields [13,14].

In zero MW field the Floquet (or dressed-state) energy of each n state is given by

$$W = -1/2n^2 - (n - 75)\omega, \tag{1}$$

where ω is the MW angular frequency. The $n = 75$ energy is frequency independent, and the $n = 73$ energy, for example, increases twice as rapidly as the MW frequency [see Fig. 2(a)]. In Fig. 1(b) we show the $n = 72$ and $n = 82$ Floquet levels as a function of MW frequency near the ten-photon $n = 72$–82 resonance at 15.2 GHz. In zero MW field the two levels cross, as shown by the broken lines, and as shown by the solid lines, in a MW field of 3 V/cm there is an avoided crossing of magnitude $\Omega_{10} \approx 0.5$ GHz, which is the ten-photon Rabi frequency. ARP from $n = 72$ to 82 can be effected by sweeping the frequency through the ten-photon resonance in either direction as shown by the two arrows in Fig. 1(b).

The probability of ARP through an isolated k-photon resonance with a linear frequency sweep S is given by $P_k = \exp(-\pi^2\Omega_k^2/kS)$, where Ω_k is the magnitude of the avoided crossing in GHz and S is given in GHz/ns. The requirement for ARP is

$$\Omega_k > \frac{\sqrt{kS}}{\pi}. \tag{2}$$

In our experiments $S = 0.012$ GHz/ns, so Ω_k for $k = 1$ and 10 Eq. (2) requires $\Omega_1 > 35$ MHz and $\Omega_{10} > 110$ MHz, respectively. For $k = 1$ $\Omega_k = 0.3n^2E$, in which E is the MW-field amplitude, and for $k > 1$ an approximate requirement is that $0.3n^2E/\Delta_d \approx 1$ where Δ_d is the largest detuning from an intermediate-state resonance. For a

PRL 96, 073002 (2006) PHYSICAL REVIEW LETTERS week ending 24 FEBRUARY 2006

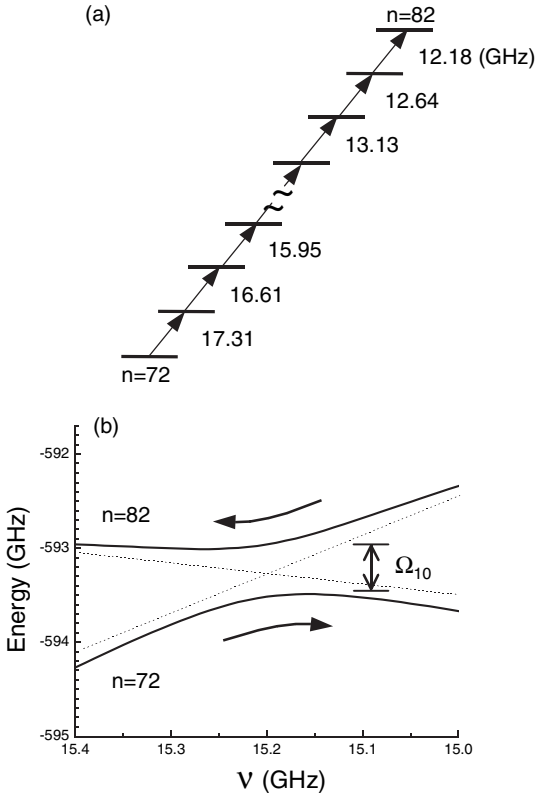

FIG. 1. (a) $n = 72 \rightarrow 82$ transition by a sequence of single-photon ARPs. (b) $n = 72$ and $n = 82$ Floquet states near the ten-photon resonance plotted as a function of MW frequency ν (solid curves). In zero MW field the two levels cross, as shown by the broken lines.

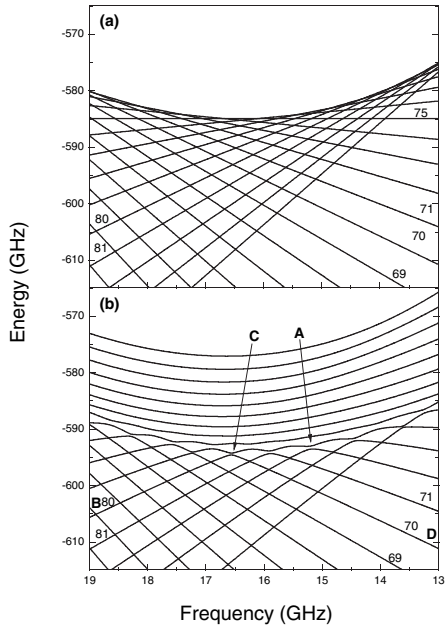

FIG. 2. (a) Floquet energy levels as defined in Eq. (1) for $60 \leq n \leq 84$ vs MW frequency in zero MW field. The $n = 69$, 70, 71, 75, 80, and 81 levels are labeled. The $\Delta n = 1$ resonances are the highest lying level crossings, and $\Delta n > 1$ crossings are lower in energy. (b) With a MW amplitude of 3 V/cm, the $\Delta n = k$, $k \leq 8$ avoided crossings become smooth curves, the $\Delta n = 10$ avoided crossings are recognizable as isolated avoided-level crossings, and the $\Delta n \geq 11$ avoided crossings are invisible on this scale. $n = 72$–82 ten-photon avoided crossing is denoted as A at 15.2 GHz. With a $19 \rightarrow 13$ GHz chirped pulse the atoms in level B pass to D through C.

k-photon transition the variation in the $\Delta n = 1$ frequency, $1/n^3$, leads to $\Delta_d = 3k/2n^4$ and $E = 5k/n^6$. Thus the requisite MW field E increases linearly with k, for $k > 1$. This simple model suggests that for $n = 75$ the required fields are 18 mV/cm and 1.4 V/cm for $k = 1$ and 10. From Eq. (1) it is apparent that the minimum required frequency sweep is

$$\Delta\nu \approx \frac{2\Omega_k}{k}, \tag{3}$$

which decreases as $1/\sqrt{k}$ and is $\sim$22 MHz for our slew rate and $k = 10$. For the avoided crossing shown in Fig. 1(b), with $E = 3$ V/cm, the minimum sweep is $\approx$ 100 MHz.

The ten-photon avoided crossing shown in Fig. 1(b) does not exist in isolation but is surrounded by other level crossings of both higher and lower order. Whether or not this avoided crossing is accessible is a crucial question. To address it we show in Fig. 2 the calculated Floquet energy levels for $n \sim 75$ vs the frequency of the MW field. As shown in Fig. 2(a) in zero MW field the k-photon, $\Delta n = k$ resonances appear as level crossings. The one-photon $\Delta n = 1$ resonances lie along the top of the energy levels shown in Fig. 2(a). The $k > 1$ resonances lie below them. The $\Delta n = 10$ resonance between the $n = 72$ and $n = 82$ levels of Fig. 1(b) occurs where the levels cross at 15.2 GHz. In Fig. 2(b) we show the same levels with a MW field of amplitude 3 V/cm. All level crossings become avoided crossings, and at this field the sequences of $\Delta n = k$ avoided crossings for $k \leq 8$ become smooth curves. For $\Delta n = k = 10$ there are recognizable avoided crossings, and for $\Delta n \geq 11$ the size of the avoided crossings decreases by an order of magnitude for an increase in Δn of one, producing avoided crossings invisible on the scale of Fig. 2. As shown by point A in Fig. 2(b) the ten-photon avoided crossing of Fig. 1(b) is by no means isolated, but we can use it to effect population transfer. The requirement is that it be traversed adiabatically and all other avoided crossings diabatically. An obvious approach

PRL 96, 073002 (2006) PHYSICAL REVIEW LETTERS week ending 24 FEBRUARY 2006

is a Gaussian pulse swept from 15.1 to 15.3 GHz with a peak amplitude of 3 V/cm.

In the experiment a beam of ground state Li atoms passes through a WR62 waveguide where the atoms are excited to np states by three 5 ns laser pulses using the sequence $2s \rightarrow 2p \rightarrow 3s \rightarrow np$. They are then exposed to a frequency swept MW pulse. Finally, a voltage ramp rising in 1100 ns is applied to a septum in the waveguide for selective field ionization. The electrons resulting from field ionization are ejected through a hole in the top of the waveguide and are detected with a dual microchannel-plate detector. Since the electrons have negligible flight time and atoms ionize at $F = 1/9n^4$ [15], the time-resolved electron signal allows us to determine the final n-state distribution.

To produce the chirped MW pulse we use a voltage-controlled oscillator, whose frequency varies from 13 to 19 GHz as the control voltage is changed from 2 to 15.5 V. We use its maximum sweep rate of 0.012 GHz. The typical output power is 10 mW. Using a control pulse from an arbitrary waveform generator and a pair of mixers in series we form the output into a swept pulse from 50 to 500 ns long. The pulse is amplified to powers as high as 300 mW with a solid-state amplifier and transported to the waveguide in the vacuum system.

As noted earlier, a Gaussian pulse should be nearly ideal, and using a 1 V, 50-ns-long Gaussian control pulse from the arbitrary waveform generator we have generated a swept pulse centered at 15.2 GHz. In Fig. 3 we show the population transfer observed when starting with $n = 72$ atoms and exposing them to this pulse. Figure 3 is composed of oscilloscope traces of the time-resolved field-ionization signals observed with no pulse (dashed line), and pulses with a peak amplitudes of 2 V/cm (dotted line) and 3 V/cm (solid line). For no pulse, and pulses of peak

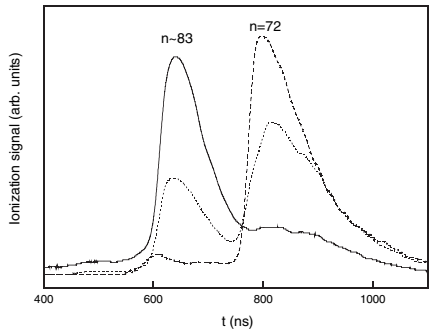

FIG. 3. Time-resolved field-ionization signals obtained subsequent to exposing $n = 72$ atoms to a 50 ns, +0.012 GHz/ns chirped pulse centered at 15.2 GHz, so that only ~600 MHz of chirp is required. For pulse amplitude zero (dashed line), the atoms stay in the $n = 72$ state. For pulse amplitude 2 V/cm (dotted line), roughly 40% of the atoms are transferred to $n \approx 83$. With pulse amplitude 3 V/cm (solid line), more than 80% of the atoms are transferred to $n \approx 83$.

amplitude <1 V/cm no population transfer is observed and the signal is observed at $t = 800$ ns. For a peak amplitude of 2 V/cm, almost half the signal is observed at $t = 640$ ns, corresponding to population transfer to $n \approx 83$. For a peak amplitude of 3 V/cm > 80% of the population is transferred to $n \approx 83$. At higher fields the population transfer decreases, as expected. We have changed n by ~11 using a MW pulse which is only chirped by 600 MHz in 50 ns. Using the Gaussian pulse used in the population transfer of Fig. 3 leads to about half as much transfer for initial $n = 71$ and 73 states and no transfer for initial $n = 70$ and 74 states.

One of the reasons for using a short frequency sweep is to minimize the number of avoided crossings encountered to ensure that only the desired avoided crossing is traversed adiabatically, but the sweep need not be short. With properly chosen pulses swept over 6 GHz the atom will find the desired avoided crossing itself. In Fig. 4 we show the population transfers observed with 500-ns-long constant amplitude pulses swept in both directions between 13 and 19 GHz. The data shown in each panel are gray-scale representations of time-resolved field-ionization signals for amplitudes of MW field E from 0.015 to 15 V/cm. In Fig. 4(a) we show the result of exposing $n = 80$ atoms to a $19 \rightarrow 13$ GHz chirp. As E increases from 0.1 to 3 V/cm the change in n increases from 0 to 10. How this population transfer occurs when $E \approx 3$ V/cm may be understood with the aid of Fig. 2(b). The atoms pass diabatically from point B to C, where ARP occurs, followed by a diabatic passage to point D. Figure 4(b) shows the analogous result for $n = 73$ atoms exposed to a pulse chirped from 13 to 19 GHz. In Figs. 4(a) and 4(b) the change in n increases with the MW-field amplitude and is approximately equal to the number of levels coupled together by the MW field, i.e., the number of smooth energy-level curves at the top of Fig. 2(b). It is as if the atoms follow diabatic trajectories which are reflected from the smooth curves of Fig. 2(b). This observation can be understood by considering the requirement for an adiabatic passage given by Eq. (2). In the chirped pulses used in obtaining the data of Figs. 4(a) and 4(b) the first and only avoided crossing to be traversed adiabatically is the one just below the smooth curves. By calculating the Floquet level structure, and thus Ω_k, for different microwave fields we can predict the Δn of the population transfer for a given field amplitude. The results of these calculations for the conditions of, for example, Fig. 4(a) are in good agreement with our observations, as shown. With a 6 GHz sweep we can select Δn, independent of n over a range of n, by the MW-field amplitude.

The multiphoton ARP approach described here allows rapid, efficient population transfer over many n states with easily generated pulses. One can envision using several such pulses, centered at different frequencies, to effect still larger changes in n on a 1 μs time scale, which could be quite useful for transporting recombined antihydrogen to

PRL 96, 073002 (2006) PHYSICAL REVIEW LETTERS week ending 24 FEBRUARY 2006

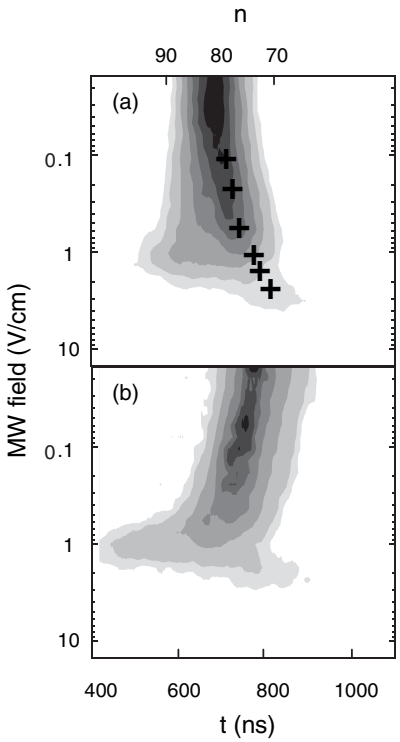

FIG. 4. Gray-scale renderings of the final-state distributions subsequent to exposure to constant amplitude MW pulses. Each panel is built up from 26 oscilloscope traces of the field-ionization signals; $t = 0$ corresponds to the beginning of the field ramp. (a) Atoms initially in $n = 80$ exposed to 19 to 13 GHz chirped pulses. The calculated Δn transfers are shown by crosses (+). Population transfer to n as low as ~ 72 is observed. (b) Atoms initially in $n = 73$ exposed to 13 to 19 GHz chirped pulses. Population transfer to $n \approx 77$ is efficient, and transfer to very high n states is observed.

lower lying states [16]. More generally, this work suggests that it may actually be simpler to use a single multiphoton resonance than a sequence of single-photon resonances since only a small chirp is required. Furthermore, this process is robust; it works in spite of the presence of many levels which we have ignored. Since it is straightforward to generate tailored laser pulses [17–19], especially ones with Gaussian intensity profiles and prescribed chirps, this approach should be applicable to other physical systems [2,9]. For example, laser excitation of a high vibrational state of a diatomic molecule using one multiphoton transition rather than a sequence of single-photon transitions is a case almost identical to this one.

It is a pleasure to acknowledge stimulating discussions with L. A. Bloomfield and R. R. Jones. This work has been supported by the National Science Foundation under Grants No. PHY-0244320 and No. CHE-0215957.

[1] S. Chelkowski, A. D. Bandrauk, and P. B. Corkum, Phys. Rev. Lett. **65**, 2355 (1990).
[2] D. J. Maas *et al.*, Chem. Phys. Lett. **290**, 75 (1998).
[3] D. M. Villeneuve *et al.*, Phys. Rev. Lett. **85**, 542 (2000).
[4] R. G. Hulet and D. Kleppner, Phys. Rev. Lett. **51**, 1430 (1983).
[5] B. Meerson and L. Friedland, Phys. Rev. A **41**, 5233 (1990).
[6] J. Lambert, M. W. Noel, and T. F. Gallagher, Phys. Rev. A **66**, 053413 (2002).
[7] H. Maeda, D. V. L. Norum, and T. F. Gallagher, Science **307**, 1757 (2005).
[8] J. Oreg, F. T. Hioe, and J. H. Eberly, Phys. Rev. A **29**, 690 (1984).
[9] G. N. Gibson, Phys. Rev. A **72**, 041404 (2005).
[10] N. V. Vitanov *et al.*, Annu. Rev. Phys. Chem. **52**, 763 (2001); N. V. Vitanov *et al.*, Adv. At. Mol. Opt. Phys. **46**, 55 (2001).
[11] B. Broers, H. B. van Linden van den Heuvell, and L. D. Noordam, Phys. Rev. Lett. **69**, 2062 (1992).
[12] J. H. Shirley, Phys. Rev. **138**, B979 (1965).
[13] R. V. Jensen, S. M. Susskind, and M. M. Sanders, Phys. Rep. **201**, 1 (1991).
[14] A. Buchleitner, D. Delande, and J. Zakrewski, Phys. Rep. **368**, 409 (2002).
[15] T. F. Gallagher, *Rydberg Atoms* (Cambridge University Press, Cambridge, 1994), p. 103.
[16] G. Gabrielse *et al.*, Phys. Rev. Lett. **89**, 213401 (2002).
[17] T. C. Weinacht, J. Ahn, and P. H. Bucksbaum, Phys. Rev. Lett. **80**, 5508 (1998).
[18] G. Vogt *et al.*, Phys. Rev. Lett. **94**, 068305 (2005).
[19] E. Wells *et al.*, Phys. Rev. A **72**, 063406 (2005).

Bibliography

[1] I. Martinson and L. Curtis, Nucl. Instrum. & Methods B **235**, 17 (2005).

[2] T. P. Hezel, C. E. Burkhardt, M. Ciocca, and J. J. Leventhal, Am. J. Phys. **60**, 324 (1991).

[3] P. Goy, J. Liang, M. Gross, and S. Haroche, Phys. Rev. A **34**, 2889 (1986).

[4] C. J. Lorenzen and K. Niemax, Phys. Scr. **27**, 300 (1983).

[5] T. F. Gallagher, *Rydberg Atoms* (Cambridge University Press, Cambridge, 1994).

[6] M. G. Littman, M. M. Kash, and D. Kleppner, Phys. Rev. Lett. **41**, 103 (1978).

[7] M. Fowler, The Photoelectric Effect, Lecture Notes, PHYS252, Univerisity of Virginia, 1997.

[8] L. F. DiMauro and P. Agostini, in *Advances in Atomic, Molecular, and Optical Physics*, edited by B. Bederson and H. Walther (Academic Press, San Diego, CA, 1995), Vol. 35, Chap. Ionization Dynamics in Strong Laser Fields, pp. 79–120.

[9] A. L'Huillier, L. A. Lompre, G. Mainfray, and C. Manus, J. Phys. B **16**, 1363 (1983).

[10] S. Augst *et al.*, Phys. Rev. Lett. **63**, 2212 (1989).

[11] M. D. Perry, A. Szoke, O. L. Landen, and E. M. Campbell, Phys. Rev. Lett. **60**, 1270 (1988).

[12] R. G. Tomlinson, Phys. Rev. Lett. **14**, 489 (1965).

[13] P. A. M. Dirac, Proc. R. Soc., London, Sec. A **114**, 243 (1927).

[14] Z. Deng and J. H. Eberly, J. Opt. Soc. Am. B **2**, 486 (1985).

[15] Z. Deng and J. H. Eberly, Phys. Rev. Lett. **53**, 1810 (1984).

[16] A. Giusti-Suzor and P. Zoller, Phys. Rev. A **36**, 5178 (1987).

[17] T. Clausen, Ph.D. thesis, Wesleyan University, 2002.

[18] J. E. Bayfield and P. M. Koch, Phys. Rev. Lett. **33**, 258 (1974).

[19] D. R. Mariani, W. Van de Water, P. M. Koch, and T. Bergeman, Phys. Rev. Lett. **50**, 1261 (1983).

[20] K. A. H. van Leeuwen *et al.*, Phys. Rev. Lett. **55**, 2231 (1985).

[21] R. V. Jensen, S. M. Susskind, and M. M. Sanders, Phys. Rept. **201**, 1 (1991).

[22] J. G. Leopold and D. Richards, Journal of Physics B: Atomic and Molecular Physics **19**, 1125 (1986).

[23] T. Clausen and R. Blümel, Phys. Rev. A **70**, 053411 (2004).

[24] P. Pillet *et al.*, Phys. Rev. Lett. **50**, 1042 (1983).

[25] P. Pillet *et al.*, Phys. Rev. A **30**, 280 (1984).

[26] P. Pillet, C. H. Mahon, and T. F. Gallagher, Phys. Rev. Lett. **60**, 21 (1988).

[27] R. C. Stoneman, D. S. Thomson, and T. F. Gallagher, Phys. Rev. A **37**, 1527 (1988).

[28] H. Maeda and T. F. Gallagher, Phys. Rev. Lett. **93**, 193002 (2004).

[29] A. Schelle, D. Delande, and A. Buchleitner, Phys. Rev. Lett. **102**, 183001 (2009).

[30] R. V. Jensen, S. M. Susskind, and M. M. Sanders, Phys. Rev. Lett. **62**, 1476 (1989).

[31] N. B. Delone, S. P. Goreslavsky, and V. P. Krainov, J. Phys. B **27**, 4403 (1994).

[32] G. Casati, B. V. Chirikov, D. L. Shepelyansky, and I. Guarneri, Phys. Rept. **154**, 77 (1987).

[33] G. Casati, I. Guarneri, and D. L. Shepelyansky, Phys. Rev. A **36**, 3501 (1987).

[34] P. W. Anderson, Phys. Rev. **109**, 1492 (1958).

[35] J. H. Shirley, Phys. Rev. **138**, B979 (1965).

[36] A. Krug and A. Buchleitner, Phys. Rev. A **66**, 053416 (2002).

[37] A. Buchleitner, D. Delande, and J.-C. Gay, J. Opt. Soc. Am. B **12**, 505 (1995).

[38] A. Buchleitner, B. Gremaud, and D. Delande, J. Phys. B **27**, 2663 (1994).

[39] Y. K. Ho, Physics Reports **99**, 1 (1983).

[40] N. F. Ramsey, *Molecular Beams* (Oxford University Press, Oxford, 1956).

[41] R. Lafon *et al.*, Phys. Rev. Lett. **86**, 2762 (2001).

[42] T. W. Hänsch, Appl. Opt. **11**, 895 (1972).

[43] M. G. Littman and H. J. Metcalf, Appl. Opt. **17**, 2224 (1978).

[44] I. Shoshan, N. N. Danon, and U. P. Oppenheim, J. Appl. Phys. **48**, 4495 (1977).

[45] D. Schumacher *et al.*, Appl. Opt. **41**, 1722 (2002).

[46] A. J. S. McGonigle *et al.*, Appl. Opt. **41**, 1714 (2002).

[47] B. Saleh and M. Teich, *Fundamentals of Photonics* (John Wiley and Sons, Inc., New York, 1991).

[48] E. Hecht, *Optics* (Addison Wesley, San Francisco, 2002).

[49] V. N. Rai, M. Shukla, and R. K. Khardekar, Meas. Sci. Technol. **5**, 447 (1994).

[50] M. G. Littman, Optics Letters **3**, 138 (1978).

[51] S. Ramo and J. R. Whinnery, *Fields and Waves in Modern Radio* (John Wiley & Sons, Inc., New York, 1953).

[52] R. Baierlein, *Thermal Physics* (Cambridge University Press, Cambridge, 1999).

[53] J. H. Moore, C. C. Davis, and M. A. Coplan, *Building Scientific Apparatus: A Practicle Guide to Design and Construction* (Addison Wesley, Reading, MA, 1983).

[54] Edwards Vacuum, Edwards B34831977 Diffstak 160/700M Overview and Technical Specs (2009).

[55] Duniway Stockroom Corp., Duniway: Glass Ion - Information (2009).

[56] A. Chatterjee, K. Mallik, and S. M. Oak, Rev. Sci. Instrum. **69**, 2166 (1998).

[57] K. Mallik, Rev. Sci. Instrum. **71**, 1853 (2000).

[58] N. Chadderton, The ZTX415 Avalanche Mode Transistor: An Introduction to Characteristics, Performance, and Applications (1996).

[59] J. L. Wiza, Nucl. Instrum. & Methods. **162**, 587 (1979).

[60] E. J. Galvez *et al.*, Phys. Rev. Lett. **61**, 2011 (1988).

[61] A. L'Huillier, L. A. Lompre, G. Mainfray, and C. Manus, Phys. Rev. A **27**, 2503 (1983).

[62] W. Zhao *et al.*, J. Opt. Soc. Am. B **38**, 191 (2005).

[63] J. J. Mestayer *et al.*, Phys. Rev. Lett. **100**, 243004 (2008).

[64] M. T. Frey *et al.*, Rev. Sci. Instrum. **64**, 3649 (1993).

[65] D. Delande and J. C. Gay, Europhysics Letters **5**, 303 (1988).

[66] E. S. Shuman, R. R. Jones, and T. F. Gallagher, Phys. Rev. Lett. **101**, 263001 (2008).

[67] V. E. Klimenko, Ph.D. thesis, University of Virginia, 2002.

[68] T. F. Gallagher, Phys. Rev. Lett. **61**, 2304 (1988).

[69] J. G. Story, D. I. Duncan, and T. F. Gallagher, Phys. Rev. Lett. **70**, 3012 (1993).

[70] E. S. Shuman, Ph.D. thesis, University of Virginia, 2007.

[71] H. Maeda and T. F. Gallagher, Phys. Rev. Lett. **92**, 133004 (2004).

[72] H. Maeda and T. F. Gallagher, Physical Review A (Atomic, Molecular, and Optical Physics) **75**, 033410 (2007).

[73] D. W. Schumacher, D. I. Duncan, R. R. Jones, and T. F. Gallagher, J. Phys. B **29**, L397 (1996).

[74] B. J. Lyons *et al.*, Phys. Rev. A **57**, 3712 (1998).

[75] U. Fano and J. W. Cooper, Rev. Mod. Phys. **40**, 441 (1968).

[76] K. T. Lu and U. Fano, Phys. Rev. A **2**, 81 (1970).

[77] M. J. Seaton, Proc. Phys. Soc., London **88**, 801 (1966).

[78] M. J. Seaton, Rep. Prog. Phys. **46**, 167 (1983).

[79] W. E. Cooke and C. L. Cromer, Phys. Rev. A **32**, 2725 (1985).

[80] U. Fano, Phys. Rev. A **2**, 353 (1970).

[81] X. Wang and W. E. Cooke, Phys. Rev. A **46**, 4347 (1992).

[82] X. Wang and W. E. Cooke, Phys. Rev. Lett. **67**, 976 (1991).

[83] S. N. Pisharody and R. R. Jones, Phys. Rev. A **65**, 033418 (2002).

[84] H. Maeda, J. H. Gurian, D. V. L. Norum, and T. F. Gallagher, Phys. Rev. Lett. **96**, 073002 (2006).

[85] H. Maeda, D. V. L. Norum, and T. F. Gallagher, Science **307**, 1757 (2005).

[86] J. Lambert, M. W. Noel, and T. F. Gallagher, Phys. Rev. A **66**, 53413 (2002).

[87] M. W. Noel, W. M. Griffith, and T. F. Gallagher, Phys. Rev. Lett. **83**, 1747 (1999).

[88] M. W. Noel, W. M. Griffith, and T. F. Gallagher, Phys. Rev. A **62**, 63401 (2000).

This work is typeset in URW Palladio using LaTeX 2_ε, an open-source document preparation system. URW Palladio is a free version of Hermann Zapf's Palatino, first designed in 1948.